

# Experimental tests of random wave models with chaotic microwave billiards



## Dissertation

Presented in Partial Fulfillment  
of the Requirements for the Degree of

**Doctor of Natural Sciences**  
(Dr. rer. nat.)

Submitted to the Faculty of Physics  
Philipps-University Marburg

by

**Ruven Höhmann**

Marburg/Lahn 2008

Vom Fachbereich Physik der Philipps-Universität Marburg/Lahn als Dissertation  
am 16. Juni 2008 angenommen.

Erstgutachter: Prof. Dr. H.-J. Stöckmann

Zweitgutachter: Prof. Dr. B. Eckhardt

Tag der mündlichen Prüfung: 26. Juni 2008

# Zusammenfassung

In dieser Arbeit werden durch Zufallswellenmodelle gewonnene Vorhersagen mit Hilfe von Mikrowellen-Experimenten überprüft. In wellenmechanischen bzw. quantenmechanischen Systemen, deren klassische Dynamik chaotisch ist, können mit dem Modell der zufälligen Überlagerung von Wellen statistische Aussagen über physikalische Größen getroffen werden, die nur von allgemeinen Eigenschaften der Wellenfunktion abhängen. Um quantenmechanische Systeme zu untersuchen, nutzen wir in unseren Experimenten aus, dass in quasi-zweidimensionalen Mikrowellenresonatoren eine Äquivalenz zwischen Schrödingergleichung und Helmholtzgleichung existiert.

Im ersten Teil dieser Arbeit werden räumliche Korrelationsfunktionen in einem offenen Billardsystem untersucht. In offenen quantenmechanischen Systemen erwartet man laufende Wellen als Lösung der Schrödingergleichung. Somit muss die Wellenfunktion als komplexe Größe beschrieben werden. Dadurch sind im zweidimensionalen die Nullstellen der Funktion Knotenpunkte und nicht, wie für geschlossene Billardsysteme, Knotenlinien. Es werden in dieser Arbeit räumliche Korrelationsfunktionen zwischen den Knotenpunkten der Wellenfunktion und den Sattelpunkten der Phase untersucht. Hierbei wird zudem der Einfluss der endlichen Systemgröße auf die räumlichen Korrelationsfunktionen betrachtet. Als letztes wird in diesem Teil die statistische Verteilung des Quantenstresstensors untersucht.

Im zweiten Teil wird die zeitliche Stabilität eines quantenmechanischen Systems gegenüber einer lokalen Störung betrachtet. Das Überlapp-Integral der zeitlichen Entwicklung eines gestörten und eines ungestörten Systems mit der selben Anfangswellenfunktion wird als *Fidelity* bezeichnet und gibt die zeitliche Stabilität eines quantenmechanischen Systems gegenüber einer Störung wieder. Experimentell wird für die Realisierung einer lokalen Störung ein kleiner Störkörper in einem Billiard verschoben. Mit Hilfe des Modells der zufälligen Überlagerung ebener Wellen wird ein theoretischer Ausdruck für die Fidelity einer lokalen Störung hergeleitet und mit den experimentellen Ergebnissen verglichen.

Im letzten Teil der Arbeit wird die Wahrscheinlichkeit für das Auftreten extrem hoher Wellen auf Meeren – sogenannter Monsterwellen – untersucht. Untersuchungen mit Radarsatelliten haben gezeigt, dass ein rein statistisches Modell zufällig überlagerter Wellen diese Häufigkeit unterschätzt. Ein Ansatzpunkt zur Erklärung der deutlich höheren Wahrscheinlichkeit für Monsterwellen sind Fokussierungseffekte, hervorgerufen durch ortsabhängige Geschwindigkeitsfelder. Diese können wiederum durch Wirbel oder im Flachwasser durch unterschiedliche Wassertiefen entstehen. In dieser Arbeit wird eine Analogstudie mit Mikrowellen vorgestellt, die zeigt, dass sich eine erhöhte Wahrscheinlichkeit für extrem hohe Wellen ergibt.



# Abstract

In this work we shall test predictions of random wave models with microwave experiments. In wave or quantum mechanical systems, where the classical dynamic is chaotic, we can make predictions on quantities which only depend on general properties of the wave function. In our experiments on quasi two-dimensional microwave cavities we use the complete equivalence of the Schrödinger equation and the Helmholtz equation to study properties of quantum systems with electromagnetic waves.

In the first part of this thesis we investigate spatial correlation functions of open billiard systems. In open quantum systems we expect running waves as the solution of the Schrödinger equation. Thus the wave function is complex and the zeros of a two-dimensional complex function are nodal points and not nodal lines as we would expect for a closed system. In this work we shall investigate the spatial correlation function between nodal points of the wave function and saddle points of the phase of the wave function. For this correlation function we will additionally look for the influence of the boundary due to the finite size of the system. Another quantity one can study is the distribution of the components of the quantum stress tensor.

In the second part we shall study the time dependent stability of a quantum system against a local perturbation. The time dependent stability of a quantum system is described by the *fidelity*, which is defined as the overlap integral of the time evolution of the same initial state under an unperturbed and a perturbed Hamiltonian. Experimentally the local perturbation has been realized by the shift of a small scatterer. We use the model of random plane waves to calculate a theoretical expression for the fidelity of a local perturbation and compare this to our experimental results.

In the last part of this work we shall present an analogue experiment with microwaves to investigate the probability of extreme wave heights in the ocean. Such high amplitudes in the ocean are called freak waves, rogue waves or sometimes giant waves. Data of wave heights collected with radar satellite suggests that a random wave model surely underestimates the probability of such events. One way to explain the higher probability for freak waves is the effect of focussing of waves due to variable velocity fields. These velocity fields can be formed by current eddies or a height variation in shallow water. In our analogue study we use a potential landscape for microwaves to show the influence of focussing effects on the distribution of intensities.



# Contents

<b>1. Introduction</b>	<b>1</b>
<b>2. Basic principles</b>	<b>3</b>
2.1. Resonant cavities . . . . .	3
2.2. Measuring technique . . . . .	5
2.3. Random plane wave model . . . . .	8
<b>3. Spatial correlation functions in microwave billiards</b>	<b>11</b>
3.1. Introduction . . . . .	11
3.2. Experimental setup . . . . .	12
3.3. Vortex and saddle point correlations . . . . .	13
3.4. Boundary effects . . . . .	21
3.5. Stresstensor . . . . .	23
<b>4. Fidelity of local perturbations</b>	<b>33</b>
4.1. Introduction . . . . .	33
4.2. Experimental setup . . . . .	35
4.3. Theoretical model . . . . .	36
4.4. Results . . . . .	37
<b>5. Rogue waves</b>	<b>41</b>
5.1. General Introduction . . . . .	41
5.2. Basic properties of the experiment . . . . .	42
5.3. Scatterer Configurations . . . . .	51
5.4. Results in energy domain . . . . .	52
5.5. Transient waves . . . . .	57
<b>6. Summary and outlook</b>	<b>67</b>
<b>A. Bilinear interpolation and nodal line estimation</b>	<b>69</b>
A.1. The method of bilinear interpolation . . . . .	69
A.2. Limits of the bilinear interpolation . . . . .	71
A.3. Nodal lines of an interpolated field . . . . .	72
<b>B. Critical point analysis</b>	<b>75</b>
<b>C. Theoretical expressions for the pair correlation functions</b>	<b>79</b>
C.1. Pair correlation functions . . . . .	79
C.2. Densities of critical points from a straight boundary . . . . .	80

<b>D. Calculation of the period shift in correlation functions</b>	<b>83</b>
<b>E. Calculation of the variance of the level velocity distribution</b>	<b>85</b>
E.1. Calculation using the distribution function . . . . .	86
E.2. Calculation of higher order moments of Gaussian random variables . . . . .	87
<b>F. List of Figures</b>	<b>88</b>
<b>G. Bibliography</b>	<b>90</b>

# 1. Introduction

In classical mechanics we distinguish between regular and irregular motion of a particle. These two types of motion can be distinguished by the sensitivity of the trajectory against a slight change of the initial conditions. In case of a regular motion two trajectories which start with slightly different initial conditions will separate in phase space at most linearly in time whereas for irregular or chaotic motion the growth of the distance is exponential.

In the case of the quantum mechanics it is not obvious from the first sight what chaos means as here the concept of phase space trajectory does not hold any more. In the limit of  $\hbar \rightarrow 0$  or in other words for high quantum numbers we expect the classical mechanics to appear again from the quantum mechanics. It has been shown [Gut90, Haa01], that in the semiclassical regime the classical chaotic motion can be recognized again.

In 1984 Bohigas, Giannoni and Schmit did conjecture [Boh84] that statistical properties of quantum systems with chaotic classical dynamics can be described by random matrix theory. Random matrix theory has been developed by Wigner, Dyson and Mehta in the 1950s and 60s to describe the statistical properties of the spectra of complex nuclei [Por65]. There have been many numerical and experimental tests of the BGS-conjecture. One possible way to test this conjecture experimentally are billiard systems. Here the type of classical motion is determined by the billiard geometry. With flat quasi two-dimensional microwave resonators one has the possibility to study questions of quantum chaos. This is possible since the Schrödinger equation for a particle in a two-dimensional confined region with hard wall boundary conditions is equivalent to the Helmholtz equation, describing waves in flat quasi two-dimensional microwave resonators. This analogy has been used by many groups to study questions related to quantum chaos [Stöck90, Dor90, Sri91, Gräf92].

If one is interested in wave function properties of chaotic systems especially of chaotic billiard systems another very important model has to be considered. Many statistical properties of wave functions in chaotic billiards can be described with the famous random wave model (RWM) proposed by Berry [Ber77]. The model assumes that the wave function at any point in the interior of a billiard can be described by a random superposition of plane waves of different amplitudes and directions. This model has passed a large number of tests either experimentally or numerically in most cases with a remarkably good agreement. But there have been also some studies which showed the natural limit of this model. This happens whenever system specific features play an important role. Throughout this work we compare experimental results obtained from microwave measurements in chaotic billiards with predictions of the RWM.

In chapter three we start with the presentation of experimental results on spatial correlation function measured at a quantum-dot like resonator. Here we have tested correlation functions of vortices and saddle points for an open quantum system. In the low frequency regime of this study the wavelength becomes comparable with the system size giving rise to deviations from the random plane wave model. We extend the theoretical description of a class of correlation function to the situation if the system size is comparable to the wavelength. Finally we present experimental results on the quantum stress.

In the fourth chapter we investigate the influence of a local perturbation on the stability of a quantum system. This effect has been studied already in terms of the level velocity distribution [Bar99]. We extend this investigations to the framework of the fidelity – a quantity introduced by Peres to study the stability of quantum evolution [Per84]. We derive a theoretical expression for the fidelity using the RWM and compare it with our experimental results.

In the last part of this thesis we present results on an analogue experiment for rogue waves on the ocean. Rogue or giant waves have attracted more and more interest in the last decades as one has recognized that their occurrence is much more likely than predicted by a purely statistical random wave model [Kha03, Hel08, Law01]. The questions arises which physical mechanism is responsible for the deviations in the probability of finding extreme waves on the ocean. A possible explanation for the higher probability of freak waves is the effect of focussing of waves due to variable velocity fields. These velocity fields can be formed by current eddies or a height variation in shallow water. In our analogue study we use a potential landscape for microwaves to investigate the influence of focussing effects on the distribution of intensities.

## 2. Basic principles

### 2.1. Resonant cavities

The experiments in our group are based on measurements of electromagnetic waves in resonant cavities. The starting point for the theoretical description of our experimental situation is a hollow metallic cylinder with an arbitrary shape of the cross section. For simplicity we assume that the cross section is not changing along the cylinder axis and that conductance of the boundary of the cylinder is perfect. The  $z$ -axis is assumed to be along the cylinder axis.

From Maxwell's equations we can derive the stationary wave equation:

$$(\nabla^2 + k^2) \begin{Bmatrix} \vec{E} \\ \vec{B} \end{Bmatrix} = 0, \quad (2.1)$$

where  $k = 2\pi\nu/c$  is the modulus of the wave number ( $c$  : speed of light, and  $\nu$  : frequency). For the above described situation an ansatz where we single out the  $z$ -dependence of the two fields is suitable. The fields then read

$$\begin{Bmatrix} \vec{E}(x, y, z, t) \\ \vec{B}(x, y, z, t) \end{Bmatrix} = \begin{Bmatrix} \vec{E}(x, y)e^{\pm ik_z z - i2\pi\nu t} \\ \vec{B}(x, y)e^{\pm ik_z z - i2\pi\nu t} \end{Bmatrix} \quad (2.2)$$

Inserting this in the wave equation 2.1 we obtain a reduced wave equation:

$$(\nabla_{xy}^2 + k^2 - k_z^2) \begin{Bmatrix} \vec{E} \\ \vec{B} \end{Bmatrix} = 0. \quad (2.3)$$

For the following discussion it is useful to divide the components of the field vectors into a part parallel to the  $z$ -axis and one perpendicular ( $\vec{E} = \vec{E}_z + \vec{E}_t$  and  $\vec{B} = \vec{B}_z + \vec{B}_t$ ). It is possible to show [Jac82] that the transversal components are fully determined by the  $z$ -component of the electrical and the magnetic fields. Thus it is sufficient to study only the  $z$ -component of the reduced wave equation 2.3. The general boundary conditions

$$\vec{n} \times \vec{E} = 0 \quad \vec{n} \cdot \vec{B} = 0 \quad (2.4)$$

then reduce to

$$E_z|_S = 0 \quad \left. \frac{\partial B_z}{\partial n} \right|_S = 0. \quad (2.5)$$

In our experiment we close our cavity with an additional metallic boundary at  $z = 0$  and  $z = d$ . We can assume that the two boundaries are parallel to each other. There are two different solutions which satisfy the boundary conditions (2.5) and the stationary wave equation. In total we have for transverse magnetic (TM)-modes:

$$\left[ \nabla_{xy}^2 + k^2 - \left( \frac{n\pi}{d} \right)^2 \right] E_z = 0 \quad E_z|_S = 0 \quad (2.6)$$

with

$$E_z = \varphi(x, y) \cos \left( \frac{n\pi z}{d} \right) \quad n = 0, 1, 2, \dots, \quad (2.7)$$

where  $\varphi(x, y)$  is a scalar wave function and  $n$  is the *quantum* number in  $z$ -direction introduced by top and bottom plate. Each of this quantum numbers give rise to an independent mode in  $z$ -direction which we denote with  $\text{TM}_n$  corresponding to their  $z$ -quantum number. The second possible kind of solutions for the wave equation are the transverse electric (TE)-modes:

$$\left[ \nabla_{xy}^2 + k^2 - \left( \frac{m\pi}{d} \right)^2 \right] B_z = 0 \quad \left. \frac{\partial B_z}{\partial n} \right|_S = 0 \quad (2.8)$$

with

$$B_z = \phi(x, y) \sin \left( \frac{m\pi z}{d} \right) \quad m = 1, 2, 3 \dots \quad (2.9)$$

Here  $\phi(x, y)$  is as in the previous case a scalar wave function and  $m$  the quantum number in  $z$ -direction.

With our setup we couple microwaves with a small wire antenna from the top or bottom plate into a resonator. Thus the antenna is parallel to the  $z$ -axis and we can only couple electrical energy to TM-modes. So we focus in the following discussion only on the case of TM-modes.

### 2.1.1. Correspondence to quantum mechanics

In most of our experiments the resonator has a height  $d$  of 8 mm yielding a cutoff frequency for the first mode of  $\nu_{\text{cutoff}} = c/2d = 18.75$  GHz. Below this frequency only the TM modes with  $n = 0$  can propagate in the cavity. Thereby we see a strong similarity between equation 2.7 with  $n = 0$  and the two-dimensional Schrödinger equation with hard wall boundary conditions:

$$\left( \frac{\hbar^2}{2m} \nabla_{xy}^2 + E \right) \psi(x, y) = 0 \quad \psi(x, y)|_S = 0 \quad (2.10)$$

Formally these two equations are equivalent if we identify the  $z$ -component of the electrical field  $E_z$  with the quantum mechanical wave function  $\psi$  and the wave number  $k^2$  with quantum mechanical energy  $E$ . In addition we have to set  $\frac{\hbar^2}{2m} = 1$  for a full correspondence.

We can even extend this correspondence to model soft potentials with electromagnetical waves [Lau94, Kim05a]. For  $n \neq 0$  we have in equation 2.6 another term which can

be interpreted as a potential if we vary the distance  $d$  between top and bottom plate smoothly in dependence of the position. We then obtain the following correspondence:

$$V(x, y) = \left( \frac{n\pi}{d(x, y)} \right)^2 \quad (2.11)$$

This is obviously only true in the adiabatic limit, where the height variation is slow in comparison to the wave length, since for  $d$  varying with position the separation of the  $z$  component is only correct approximately. This analogy is used in chapter 5 to study waves in potential landscapes.

The second extension of our quantum billiard analogy by means of electromagnetic waves concerns the probability density current in quantum mechanics. If we open a system then the waves become complex or in other words we have traveling waves instead of standing waves in a closed system. Associated with traveling waves is a current. In quantum mechanics this probability current density can be calculated according to:

$$\vec{j} = \frac{\hbar}{m} \text{Im}(\psi^* \nabla \psi) \quad (2.12)$$

where  $\rho = |\psi|^2$  and  $\phi$  the phase of the wave function ( $\psi = \rho e^{i\phi}$ ). In the case of a slowly varying  $\rho$  this can be approximated to

$$\vec{j} \approx \frac{\hbar}{m} \rho \nabla \phi \quad (2.13)$$

where we see that in this limit the probability flow is described by the phase derivative. For the Poynting vector in a quasi two-dimensional resonator one can calculate the following relation [Šeb99]:

$$\vec{S} = \frac{c}{8\pi k} \text{Im}(E_z^* \nabla E_z) \quad (2.14)$$

As we can measure the complex signal of the electrical field (see section 2.2) we can directly reconstruct the Poynting vector and have an equivalence of the probability current density with the Poynting vector. In the following we call the probability current density and also the Poynting vector just flow or current. All further consequences of the flow in an open microwave billiard are discussed in the introduction of chapter 3

We have seen that with electromagnetic waves in cavities or resonators we have a rich analogy to study quantum mechanical properties of a single particle either in a closed system in an open system or even in a potential landscape. All these fields will be explored later on in this thesis

## 2.2. Measuring technique

We have started our description from a theoretical point of view. In this section we complete the frame work to describe our experiment. In the last section we have only treated the pure field inside a resonator. We did not consider how to couple waves into

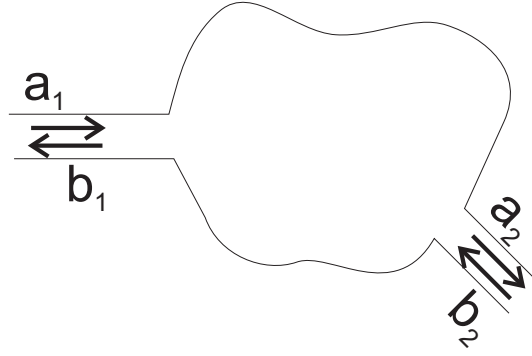


Figure 2.1.: Sketch to describe the scattering of microwaves at a cavity.

the cavity and out of the cavity to retrieve the information about the wave function which might have established inside a resonator. If we insert an antenna to measure the wave function inside of a microwave cavity we unavoidably disturb the wave function of the clean system. A suitable theoretical description of this situation in our experiment is scattering theory [Ste95].

Scattering theory had been originally developed to describe scattering experiments in nuclear physics. We can use and adopt this approach also to our microwave experiment. In figure 2.1 we present a sketch of the principal situation in our experiment, where we have for example attached two leads to a billiard. We are thus interested how the amplitudes  $a_i$  of the incoming waves are related to the amplitudes  $b_i$  of the outgoing waves. Formally these amplitudes can be connected via the elements of the scattering matrix  $S_{ij}$ :

$$\begin{pmatrix} b_1 \\ b_2 \end{pmatrix} = \begin{pmatrix} S_{11} & S_{12} \\ S_{21} & S_{22} \end{pmatrix} \begin{pmatrix} a_1 \\ a_2 \end{pmatrix} \quad (2.15)$$

In [Ste95] a relation between the scattering matrix  $S$  and the electromagnetic Greens-function  $G$  was calculated. In case of isolated resonances one has the billiard Breit-Wigner formula for the scattering matrix elements:

$$S_{ij} = \delta_{ij} + 2(\alpha + i\beta)G(\vec{r}_i, \vec{r}_j; k) \quad (2.16)$$

with coupling constants  $\alpha$ ,  $\beta$  and the Greensfunction

$$G(\vec{r}_i, \vec{r}_j; k) = \sum_{n=1}^{\infty} \frac{\Psi_n(\vec{r}_i)\Psi_n(\vec{r}_j)}{k_n^2 - k^2 + \Delta_n - \frac{i}{2}\Gamma_n} \quad (2.17)$$

Here is

$\Psi_n(\vec{r}_i)$  the  $n$ th eigenfunction of the unperturbed system at the position  $\vec{r}_i$  of the antenna.

$\Gamma_n$  the spectral line widths of the resonances, with  $\Gamma_n = \alpha \sum_i |\Psi_n(\vec{r}_i)|^2$

$\Delta_n$  the shift of the resonance due to the antenna, with  $\Delta_n = \beta \sum_i |\Psi_n(\vec{r}_i)|^2$ .

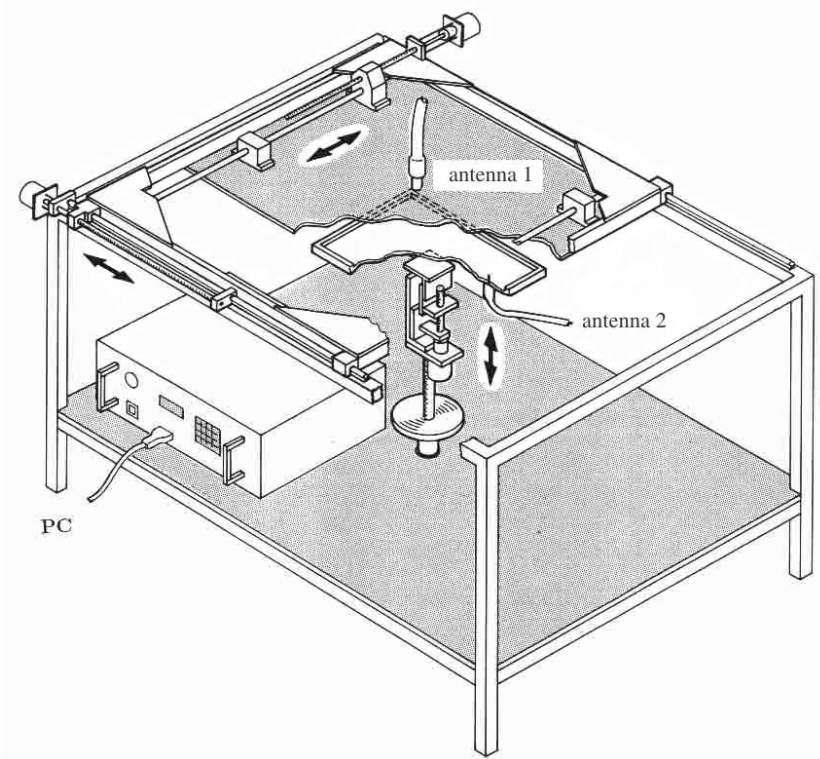


Figure 2.2.: Setup of the wave function measurement table used in our group.

In the resonance case where  $k^2 = k_n^2 + \Delta_n^2$  equation 2.16 can be reduced to:

$$S_{ij} = \delta_{ij} - 2(\beta - i\alpha) \frac{\psi_n(\vec{r}_i)\psi_n(\vec{r}_j)}{\Gamma_n} \quad (2.18)$$

For later purposes we present here the result for the intensity of the wave function in the resonance case at the position  $\vec{r}_i$  of the antenna. The intensity for a reflection spectra  $S_{ii}$  with  $i = 1, 2$  then reads:

$$|\psi_n(\vec{r}_i)|^2 = \frac{(1 - \text{Re}(S_{ii}(\vec{r}_i)))\Gamma_n}{4\beta} = \frac{\text{Im}(S_{ii}(\vec{r}_i))\Gamma_n}{4\alpha} \quad (2.19)$$

With a Lorentzian fit of the reflection spectra  $S_{ii}$  it is possible to extract the resonance position  $k_n^2 + \Delta_n^2$  and the width  $\Gamma_n$  of the resonance (for the transmission a similar derivations holds). The coupling constants  $\alpha$  or  $\beta$  can be extracted by a proper normalization of the wave function. We need this procedure in chapter 4 to extract the ordinary fidelity from the wave function properties.

The measurements of the microwave spectra have been performed with the vector network analyzers (VNA) Agilent8720ES and Wiltron360B. A VNA measures the entire scattering matrix  $S$  of a system with modulus and phase as function of frequency. With the Agilent8720ES we measure the scattering matrix in the frequency regime from 0.5 GHz up to 20 GHz with a resolution of 0.5 MHz. This is our standard measurement device. For a measurement above 20 GHz we use the Wiltron360B. A detailed description is found in [Ste93, Bar01].

For two dimensional measurements we use a wave function measurement table which is shown in figure 2.2. It consists of a top plate which can be moved in  $(x, y)$ -direction. Attached to this top plate is an antenna which can scan the underlying billiard. The device was constructed by Ulrich Kuhl who also has developed the software to control it [Kuh98]. Thereby we have the possibility to measure the spatial resolved transmission or reflection coefficients of the scattering matrix  $S$  for a frequency in the range mentioned above. For the sake of simplicity we call in chapter 3 and 5 the result of such a measurement at a single frequency a *wave function*.

### 2.3. Random plane wave model

We have discussed briefly in the introduction that in a chaotic cavity we can describe the wave function by superposition of (infinitely many) random plane waves with random amplitudes  $a_i$  and random directions of the wave vectors  $\vec{k}_i$  where the modulus for all contributing wave vector is fixed ( $|\vec{k}_i| = k$ ).

$$\psi(\vec{r}) = \sum_i a_i e^{i\vec{k}_i \vec{r}} \quad (2.20)$$

From this equation one can derive for instance the amplitude distribution function of a wave function in a closed chaotic cavity. Here we repeat the well known calculation to demonstrate the basic ideas.

We start with the ansatz to calculate the distribution with an average over a  $\delta$ -function

$$P(\psi) = \left\langle \delta \left( \psi - \sum_i a_i e^{i\vec{k}_i \vec{r}} \right) \right\rangle. \quad (2.21)$$

Expressing the  $\delta$ -function by its Fourier representation we obtain:

$$P(\psi) = \frac{1}{2\pi} \int_{-\infty}^{\infty} dt e^{it\psi} \prod_{i=0}^N \langle e^{ita_i e^{i\vec{k}_i \vec{r}}} \rangle. \quad (2.22)$$

From here we see that we can perform the average for each component individually. If we then express the exponential function by a series we have

$$\langle e^{ita_i e^{i\vec{k}_i \vec{r}}} \rangle = 1 - it \langle a_i e^{i\vec{k}_i \vec{r}} \rangle - \frac{t^2}{2} \langle a_i^2 e^{2i\vec{k}_i \vec{r}} \rangle + \dots \quad (2.23)$$

$$= 1 - \frac{t^2}{2} \langle a_i^2 \rangle + \dots \quad (2.24)$$

To proceed our calculation from equation 2.22 we have to calculate the variance of  $a_i$  which we can do by using the normalization condition of the wave function:

$$1 = \int |\psi|^2 dA = \sum_{i,j} a_i a_j \int e^{i\vec{k}_i \vec{r}} e^{i\vec{k}_j \vec{r}} dA = A \sum_i a_i^2 = AN \langle a_i^2 \rangle \quad (2.25)$$

In the limit  $N \rightarrow \infty$  we only have contributions if  $\vec{k}_i = -\vec{k}_j$ . Inserting these results all together in 2.22 we end up in the limit  $N \rightarrow \infty$

$$P(\psi) = \frac{1}{2\pi} \int_{-\infty}^{\infty} dt e^{it\psi} \left(1 - \frac{t^2}{2AN} + \dots\right)^N \quad (2.26)$$

$$P(\psi) = \frac{1}{2\pi} \int_{-\infty}^{\infty} dt e^{it\psi} e^{-\frac{t^2}{2A}} \quad (2.27)$$

$$P(\psi) = \sqrt{\frac{A}{2\pi}} e^{-\frac{A\psi^2}{2}} \quad (2.28)$$

In the last step the Fourier transform of a Gaussian was used. Thus we have calculated the amplitude distribution function for a wave function in a chaotic cavity. The results can be interpreted as a consequence of the central limit theorem yielding a Gaussian distribution.

This result and the spatial autocorrelation function of the wave function are the main ingredients for the derivation of an analytic expression for the fidelity of a local perturbation in chapter 4. The spatial autocorrelation function can also be calculated using the RWM yielding:

$$\langle \psi(\vec{r} + \vec{r}') \psi(\vec{r}') \rangle = \frac{1}{A} J_0(kr) \quad (2.29)$$

where  $k = |\vec{k}|$  is the wave number and  $A$  the billiard area. The above calculation and discussion can also be found in a similar way in [Stöck99, Bar01].



# 3. Spatial correlation functions in microwave billiards

## 3.1. Introduction

In the general introduction we have seen that in chaotic quantum systems one can find a large number of generic features which does not depend on the specific system under consideration. Here we will focus on quantities which depend on the statistical properties of the wave function. In chapter 2 we have already discussed that for wave systems where the classical or ray dynamic is chaotic, it has been conjectured by Berry [Ber77] that the wave function can be described by a superposition of random plane waves. With this conjecture one is able to calculate the spatial amplitude fluctuations for the eigenfunction in a chaotic wave billiard (see eq. 2.28) which results in a Gaussian distribution of the amplitudes.

The application of random Gaussian fields to describe the spatial structure of complex physical systems has a long successful history. It has started with the description of the random currents of shot noise by Rice [Ric45] going over to Longuet-Higgins' description of water waves [Lon57a, Lon57b]. More recently this model has been applied in diverse fields as for example for acoustics [Ebe84, Tan07], turbulence [Fri95], optical speckle pattern [Doy02, Goo07] and the cosmic microwave background fluctuations [Lid00].

More specifically in the realm of wave chaos studied by microwave measurements this model has been successfully applied to predict spatial correlation functions of the wave functions [Eck99] and quantities which can be directly related to its amplitude fluctuations. Among them are the distributions of currents [Šeb99, Bar01, Bar02, Kim03a], the intensity distributions in the transition from closed to open billiards with the measurement of long range correlations between the intensity and the density current [Kim05b] and the pair correlation function of vortex points in an open billiard [Kim03a, Bar01].

A tool to study open quantum billiards are the so called quantum dots. The first studies on quantum dots have been performed with semiconductor microstructures where the mean free path of the electrons exceeds the size of the device [Mar92]. The main subject of investigations at quantum dots had been transport studies of ballistic electrons. The drawback with such devices on micrometer scale is that it was difficult at that time to study the interplay between transport properties and the wave functions of quantum dots. In our group we have fabricated a microwave analogue billiard to study exactly this interplay [Kim02, Kim03b]. Meanwhile this billiard has been used to investigate many properties of open quantum systems. For a recent review see [Kuh07].

As discussed in the last paragraphs in [Kim03a, Bar01] the pair correlation function and the nearest neighbor distribution of vortices has been investigated, too. Here these investigations of the pair correlation function shall be extended to the charged correlation function for vortex points. Furthermore we want to investigate the pair correlation functions between saddle points and vortex points and the pair correlation function between saddle points only. For completeness we will show also the nearest neighbor distance distributions for all the mentioned pair correlations.

Secondly we want to investigate in more detail finite size effects which we have seen during the analysis of the pair correlation function of vortex points. We will give a quantitative expression to describe the deviations of spatial correlation function which are due to confinement of the wave function in a finite domain.

Thirdly we investigate the statistical properties of the quantum stress in a chaotic billiard. Quantum stress is a quantity which was originally introduced by Pauli and which involves second order derivatives of the wave function [Pau33]. Thereby it supplements previous tests of the random plane wave model as it probes finer details of a wave function due to the second order derivatives.

## 3.2. Experimental setup

For all studies to be presented in this chapter we have used the same setup. The basic principles of the experiment have been already discussed in the introduction of this thesis. In figure 3.1 a sketch of the setup is shown. The billiard we used is a rectangular cavity (21 cm  $\times$  16 cm) with rounded corners. At the bottom the billiard was coupled to two wave guides of width 3 cm with a cut-off frequency at  $\nu_T = 5$  GHz. To break of symmetry and to block direct transport, two triangular obstacles with a length of 12 cm and a height of 1 cm were placed in the resonator. Absorbers were placed at the end of the leads to avoid reflections and to mimic infinitely long coupling channels. We scanned the billiard on a square grid of 2.5 mm with a movable antenna  $A_1$  and measured transmission  $S_{12}$  in the range of 4- 18 GHz from a fixed antenna  $A_2$  in the end of the right lead. The fixed antenna had a metallic core of diameter 1 mm and a teflon coating while the probe antenna  $A_1$  was a thin wire of diameter 0.2 mm to minimize the leakage current. The lengths of the antenna  $A_1$  and antenna  $A_2$  were 4 and 5 mm respectively.

We have seen in chapter 2 that for microwave frequencies  $\nu < c/2d = 18.75$  GHz, where  $c$  is the velocity of light and  $d$  is the resonator height, the billiard is quasi-two-dimensional. In this regime there is an exact correspondence between electrodynamics and quantum mechanics, where the component of the electric field perpendicular to the plane of the microwave billiard  $E_z$  corresponds to the quantum-mechanical wave function  $\psi$ . We normalize the wave function  $\psi$  such that  $\int d\mathbf{r}|\psi(\mathbf{r})|^2 = 1$ .

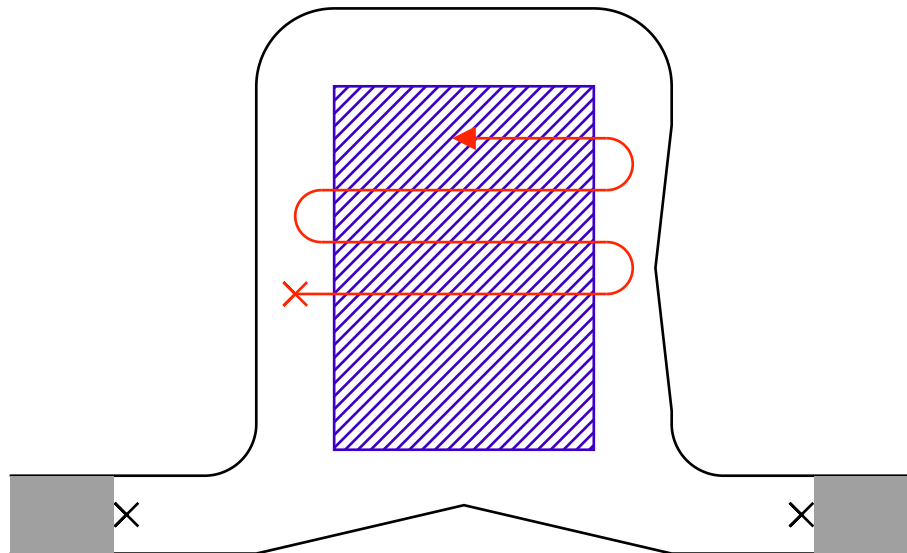


Figure 3.1.: Sketch of the microwave billiard. The basic size of the billiard is  $16\text{ cm} \times 21\text{ cm}$ . The attached leads have a width of  $3\text{ cm}$ . The central shaded field ( $10\text{ cm} \times 14\text{ cm}$ ) indicates the region of interest. The measurement grid size was  $2.5\text{ mm}$ . The gray regions at the end of the two leads indicate absorbers to mimic infinitely long channels. The crosses indicate the antennas in the system and the winding path illustrates how the third probing antenna is moved across the billiard during measurements.

## 3.3. Vortex and saddle point correlations

### 3.3.1. Introduction

Due to the two attached leads the billiard is an opened system. This has the effect that the measured wave function becomes complex which means that we have now traveling waves instead of standing waves. With traveling waves an energy transport, which can be described by the Poynting vector, is associated and which we have introduced in chapter 2. In figure 3.2 we show one example of the measured complex field inside the open cavity. In (a) and (b) the real and imaginary part of the wave function is shown. In (c) and (d) the modulus and the phase of the wave function is presented. In a closed system one expects nodal lines for the wave function. Whereas in open system due to the complex nature of the wave function its modulus has only nodal points. These nodal points are the crossings of the nodal lines of the real and the imaginary part of the wave function which are indicated in figure 3.2c by the blue and the red lines. The phase at a nodal point is ambiguous and has therefore a singularity in this point. By an integration around such a phase singularity we obtain a value which is a multiple of  $2\pi$ . In our case the acquired phase is always  $2\pi$ . As the flow is in good approximation described by the phase derivative (see equation 2.13) one can directly see the consequence of a nodal point for the flow. Each nodal point corresponds to a vortex point in the flow. There

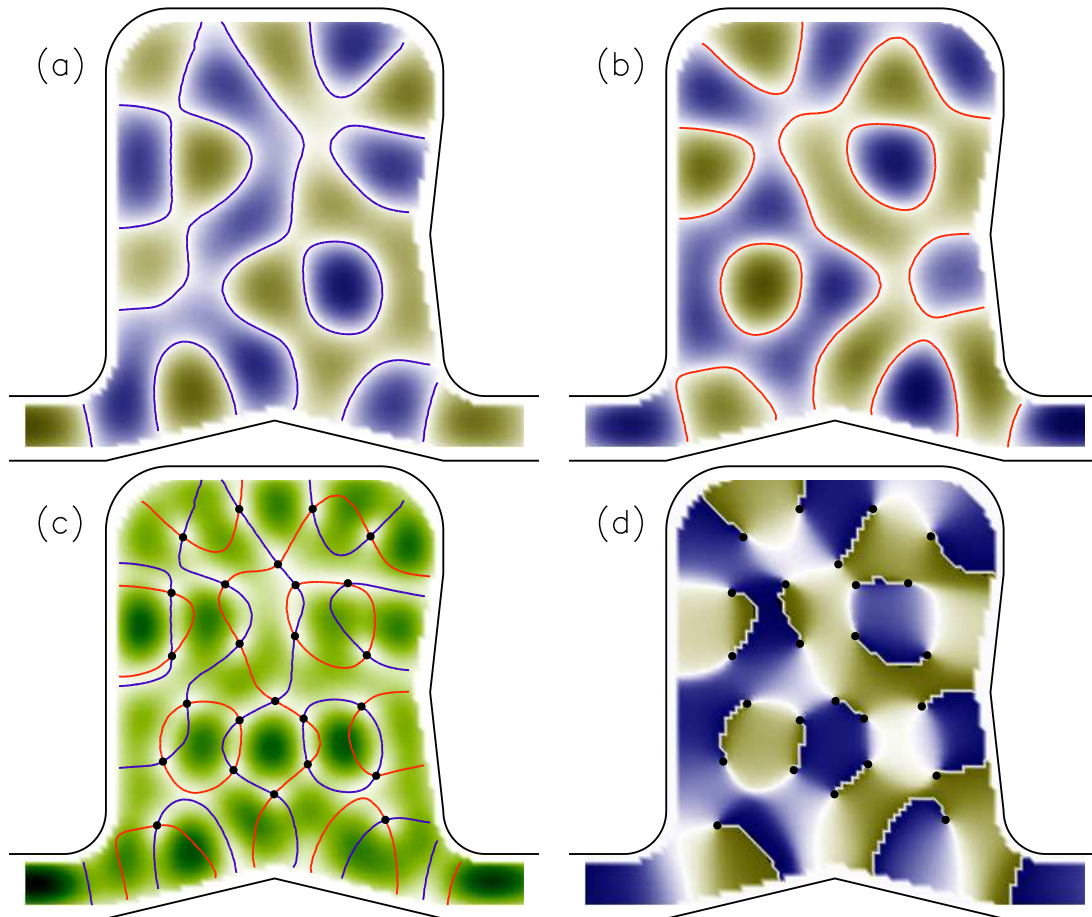


Figure 3.2.: Typical wave function in an open cavity measured at a frequency of  $\nu = 5.64$  GHz. In (a) the real part and in (b) the imaginary part of the wave function is shown. In (c) the modulus and in (d) the phase is presented. In (a) and (b) blue corresponds to positive values and beige to negative. In (d) the darkest blue color represents  $\pi$  and the darkest beige  $-\pi$ . A white color represents in all cases a value of zero. Additionally the nodal lines and points are shown in the figures.

exists a second set of topologically important points in the flow. They are called saddle points and are saddles of the phase of the wave function and correspond to hyperbolic points in the flow. If we speak of critical points either a vortex or a saddle points is meant.

As a second example we present another wave function in figure 3.3.1. In this figure we show the intensity of the wave function in part (a) and the flow for the full wave function in part (b). Additionally we present a blowup of the flow pattern where we demonstrate the different types of critical points. Vortices are indicated by filled circles. The color code is such that if the flow curls clockwise around a vortex point it is green, in case of a counterclockwise rotation it is red. There is a possibility to assign charges to vortex points. In this case vortices with a flow curling counterclockwise are assigned to positive charges, those with clockwise rotating flow to negative charges. Hyperbolic points of the flow are marked by crosses. The light blue lines indicate the measurement

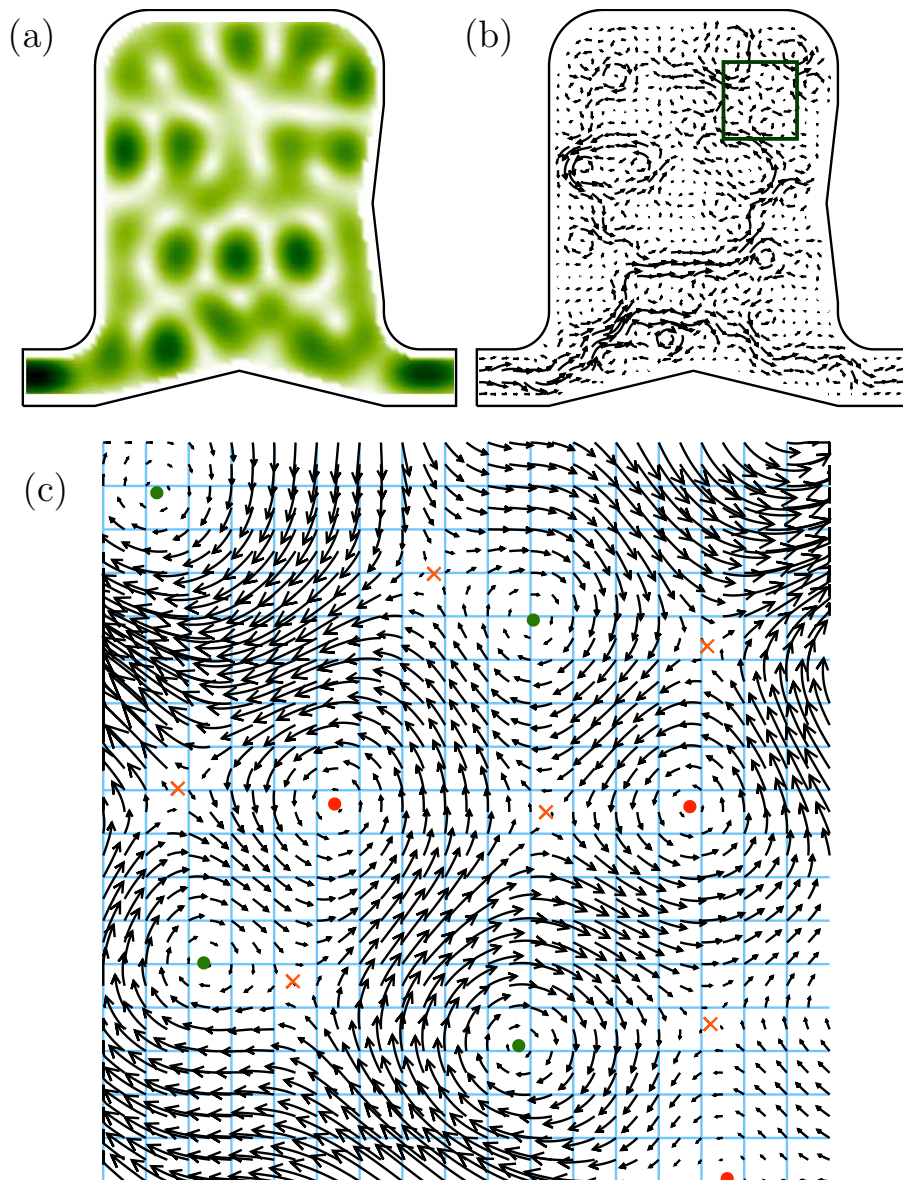


Figure 3.3.: Figure to illustrate critical points in open billiard systems. In this figure we show the intensity of the wave function in part (a) and the flow for the full wave function in part (b). Additionally we present a blowup of the flow pattern where we demonstrate the different type of critical points. Vortices are indicated by filled circles. The color code is such that if the flow curls clockwise around a vortex point it is green, in case of a counterclockwise rotation it is red.

grid. The flow in between the grid points has been obtained by a bilinear interpolation, which is described in more detail in appendix A.

In previous studies in our group the vortex points had been marked by hand. This method however failed in case of the saddle points. In this study we therefore applied the method of bilinear interpolation to estimate the nodal lines of each component of the flow. From the crossing points of the nodal lines of the flow components we obtain the position of the critical points. A detailed description of the nodal line estimation is

presented in appendix A. The second improvement which was important for the data analysis was to invent a method which classifies automatically the critical points. This method is based on the classification of fixed points used in Hamilton mechanics or in the theory of first order ordinary differential equations. This method is also presented in appendix B.

All distances between vortices or saddles are expressed in scaled distances:

$$R \equiv k|\vec{r}_2 - \vec{r}_1|, \quad (3.1)$$

where  $k$  is the wave number. Distances of vortices or saddles from the billiard boundary are also scaled and denoted by

$$Y \equiv ky, \quad (3.2)$$

where  $y$  is the shortest distance from the boundary. Since distances  $R, Y$  are scaled with respect to  $k$ , the experimental results for different frequencies  $\nu$  can be superimposed, improving the statistics.

All results presented in this section are submitted Phys. Rev. E in a joint publication with Juan Diego Urbina and Marc Dennis who have developed the theoretical description of the correlation functions discussed here. For completeness we have collected all formulas of the correlation functions to which we will compare our experimental results in appendix C.

### 3.3.2. Experimental results

#### Pair correlation functions

The vortex pair correlation function  $g_{vv}(R)$  (eq. C.4) describes the probability to find another vortex at the scaled distance  $R$ . A closely related quantity is the charged vortex pair correlation function  $g_Q(R)$  (eq. C.5) which is again the probability to find another vortex in distance  $R$  but weighted with the product of signs of the two involved vortices. Theoretical expressions for these correlation function have been obtained by A.I. Saichev et. al. [Sai01] and M. Dennis and M.V. Berry [Ber00, Den01] independently.

Figure 3.4 show the comparison between experiment and theory for the vortex-vortex pair correlation functions, both signed and unsigned in the low frequency regime. For small frequencies the distances between vortices is relatively large compared to the measurement grid which results in quite accurate estimation of the distances compared to the wavelength. We see in figure 3.4a a very good agreement between theory and experiment for small  $R$ . But in this limit the vortex distances become comparable with the system size  $L$ . Thus the boundary has an influence on the vortex correlation function which results in a smaller period length of the oscillations in the experimental data. This effect has been seen already in previous studies in our group [Eck99] and was also seen in numerical studies of the autocorrelation function in the limaçon billiard [Bäcke02]. We will focus on this topic in section 3.4.

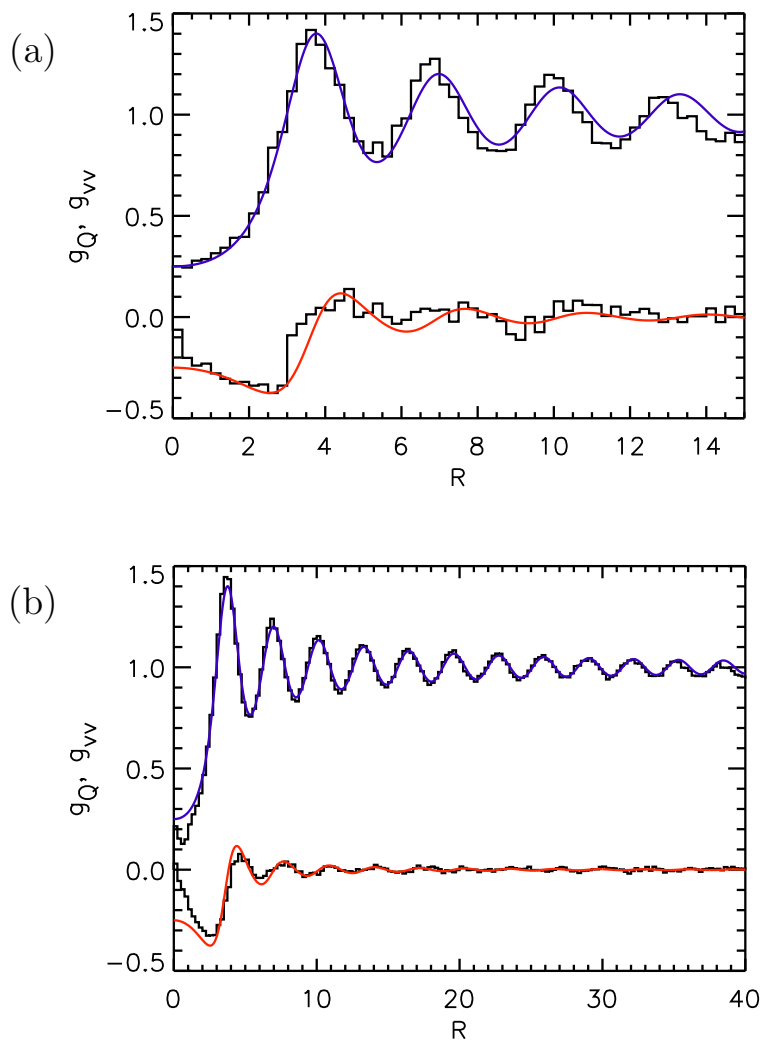


Figure 3.4.: Vortex pair correlation  $g_{vv}(R)$  and charge correlation function  $g_Q(R)$ , in (a) the low frequency regime ( $5 \text{ GHz} < \nu < 9 \text{ GHz}$ ), and (b) the high frequency regime ( $15 \text{ GHz} < \nu < 18.6 \text{ GHz}$ ). The solid lines correspond to the analytic prediction of RWM.

We have analyzed the vortex pair correlation function also for higher frequencies. This result is shown in figure 3.4b and it agrees perfectly with theory for large  $R$ , but the agreement is less good for small  $R$ . This is due to the limited spatial resolution in the measurement which fails to resolve distances comparable to the measurement grid size with sufficient accuracy. Experimental results for the vortex pair correlation function have been published already previously, though with by far poorer statistics [Bar02]. All other quantities shown in this section have not been published previously with one exception which is concerning parts of the nearest neighbor distance distributions.

Results for the saddle pair correlation function  $g_{ss}(R)$  and the vortex-saddle function  $g_{vs}(R)$  are plotted in figure 3.5a, with experimental data plotted against the asymptotic formulas (eq. C.9), (eq. C.8). The agreement between theory and experiment is very

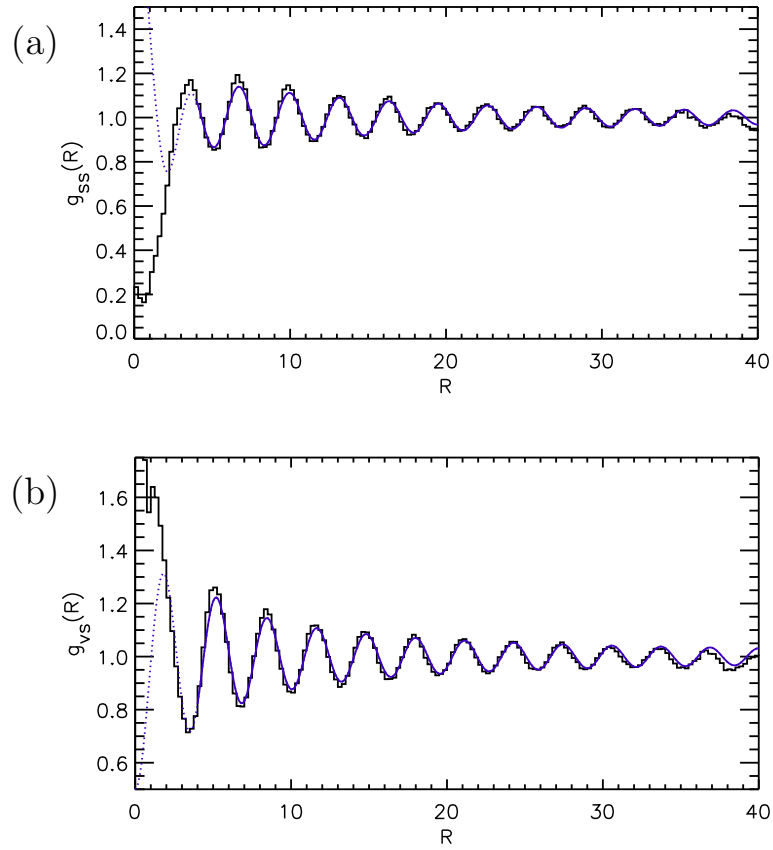


Figure 3.5.: Pair correlations involving saddle points: (a) saddle-saddle correlation function  $g_{ss}(R)$ ; vortex-saddle function  $g_{vs}(R)$ . Experimental data is plotted against the asymptotic forms of eqs. (C.8) and (C.9).

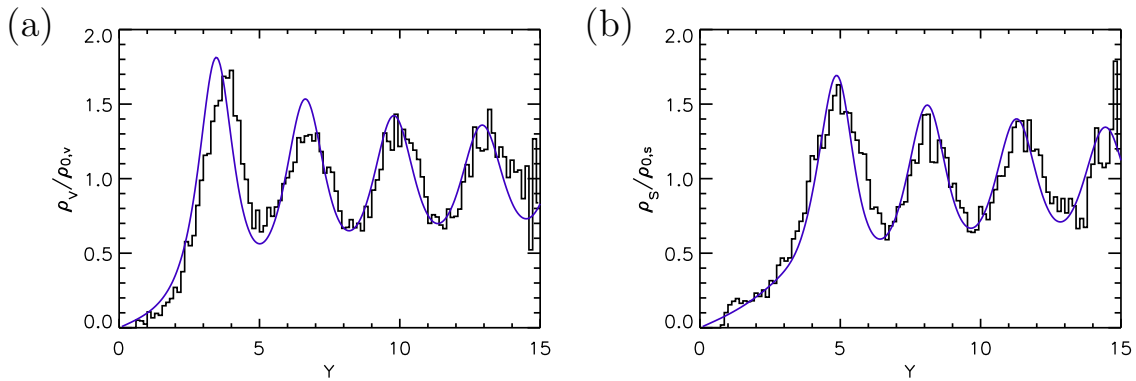


Figure 3.6.: Critical point density fluctuations as a function of scaled distance  $Y$  from a straight wall satisfying Dirichlet boundary conditions: (a) vortex density; (b) saddle density. Experimental data is plotted against the analytic forms of eqs. (C.11) and (C.12), for Dirichlet boundary conditions.

good for a wide range of  $R$ . But since we have only asymptotic expressions for the theoretical predictions, we can not compare our experimental results for values smaller than  $R = 3$ .

One way to take the metallic boundary of the experiment into account is to study the average vortex and saddle density fluctuations against a straight boundary satisfying Dirichlet conditions. Experimental measurements of this density fluctuations against the boundary are shown in figure 3.6, vortex fluctuations in the upper panel (with theoretical density from equation (C.11)), the lower panel the saddle fluctuations (with theoretical plot from equation (C.12)). As in the other presented cases the agreement between theory and experiment is good.

### Nearest neighbor distance distribution functions

Another correlation one can study is the Nearest Neighbor Distance Distribution for critical points in the flow. Theoretical results for these distributions can be obtained by the Poisson approximation [Sai01]. This approximation assumes that all points around a given critical point are statistically independent. This implies that one only has to take into account the correlations between the neighbors of one given vortex or saddle point i.e. the pair correlation function. Following the above mentioned reference one can calculate the distribution of nearest neighboring critical points approximately with the following formula

$$f(\ell) \approx 2\pi\ell g(\ell) \exp \left[ -2\pi \int_0^\ell z g(z) dz \right]$$

where  $\ell$  is the dimensionless length which is the distance of critical points divided by the mean distance of critical points. Since for vortex points the pair correlation function could be calculated exactly one can use the formula above. Whereas for correlations including saddle points we only have asymptotic results for large  $kr > 3$  and therefore calculations of the nearest neighbor distribution function is not yet possible. But one can use numerical results from the random plane wave approach for comparison with the experimental results.

In figure 3.7 we show different types of Nearest Neighbor Distributions depending on the combination of different types of critical points. In part (a) the distribution for vortices with the same sign is shown in (b) with opposite sign in (c) the sign was ignored. In part (d) we show the distribution of nearest neighbors for saddles only and in (e) the one for vortex and saddle points. We can see in all cases a reasonable good agreement between theory and experiment.

In this section we have analyzed pair correlation functions involving vortex and saddle points of the flow. Using the bilinear interpolation method it was possible to study also the saddle points. We have shown that for the pair correlation functions of critical points in the flow we get a very good agreement between theory and experiment. We have seen some deviations for the vortex pair correlation function for wave functions

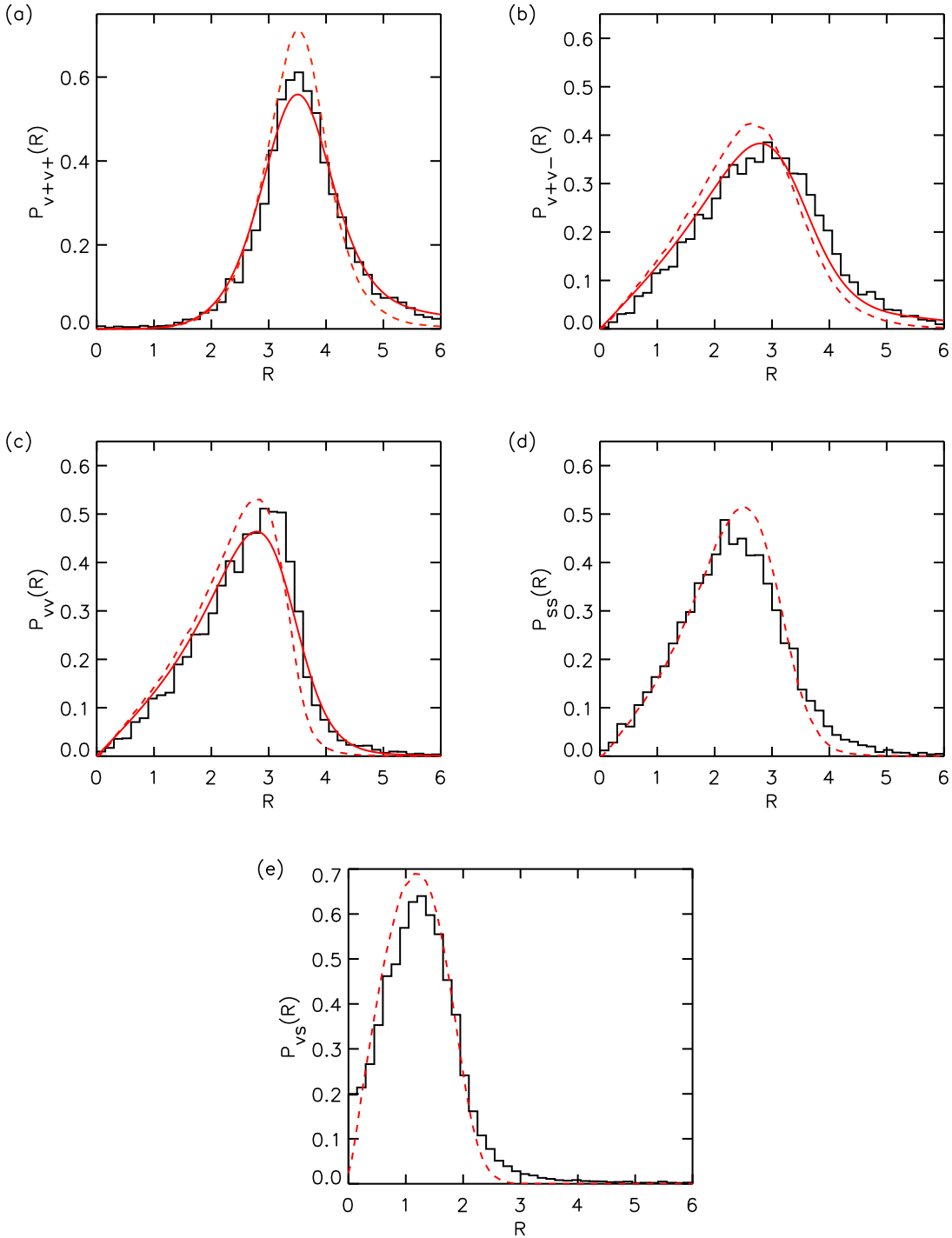


Figure 3.7.: The histograms show the experimental results for different Nearest Neighbor Distance Distributions of critical points in the flow. The solid line corresponds to the theoretical prediction in Poisson approximation. The dashed line corresponds to numerical simulations with random plane waves. In part (a) the distribution for vortices with the same sign is shown, in (b) with opposite sign, in (c) the sign was ignored. In part (d) we show the distribution of nearest neighbors for saddles only, and in (e) the one for vortex and saddle points.

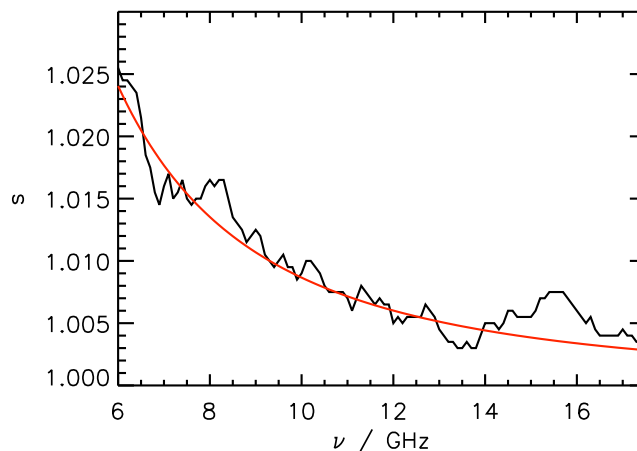


Figure 3.8.: Stretching factor  $s$  for the experimental pair correlation to reproduce the random plane wave prediction versus the frequency. The solid line corresponds to a fit with Eq. (3.5).

with wave lengths which are comparable to the system size. Here the boundary has to be included into the analysis. One way to do this is to measure the density of critical points against a straight wall. Here we also have found a good agreement. A second treatment of the boundary effects will be discussed in the next section. To complete the analysis of critical points we have also analyzed the nearest neighbor distribution function of critical points in the flow. In cases where theoretical predictions are not available we have compared our experimental results with numerical results obtained with the random plane wave model.

### 3.4. Boundary effects

In section 3.3.2 we have seen that the period length of the theoretical and experimental correlation function had disagreed. This effect of a miss match of the period length in correlation functions has been seen in experiments [Dörr98, Eck99] and it is also present in numerical studies [Aur93, Li94, Sre96, Bäcke02].

Here we want to turn to a more quantitative description of the influence of the boundary on the oscillation period. To this end we introduce a stretching factor  $s$  by replacing  $k$  by  $k_{\text{eff}} = sk$  in the theoretical expressions for the correlation functions, and determine  $s$  such that an optimal agreement with the experimental curves is obtained. In figure 3.8 the stretching factor for  $g_{\text{vv}}(R)$  is shown as a function of frequency. Each data point corresponds to the average over 100 different wave functions in a frequency range of 2 GHz. On the frequency axis the center of the frequency range is given. To neglect effects of the measurement resolution only data points with  $R$  larger than 5.3 have been taken into account. Additionally only data for  $R < kL_x$  where  $L_x$  is the smallest length scale of the billiard has been taken into the analysis. The figure shows clearly a decreasing

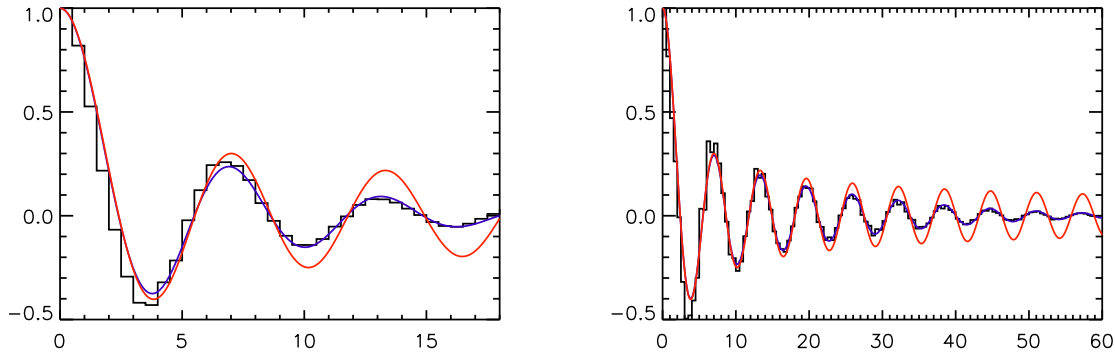


Figure 3.9.: In the left part the spatial autocorrelation function of the real part of a wave function is. This wave function was measured at a frequency of 5.4 GHz. In the right part the frequency has been 17.96 GHz. The red solid lines represents the theoretical prediction (eq. 2.29) according to the isotropic RWM. The blue solid line shows the adopted theory from equation 3.4.

behavior for the scaling factor which approaches to 1 with increasing frequency. This means the influence of the boundary on the pair correlation functions is getting smaller for higher frequencies.

This observation can be understood by considering the effect of a finite-size confinement on the bulk isotropic RWM. A basic assumption we have consistently made is that the random superposition of plane waves which define the ensemble of random waves has fixed energy. This is correct in the bulk, but any spatial confinement will induce a finite range on the distribution of wave numbers. Specifically, if  $L$  is a typical length describing the systems, wave numbers participating in the expansion of the exact state are smeared over a window  $\delta \simeq 1/L$  [Bäcke99]. Finite-size effects are then expected to produce an effective new correlation function given by

$$g_{\text{eff}}(kr) = \frac{1}{\sqrt{2\pi\delta}} \int e^{-\frac{(k'-k)^2}{2\delta^2}} g(k'r) dk'. \quad (3.3)$$

For oscillatory functions with an algebraic decay  $\sim (kr)^{-n}$  the integration yields

$$g_{\text{eff}}(kr) = g(k_{\text{eff}}r) e^{-\frac{\delta^2 r^2}{2}}, \quad k_{\text{eff}} = sk \quad (3.4)$$

with a stretching factor

$$s = 1 + n(\delta/k)^2. \quad (3.5)$$

A short derivation can be found in appendix D. The solid line in Fig. 3.8 is a fit of the experimental data with Eq. (3.5). From the fit a value of  $\delta = 19.5 \text{ m}^{-1}$  is obtained for the width distribution. The natural unit for wave numbers is the inverse of the square root of the density of states,  $\rho(k) = A/2\pi$ , where  $A$  is the billiard area. Expressing  $\delta$  in these units one obtains  $\delta\sqrt{A/2\pi} = 1.4$ . It is encouraging that a value close to one is such obtained, notwithstanding the only qualitative way of reasoning.

Encouraged by these results we have tested also the spatial auto correlation function of the real part of the wave function. In figure 3.9 we present the comparison between the experimental results of the auto correlation function and the theoretical predictions of the bulk RWM (red curve) and the new theory by equation 3.4 (blue curve). We see a very good agreement between the experimental data and the adopted RWM for waves in a bounded domain.

Here we can again perform a fit over all 681 wave functions for the spatial auto correlation function yielding a mean value for  $\delta$  of 15.3. If we express  $\delta$  again in units of the density of states we obtain  $\delta\sqrt{A/2\pi} \approx 1.13$

In this preliminary study we have included finite size effects into the theoretical description of correlation functions which have an oscillating behavior and decay algebraically with  $1/r^n$ . We have seen that if waves are confined to a bounded domain the correlation will have a shorter period length in its oscillations. This effect is supported by experimental findings in the vortex pair correlation function and the autocorrelation function of the real and imaginary part of the wave function in an open quantum billiard. In the latter case an additional Gaussian decay is seen which is predicted by our theory. For us yet unknown reasons this decay is absent in case of the pair correlation function of vortex points.

## 3.5. Stresstensor

### 3.5.1. Introduction

In this section we will focus on the Pauli quantum stress tensor (QST) for open planar chaotic billiards and its statistical properties. As we will see QST supplements previous studies of wave function statistics and flow patterns in an important way as it probes higher order derivatives (irrespective of choice of gauge) and thereby fine details of a wave function. QST was introduced by Pauli [Pau33, Pau80] already in 1933 but, in contrast to the corresponding classical entities for electromagnetic fields and fluids [Mis73], it did not get established as an useful quantity. On the other hand, studies of stress is in general an important part of material science research and, on a more fundamental atomistic level, it originates from quantum mechanics. The concept of stress had been applied to many fields in physics. Kinetic and configurational contributions to stress had been analyzed with efficient computational methods based on electronic structure calculations of solids [Nie85, Fol86, God88]. Due to the advances in nanomechanics the quantum-mechanical nature of stress [She04] becomes more important than a classical description of stress. Quantum stress has also been studied in atomic physics and chemistry [God90, Tao08]. As a last example we want to mention the quantum hydrodynamic simulations of transport properties of different quantum sized semiconductor devices like Resonant Tunneling Devices (RTD) and High Electron Mobility Transistors (HEMT) [Hönts04]. In total, QST is a fundamental concept in quantum mechanics that ties up with local forces and the flow of probability density. Hence it is natural to extend the previous studies of generic statistical distributions for open chaotic quantum

billiards to include also the case of stress. In the following parts of this section we will present our experimental results on the statistical properties of the QST. The theoretical results have been obtained by our collaborators K.-F. Berggren, D. N. Maksimov and A. F. Sadreev. A joint publication has been submitted to Phys. Rev. E [Ber08b].

### 3.5.2. Theoretical background

#### Definition

There is an ambiguity in the expression for the stress tensor because any divergence-free tensor may be added without affecting the forces [Rog02, Mar02]. For clarifying our definitions and the particular choice of the stress tensor we repeat the basic steps of Pauli's original derivation of his QST [Pau33, Pau80]. If  $\psi(\vec{x}, t)$  is a solution to the Schrödinger equation

$$i\hbar \frac{\partial \psi}{\partial t} = -\frac{\hbar^2}{2m} \Delta \psi + V \psi, \quad (3.6)$$

for a particle with mass  $m$  moving in the external potential  $V$  the components of the probability current density are

$$j_\alpha = \frac{\hbar}{2mi} (\psi^* \frac{\partial \psi}{\partial x_\alpha} - \psi \frac{\partial \psi^*}{\partial x_\alpha}). \quad (3.7)$$

Taking the time derivative of  $j_\alpha$  and using the right hand side of the Schrödinger equation above to substitute  $\partial \psi / \partial t$  Pauli arrived at the expression

$$m \frac{\partial j_\alpha}{\partial t} = - \sum_\beta \frac{\partial T_{\alpha\beta}}{\partial x_\beta} - \frac{\partial V}{\partial x_\alpha} |\psi|^2, \quad (3.8)$$

where  $T_{\alpha\beta}$  is his form of the quantum-mechanical stress tensor

$$T_{\alpha\beta} = \frac{\hbar^2}{4m} \left[ -\psi^* \frac{\partial^2 \psi}{\partial x_\alpha \partial x_\beta} - \psi \frac{\partial^2 \psi^*}{\partial x_\alpha \partial x_\beta} + \frac{\partial \psi}{\partial x_\alpha} \frac{\partial \psi^*}{\partial x_\beta} + \frac{\partial \psi^*}{\partial x_\alpha} \frac{\partial \psi}{\partial x_\beta} \right]. \quad (3.9)$$

In our case of planar billiards  $V$  may be put equal to zero and it is in that form that we will explore eq. (3.9). The kinetic Pauli QST is sometimes referred to as the quantum-mechanical momentum flux density, see e.g. Ref. [God88]. From now we will simply refer to it as QST.

#### Interpretation

To get a more intuitive understanding in classical terms of, for example, quantum-mechanical probability densities and the meaning of quantum stress (see e.g. Refs. [BB92, Hol93, Wya05]), we may follow one of the earliest physical interpretations of the

Schrödinger equation by Madelung who introduced the hydrodynamic formulation of quantum mechanics already in 1927 [Mad27]. Madelung obtained the QM hydrodynamic formulation by rewriting the wave function  $\psi$  in polar form as

$$\psi(\vec{x}, t) = R(\vec{x}, t) e^{iS(\vec{x}, t)/\hbar}. \quad (3.10)$$

The probability density is then  $\rho = R^2$ . By introducing the velocity  $\vec{v} = \nabla S(\vec{x}, t)/m$  the probability density current or probability flow is simply  $\vec{j} = \rho\vec{v}$ . Intuitively this is quite appealing. Inserting the polar form in the Pauli expression for  $T_{\alpha\beta}$  in eq. (3.9) we then have

$$T_{\alpha,\beta} = \frac{\hbar^2}{4m} \left( -\frac{\partial^2 \rho}{\partial x_\alpha \partial x_\beta} + \frac{1}{\rho} \frac{\partial \rho}{\partial x_\alpha} \frac{\partial \rho}{\partial x_\beta} \right) + \rho m v_\alpha v_\beta. \quad (3.11)$$

There are two qualitatively different terms in eq. (3.11), a quantum-mechanical term  $\tilde{T}_{\alpha\beta}$  that contains the factor  $\hbar$  and therefore vanishes in the classical limit  $\hbar \rightarrow 0$ , plus the “classical” contribution  $\rho m v_\alpha v_\beta$  which remains in the classical limit. Using the notations above eq. (3.8) gives the quantum hydrodynamic analogue of the familiar classical Navier-Stokes equation for the flow of momentum density  $m\rho\vec{v}$

$$m \frac{\partial \rho v_\alpha}{\partial t} = - \sum_{\beta} \nabla_{\beta} T_{\alpha\beta} - \rho \nabla_{\alpha} V. \quad (3.12)$$

Alternatively the Schrödinger equation may be rewritten in terms of the two familiar hydrodynamic equations in the Euler frame [BB92, Hol93, Wya05]

$$\frac{\partial \rho}{\partial t} + \nabla \cdot [\rho \vec{v}] = 0 \quad (3.13)$$

$$\frac{\partial \vec{v}}{\partial t} + [\vec{v} \cdot \nabla] \vec{v} = \vec{f}/m + \vec{F}/m, \quad (3.14)$$

where the external force is due to external potential

$$\vec{f} = -\nabla V, \quad (3.15)$$

and the internal force is due to the quantum potential

$$\vec{F} = -\nabla V_{QM}, \quad V_{QM} = -\frac{\hbar^2}{2m} \frac{\nabla^2 R}{R}. \quad (3.16)$$

Then the internal force can be expressed by a stress tensor for the probability fluid as

$$F_{\alpha} = - \sum_{\beta} \frac{1}{\rho} \frac{\partial \tilde{T}_{\alpha\beta}}{\partial x_{\beta}}. \quad (3.17)$$

Thus we are dealing with a “probability fluid” in which flowlines and vorticity patterns are closely related to QST.

### 3.5.3. Experimental results

Generally there are obvious measurement problems associated with QST for a quantum billiard, among them the limited spatial resolution presently available (see e.g. Ref. [Cro03]). Again it is possible to use the analogy between the Helmholtz and the Schrödinger equation to study the statistical properties of the QST. For this study we use the transmission data which has been measured from the source to the probe antenna on the frequency range from 5.5 to 10 GHz with a step size of 20 MHz, corresponding to wave lengths from 3 to 5 cm. As we probe here directly the field or better its second derivative which is very sensitive to fluctuations we have to assure that the leak current into the probe antenna can be neglected.

To check this we compared the experimentally obtained distribution of wave function intensities  $\rho = |\psi|^2$  with the theoretical predictions. In the case of an open billiard the wave function becomes complex. The strength of the openness can be described by a parameter  $\epsilon$  which can be calculated directly from the real and imaginary part of the experimentally obtained wave function:

$$\epsilon = \langle v^2 \rangle / \langle u^2 \rangle, \quad (3.18)$$

where  $u = \text{Re}\psi$  and  $v = \text{Im}\psi$ . In this calculation one has to ensure that  $u$  and  $v$  are uncorrelated ( $\langle uv \rangle = 0$ ), which can be obtained by applying a proper phase rotation [Sai02]). The intensity distribution of a partially open system is described with the modified Porter-Thomas distribution (see e.g. Ref. [Sai02])

$$p(|\psi|^2) = \mu \exp(-\mu^2 |\psi|^2) I_0\left(\mu \sqrt{\mu^2 - 1} |\psi|^2\right) \quad (3.19)$$

where

$$\mu = \frac{1}{2} \left( \epsilon + \frac{1}{\epsilon} \right). \quad (3.20)$$

Whenever  $\chi^2$ , the weighted squared difference of the experimental data and the modified Porter-Thomas distribution, was below  $\chi_{\text{cutoff}}=1.1$  the pattern has been selected for the final analysis of the statistics for the QST components.

Since the wave functions are experimentally known, including their phases, the quantum-mechanical probability density  $\vec{j} = \text{Im}\psi^* \nabla \psi$ , and the components of the QST can be obtained from the measurement. As an example Fig. 3.10 shows the intensity (a) and the phase (b) of the measured field at one frequency, as well as the probability current (c) and different components of the stress tensor (d - f).

The analysis of the data has been performed in dimensionless coordinates  $\vec{x} = k\vec{r}$ . Since  $u$  and  $v$  are two independent random wave fields we may rescale the imaginary part to obtain  $\epsilon$  values of one, thus mapping the experimental result to the situation of a completely open billiard. This step made it easy to superimpose the results from many field patterns of different frequencies which originally had different  $\epsilon$  values. For the analysis all wave functions passing the  $\chi^2$  test mentioned above have been used. Altogether 83 of 225 possible patterns have been taken in the analysis.

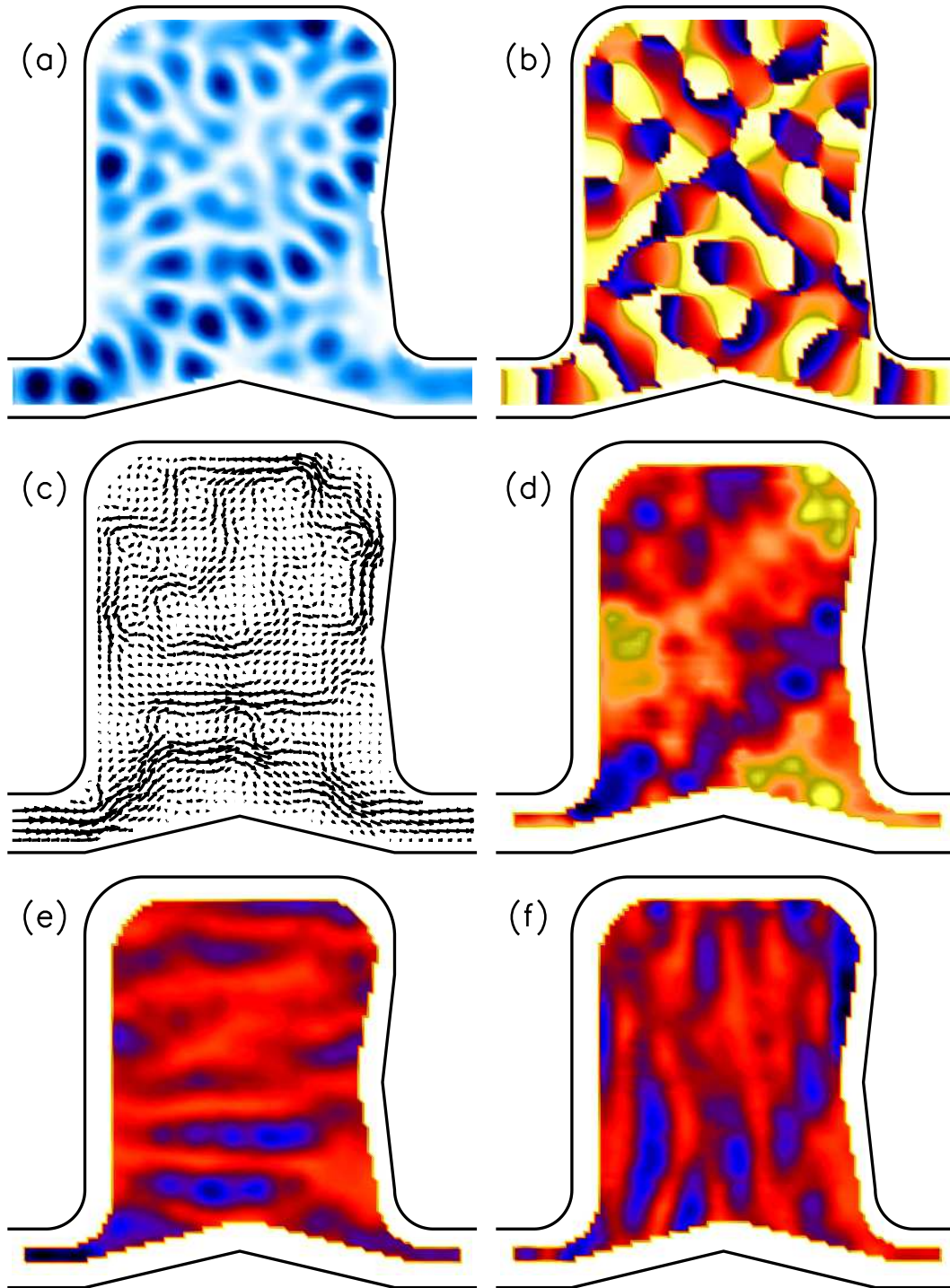


Figure 3.10.: The figure shows different quantities obtained from the measurement at the frequency  $\nu = 8.5$  GHz. In (a) the intensity of the wave function is shown and in (b) its phase. The plot (c) shows the Poynting vector of the system being equivalent to the probability current density in quantum mechanics. In (d)-(f) different components of the QST are shown, namely  $xy$  (d),  $xx$  (e) and  $yy$  component (f). Dark areas indicate higher values.

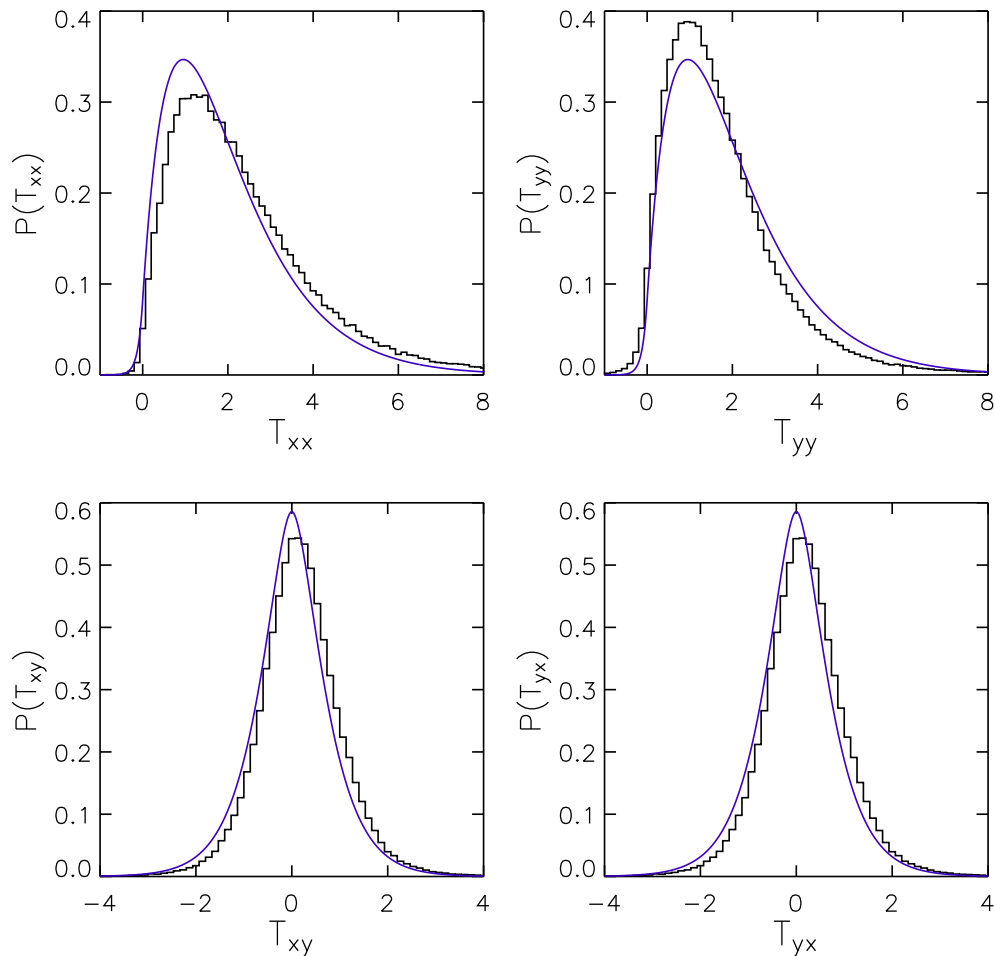


Figure 3.11.: Results for the experimental statistical distributions for the components of the QST stress tensor obtained by a superposition of all experimental data scaled to  $\epsilon = 1$  as explained in text. The solid lines correspond to the theoretical predictions in section 3 of [Ber08a] for  $\epsilon = 1$ .

Figure 3.11 show the distributions of the QST components obtained in this way. In addition the theoretical curves are shown as solid lines. From the figure we see that there is a good overall agreement between experiment and theory, but also that non-statistical deviations are unmistakable.

Deviations between experiment and theory had been found by us already in the past in an open microwave billiard, similar to the one used in the present experiment, in the distribution of current components [Bar02, Kim03a]. For the vertical  $y$  component a complete agreement between experiment and theory was found, but for the horizontal  $x$  component the experimental distribution showed, in contrast to theory, a pronounced skewness. The origin of this discrepancy was a net current from the left to the right due to source and drain in the attached wave guides. In a billiard with broken time-reversal symmetry without open channels a complete agreement between experiment and theory had been found, corroborating the net current hypothesis.

For a quantitative discussion of the net current we introduced for each pattern the normalized net current by

$$\vec{j}_{\text{net}} = \frac{\langle \vec{j} \rangle}{\langle |\vec{j}| \rangle}. \quad (3.21)$$

where the average is over all positions in the shaded region in Fig. 3.1. In Fig. 3.12 the  $y$  component of  $\vec{j}_{\text{net}}$  is plotted versus its  $x$  component for each wave function. One notices an average net current pointing from left to right, with an angle of about twenty degrees in upward direction. For the analysis we discriminated between three regimes for the strength of the net current. Additionally we performed a coordinate transformation such that for each pattern the vector of the net current is aligned along the positive  $x$ -axis. This rotation has been done for all experimental and numerical results in this section.

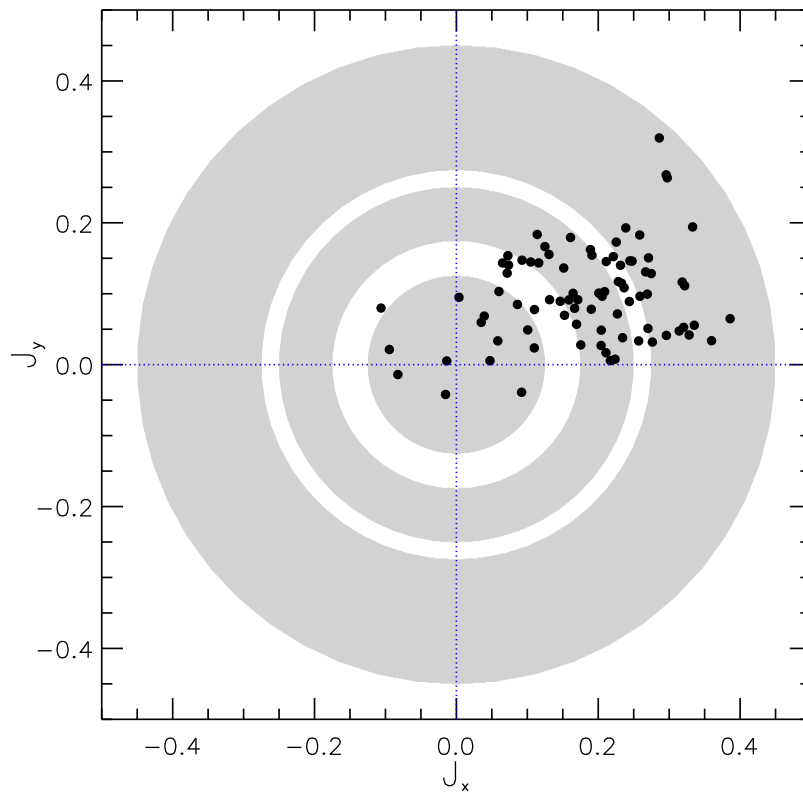


Figure 3.12.: Plot of the net current as it is defined in Eq. (3.21). The shaded regions are indicating three different regimes of net current strength which had been used in the later analysis.

In Fig. 3.13 the results for the three different regimes of net current strengths are shown. For the distributions of the  $xx$  and the  $yy$  component of the QST a clear dependence on the net current strength is found, where the deviations from theory increase with increasing net current.  $T_{xy}$  is only slightly affected by the net current, if at all. In the limit of small net currents all experimental distributions approach the theoretical ones.

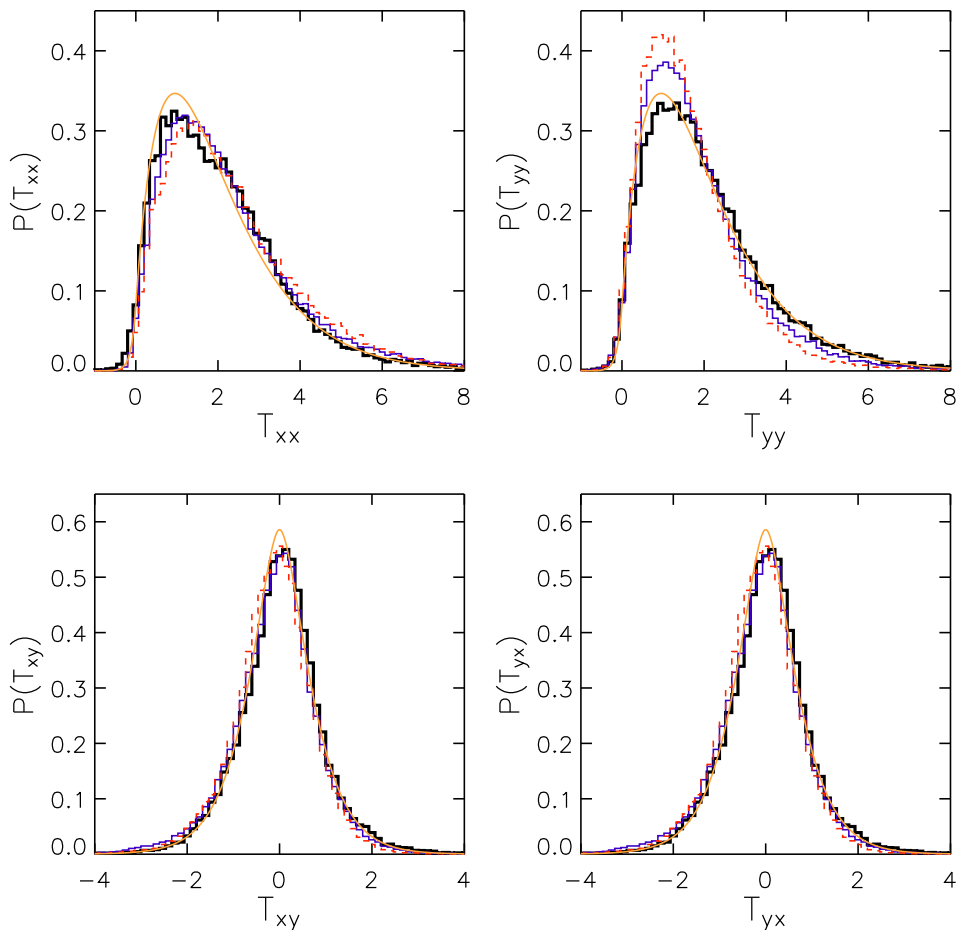


Figure 3.13.: Histograms of the QST distributions obtained from experimental data. The thick lines corresponds to the smallest net currents (see Fig. 3.12), the thin lines to intermediate ones and the dashed lines to ones with the largest net current. As in Fig. 3.11 the solid lines correspond to the theoretical predictions in section 3 of [Ber08a] for  $\epsilon = 1$ .

To test further the influence of the net current on the distributions of the stress tensor we performed a numerical simulation with random plane waves. Each random wave field was calculated on an area of  $500 \text{ mm} \times 500 \text{ mm}$ , with a grid size of  $2.5 \text{ mm}$ . The random wave field consisted of  $N = 500$  plane waves with random directions and amplitudes. The frequency used for the numerics was  $\nu = 5 \text{ GHz}$ . To introduce the net current we first performed a random superposition of plane waves according to Eq. (2.20), and then added a normalized plane wave with the wave vector  $K'$  pointing in the same direction as the net current observed in the experiment,

$$\psi(r) = \frac{1}{\sqrt{A}} \left( a' e^{iK' \cdot r} + \sum_{n=1}^N a_n e^{i\vec{k}_n \cdot \vec{r}} \right). \quad (3.22)$$

The strength of the resulting net current was adjusted by a prefactor  $a'$ . The best agreement between the experiment and the numerics was found for  $a' = 0.45$ . To get sufficient statistics we averaged over 200 different wave functions. In figure 3.14

we present the distribution of net currents for the numerical simulation. We see a much larger cloud in comparison to the experimental distribution of the net currents. However, with this distribution we got the best agreement between the simulation and the experimental data if we use figure 3.11 as a reference.

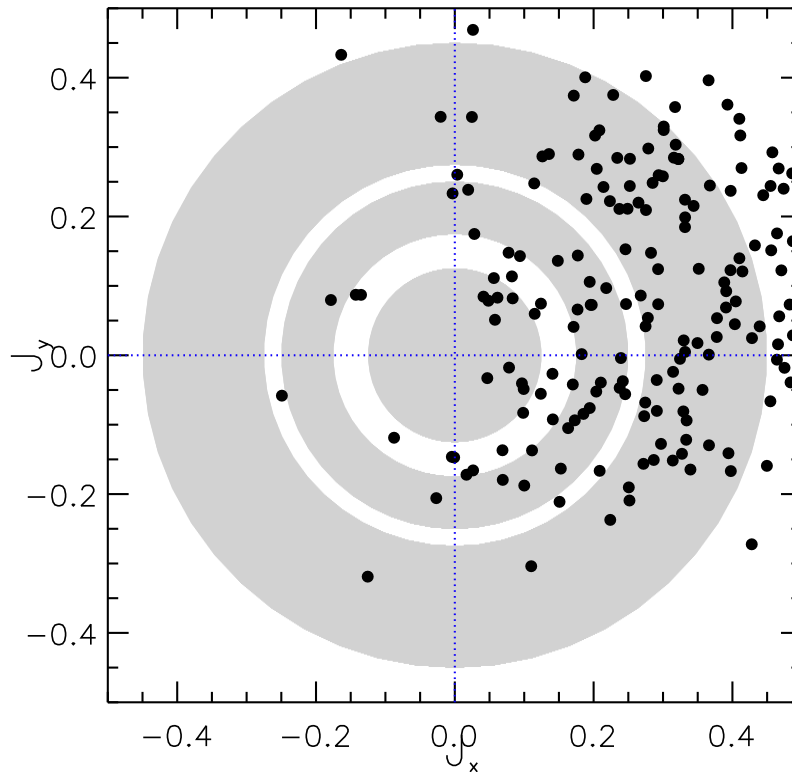


Figure 3.14.: Plot of the net current of the numerical data. For the following data processing the same selection rules have been applied as for the experimental data.

Fig. 3.15 shows the distributions for the QST components for numerical data derived from Eq. (3.22). The left part shows the distribution of the QST components without any special data processing. This corresponds to figure 3.11 for the experimental data. In the right part of the figure we present the numerical data after discriminating between different regimes of the net current. Here the same three regimes for the net current as for the experimental study have been used. Additionally we have again applied the coordinate transformation to align all net currents along the x-axis. The results from this type of simulation are in good qualitative agreement with the experimental results. In particular the deviations from the theory in Section 3 of Ref. [Ber08b] increase monotonically with the net current, just as in the experiment.

In summary we have seen that the experimental data coincides qualitatively with the theoretical predictions for the distributions of the QST components. If we consider the presence of a net current, the deviations can be explained at least qualitatively by numerical simulations with random plane waves.

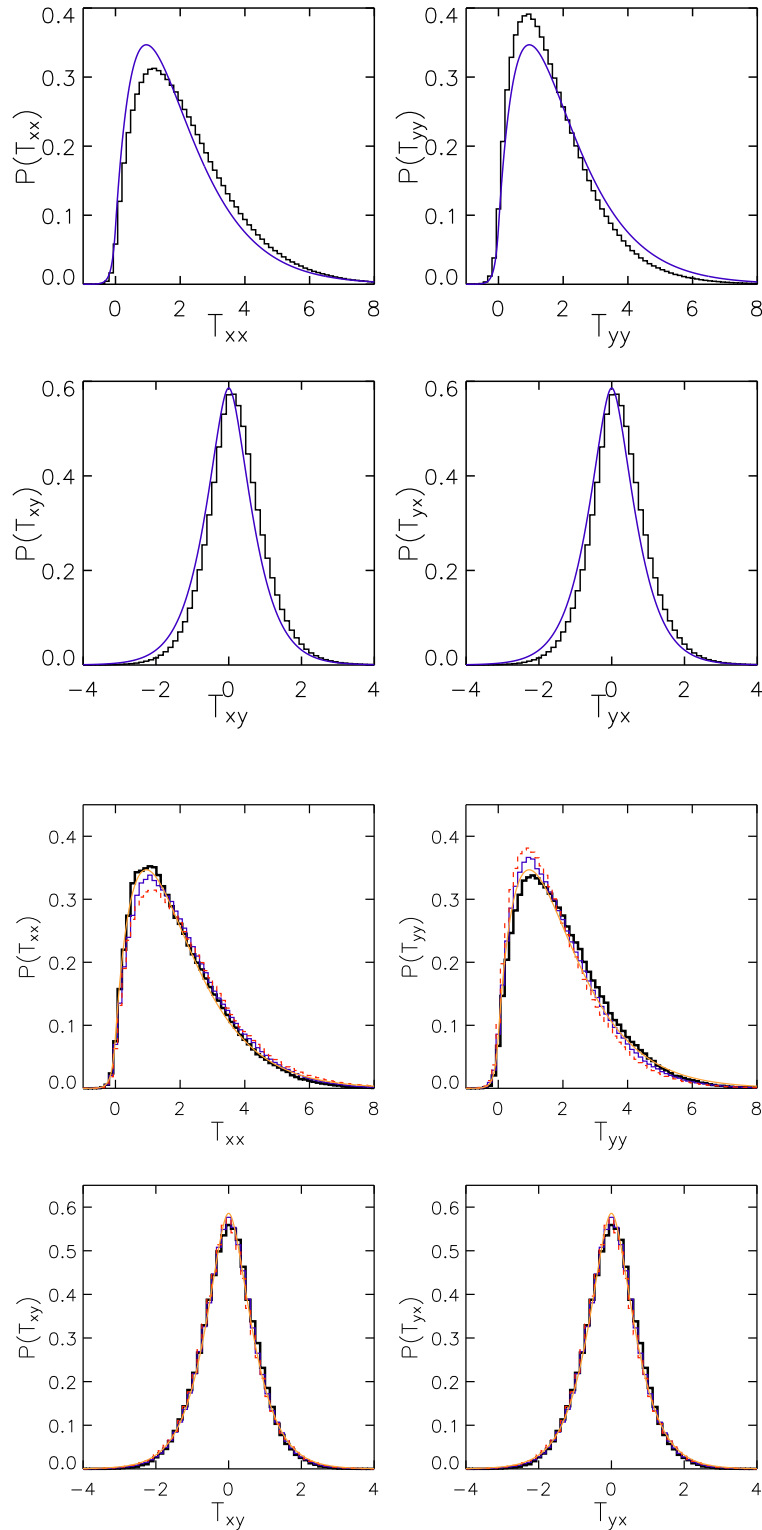


Figure 3.15.: Histograms of the QST components obtained from the simulations according to the wave function in Eq. (3.22). The upper four plots show the distributions of the QST components in the same way as in figure 3.11 for the experimental data. In the lower part the data is presented after discriminating the three net current regimes and after the application of the coordinate rotation (see text for details). As above the thick lines correspond to low, thin to intermediate and dashed lines to large net currents.

# 4. Fidelity of local perturbations

## 4.1. Introduction

Since the introduction of the concept of fidelity 25 years ago by Peres [Per84] it has attracted many attention. The idea of this concept is to quantify the stability of a quantum system against perturbations. It was defined as the overlap of two identical initial states which undergo two slightly different time evolutions. Expressed in an equation the fidelity amplitude reads:

$$f(t) = \langle \psi_0 | e^{2i\pi H_0 t} e^{-2i\pi H_1 t} | \psi_0 \rangle \quad (4.1)$$

Here  $\psi_0$  is the initial state,  $H_0$  the unperturbed and  $H_1 = H_0 + \lambda V$  the perturbed Hamiltonian. With the perturbation parameter  $\lambda$  the strength of the perturbation  $V$  can be varied. The time  $t$  is given in units of the Heisenberg time  $t_H = \hbar/\Delta E$  with  $\Delta E$  the mean level spacing. We will express all times in this chapter in units of the Heisenberg time. The fidelity  $F(t)$  is then defined as the modulus square of the fidelity amplitude.

A similar concept has already been developed to describe the spin echo experiments of nuclear magnetic resonances in the middle of the last century (see reference [Abr61] for a review). The strong interest nowadays is due to the quite new field of quantum computation. In this research field the stability of the quantum mechanical system against perturbations is of large importance [Fra04].

Roughly speaking there exist three different regimes for the behavior of the fidelity which are depending on the perturbation strength  $\lambda$ . In the *perturbative regime*  $\lambda$  is much smaller than the mean level spacing of the unperturbed system. This means the perturbation is so small that we can use first order stationary perturbation theory to calculate an expression for the fidelity amplitude. If we use the first order of the perturbation expansion we obtain for the fidelity amplitude

$$f(t) \simeq \langle \psi_0 | e^{-2\pi i \lambda V_{\text{diag}} t} | \psi_0 \rangle, \quad (4.2)$$

where  $V_{\text{diag}}$  is the diagonal component of the perturbation in the basis of the unperturbed system  $H_0$ . Assuming now that these diagonal elements are Gaussian distributed one can calculate the averaged fidelity amplitude:

$$\langle f(t) \rangle \approx e^{-2\pi^2 \lambda^2 \langle V_{\text{diag}}^2 \rangle t^2} \quad (4.3)$$

We see from eq.(4.3) that the decay of the fidelity amplitude is Gaussian in time for the *perturbative regime*.

The second regime is called *Fermi golden rule regime*, here the perturbation strength  $\lambda$  is comparable to the mean level spacing of the unperturbed system. In this regime we obtain for the fidelity amplitude an exponential decay where the decay constant could be obtained using Fermi's golden rule [Cer02, Van03]. There has also been a random matrix approach in the linear response limit from Gorin et al. [Gor04]. They could show the transition from Gaussian to exponential decay for increasing perturbation strength.

Later on it was possible for Stöckmann et. al. [Stöck04] to calculate an exact result for the fidelity for arbitrary perturbation strength  $\lambda$ . These calculations were done using super symmetric calculation techniques.

The third regime which is discussed in literature is the Lyapunov regime. Here the perturbation strength exceeds the mean level spacing by far. The result is an exponential decay which is independent on the perturbation strength  $\lambda$  but where the decay rate is related to the Lyapunov exponent of the underlying classical dynamics. This regime cannot be treated with techniques from random matrix theory as here system specific features play the major role for the fidelity decay.

### 4.1.1. How to measure fidelity

A measurement unavoidable disturbs the system one is interested in. Therefore it is difficult to measure directly the fidelity of a system as it was defined in eq. (4.1). This led Schäfer et al. [Sch05] to the definition of the scattering fidelity  $f^{\text{scat}}(t)$ :

$$f^{\text{scat}}(t) = \frac{\hat{C}[S_{ab}, S_{ab}^{(\lambda)*}](t)}{\sqrt{\hat{C}[S_{ab}, S_{ab}^*](t) \cdot \hat{C}[S_{ab}^{(\lambda)}, S_{ab}^{(\lambda)*}](t)}}. \quad (4.4)$$

Here  $S_{ab}$  is a scattering matrix element, and  $\hat{C}[S_{ab}, S_{ab}^{(\lambda)*}](t)$  the Fourier transform of the cross-correlation function of the respective matrix elements. As it was shown in [Sch05] the Fourier transform of the cross-correlation function can be expressed as

$$\hat{C}[S_{ab}, S_{ab}^{(\lambda)*}](t) = \left\langle \hat{S}_{ab}(t) \hat{S}_{ab}^{\lambda*}(-t) \right\rangle, \quad (4.5)$$

where the brackets denote an average over an ensemble, an energy window or both. This ansatz is limited to cases where the measuring antenna is weakly coupled and the classical dynamic is chaotic. Experimentally it has been shown that the measured scattering fidelity matches very good the theoretical predictions using the linear response result of Gorin et al. [Gor04]. The perturbation parameter which was the only free parameter has been obtained independently using the variance of the level velocities. We will do the same when we study our experimental results of the fidelity for a local perturbation.

### 4.1.2. Level distributions for local perturbations

Before we show the results of the fidelity for a local perturbation we want to recapitulate some older results which have been measured and discussed eight years ago in our group. There we have compared the distribution of level velocities for a local perturbation with those of a global perturbation.

In this former study a perturbation was called *global* if it gives rise to a total rearrangement of the wave functions and the spectrum already for a moderate perturbation. In this case the level velocities are Gaussian distributed as predicted from random matrix theory. All results discussed above for the fidelity are also obtained using global perturbations.

A perturbation is called *local* if it affects the wave functions only locally. To achieve a local perturbation a small disk can be introduced into the billiard and can then be moved through the billiard. That a small disk affects the wave function only locally is used in the perturbing beat method which is used to measure the eigenfunctions of a billiard system. The technique uses the fact that the introduction of a small disk or better a point-like impurity causes a shift of the eigenenergy by

$$\Delta E_n = \alpha |\psi_n(r)|^2, \quad (4.6)$$

where  $\alpha$  describes the strength of the perturbation, and  $\psi_n$  is the wave function at the scatterer position in the absence of the scatterer.

Using the random plane wave assumption from Berry it is possible to calculate the distribution function of the level velocities for a local perturbation yielding

$$P(v) = \frac{\beta}{\pi} K_0(\beta|v|), \quad (4.7)$$

where  $K_0(x)$  is a modified Bessel function, and  $\beta = A/(\sqrt{2}\alpha k)$  ( $A$ : billiard area,  $k$ : wave number). In the appendix the variance of the level velocities is shown to be

$$\langle v^2 \rangle = \int_{-\infty}^{\infty} v^2 P(v) = \frac{1}{\beta^2} \quad (4.8)$$

From the variance of the level velocity distribution we can obtain the perturbation strength. Thereby we can compare our experimental results with the theory without any free parameter

## 4.2. Experimental setup

Even though the experiment has been measured long time ago and the details of the setup are described in several publications, we want to repeat the main aspects of the experimental setup. The system studied was a rectangular microwave billiard with

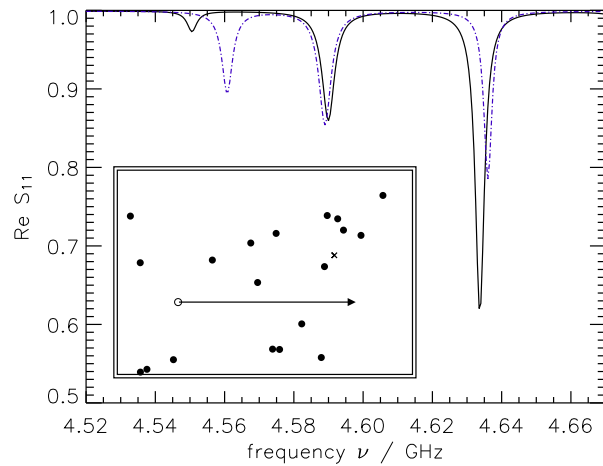


Figure 4.1.: Part of the reflection spectrum for two perturber positions differing by  $|\Delta r| = 4$  mm. The inset shows a sketch of the used microwave billiard (scatterers are shown three times larger). The antenna position is marked by a cross.

height  $h = 8$  mm, side lengths  $a = 340$  mm,  $b = 240$  mm and 19 disks with a diameter of  $D = 4.6$  mm placed randomly inside the billiard (see inset of Fig. 4.1). Another disk of the same size has been moved in steps of 1 mm through the billiard. With a fixed wire antenna we measured the reflection spectrum for 300 different positions of the moving disk in a frequency range from 3.5 to 6 GHz. In this frequency range the billiard can still be treated as two-dimensionally, and there is a complete agreement with the corresponding quantum mechanical system [Stöck99]. Figure 4.1 shows part of the reflection spectrum for two slightly different positions of the movable disk. In addition we measured the eigenfunctions [Ste92] to make sure that they are delocalized and their intensities Porter-Thomas distributed. In the measured frequency regime it was also possible to extract resonance positions and amplitudes from the spectrum by a Lorentz fit. These quantities will be needed later for the determination of the ordinary fidelity.

### 4.3. Theoretical model

In this section an expression for the fidelity amplitude shall be derived. First we shall derive an explicit expression of the fidelity decay caused by the shift of a local perturber. We assume that the system is completely chaotic (in the experiment this was verified by measuring the eigenfunctions, see above). In this case we may average expression (4.1) over all possible initial states resulting in

$$f(t) = \frac{1}{N} \text{Tr} \left( e^{2\pi i H_0 t} e^{-2\pi i H_1 t} \right), \quad (4.9)$$

where  $N$  is the number of states taken in the trace. In the present case  $H_0$  and  $H_1$  correspond to the Hamiltonian of the billiard with the perturber placed at two different

positions. For a weak, point-like perturbation, the perturber just produces a positive shift of the eigenenergy proportional to the intensity  $|\psi|^2$  of the unperturbed wave function at the perturber position, see eq. (4.6), i.e. the Hamiltonian in the basis of the unperturbed system is given by

$$H_{nm}(r) = \delta_{nm}(E_n^0 + \alpha|\psi_n(r)|^2), \quad (4.10)$$

where  $E_n^0$  are the eigenenergies of the unperturbed system and  $r$  the position of the scatterer. For this approach to be valid it is essential that the shift induced by the perturber is always small compared to the mean level spacing, i.e. we never leave the perturbative regime. We then obtain from Eqs. (4.2) and (4.9)

$$f(t) = \left\langle e^{2\pi i \alpha (|\psi_1|^2 - |\psi_2|^2)} \right\rangle, \quad (4.11)$$

where the abbreviation  $\psi_i = \psi(r_i)$  has been used. The brackets denotes the average over all  $N$  participating states. To calculate this average, we now apply the random plane wave assumption. The average is most conveniently expressed in the following way [Sre96],

$$f(t) = \frac{\sqrt{|K|}}{2\pi} \iint d\psi_1 d\psi_2 e^{2\pi i \alpha (|\psi_1|^2 - |\psi_2|^2)} \times e^{-\frac{1}{2}(\psi_1, \psi_2) K (\psi_1, \psi_2)^T}, \quad (4.12)$$

where  $K$  is a  $(2 \times 2)$ -matrix of which the inverse

$$K^{-1} = \begin{pmatrix} \langle \psi_1 \psi_1 \rangle & \langle \psi_1 \psi_2 \rangle \\ \langle \psi_2 \psi_1 \rangle & \langle \psi_2 \psi_2 \rangle \end{pmatrix} \quad (4.13)$$

can be expressed in terms of two-point correlation functions only. Using again the model of random plane waves [Ber77] the two-point correlation function can be calculated yielding  $\langle \psi_i \psi_j \rangle = \frac{1}{A} J_0(k|r_i - r_j|)$ . Performing the integrations one obtains the final expression for the fidelity amplitude

$$f(t) = [1 + (\lambda t)^2]^{-\frac{1}{2}}, \quad (4.14)$$

where

$$\lambda = \frac{4\pi\alpha}{A} \sqrt{1 - J_0^2(k|\Delta r|)}. \quad (4.15)$$

$|\Delta r|$  is the shift of the scatterer. For large  $t$  the fidelity amplitude decays algebraically with  $f(t) \sim 1/t$ . The only free parameter in Eq. (4.15) is  $\alpha$ . This parameter can be obtained independently from the variance of the level velocities, see Eq. (4.8). This allows us to compare the experimental results with theory without any free parameter.

## 4.4. Results

Figure 4.2 shows the scattering fidelity, as obtained from eq. (4.4), for three different perturber shifts. The solid lines correspond to the theoretical prediction from eq. (4.14).

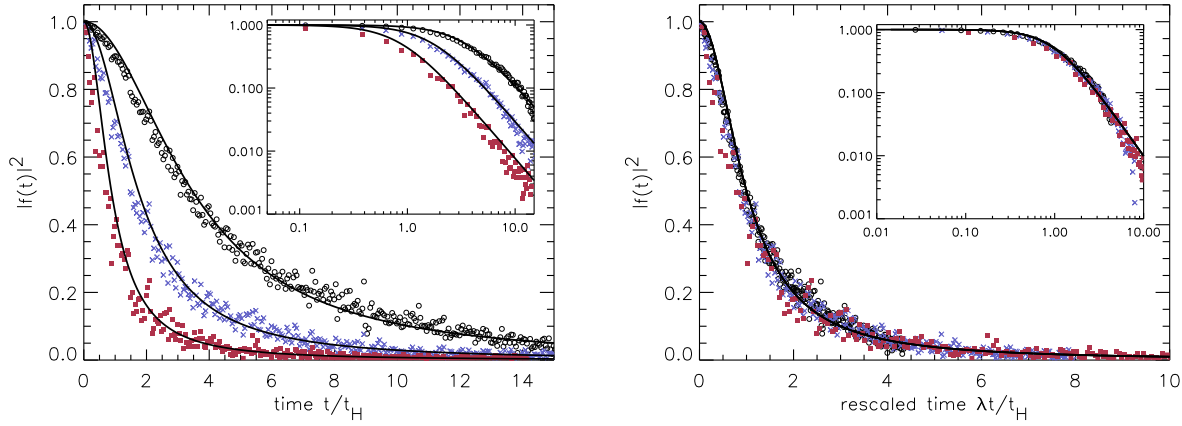


Figure 4.2.: In the left part the results of the scattering fidelity for different shifts of the perturber  $|\Delta r| = 1$  mm (open circles, black), 2 mm (crosses, blue), and 4 mm (filled squares, red) is shown. The solid line corresponds to the theoretical prediction of eq. (4.14). The results were obtained for the frequency range from 3.5 to 6 GHz. The insert shows the same results in a double-logarithmic plot. The right part of the figure presents the same data but on a rescaled time axis according to  $t' = \lambda t$ .

A good agreement between theory and experiment is found in all cases, apart from minor systematic deviations for small times. Values obtained for the coupling parameter  $\alpha$  by a fit deviate from those from the level velocities by a few %. The inset shows the results in a double-logarithmic plot illustrating the algebraic decay for long times  $t$ . Equation (4.14) exhibits a scaling behavior: On a rescaled time axis  $\lambda t$  all experimental results should fall onto one single curve. In the right part of figure 4.2 we demonstrate that this is indeed the case.

So far we have discussed the results for the scattering fidelity. Let us now see, how the ordinary fidelity (4.1) can be obtained. Since the measurement has been performed at a fixed antenna position  $r_0$ , the initial state is localized at  $r_0$ , i. e.  $|\psi_0\rangle = |r_0\rangle = \delta(r - r_0)$ . Expanding  $|\psi_0\rangle$  in terms of eigenfunctions  $|\psi_n^1\rangle$  of  $H_1$ , and  $\langle\psi_0|$  in terms of eigenfunctions  $\langle\psi_n^0|$  of  $H_0$ , eq. (4.1) reads

$$f(t) = \sum_{n,m} \psi_n^0(r_0) \psi_m^1(r_0) e^{2\pi i(E_n^0 - E_m^1)t} \langle\psi_n^0|\psi_m^1\rangle. \quad (4.16)$$

The shift of the energy is a first order effect of the perturber, the change of the eigenfunctions being of the next order. Neglecting these higher order effects, we may approximate  $\langle\psi_n^0|\psi_m^1\rangle \approx \delta_{nm}$  to obtain

$$f(t) = \sum_n \psi_n^0(r_0) \psi_n^1(r_0) e^{2\pi i(E_n^0 - E_n^1)t}. \quad (4.17)$$

All quantities entering the sum on the right hand side are available from the experiment, the eigenenergies from the resonance positions, and the eigenfunctions at the antenna position from the resonance depths [Kuh00].

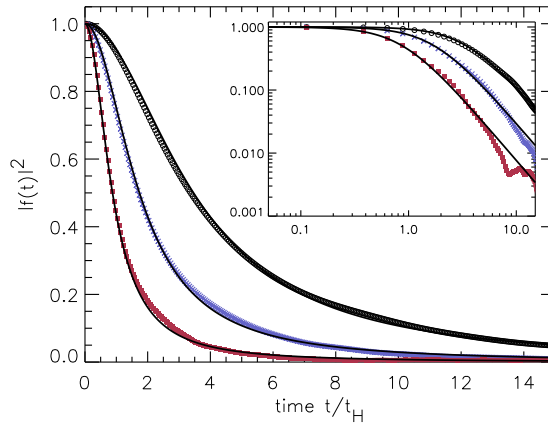


Figure 4.3.: Ordinary fidelity determined as obtained from the resonance position and depths, see text. The meaning of the symbols is the same as in Fig. 4.2.

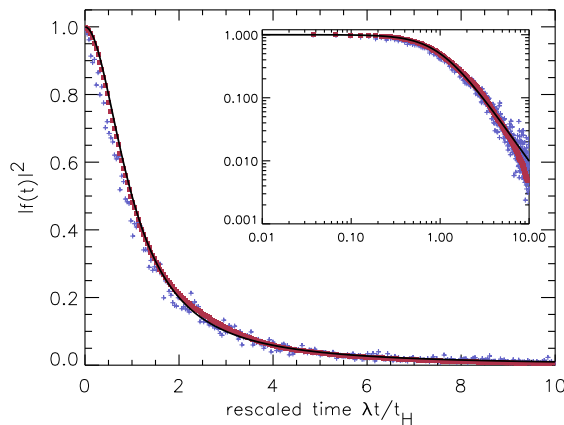


Figure 4.4.: Scattering fidelity, obtained from a superposition of the results from all perturber shifts (blue crosses) and ordinary fidelity (red squares) on a rescaled time axis. The solid line corresponds to the theoretical prediction.

How to obtain this quantity was outlined in the introduction of this chapter. We have computed the fidelity using altogether 64 resonances in the sum of eq. 4.17. In figure 4.3 the results for the fidelity are presented. A very good agreement between theory and experiment is found. Here the relative deviation for the coupling parameter  $\alpha$  taken from the variance of the level velocities and the one obtained from the fidelity even agree up to 1%. No smoothing has been applied. The ordinary fidelity, too, shows the scaling behavior predicted by eq. (4.14) as is shown in figure 4.4. In addition, the collected results for the scattering fidelity, obtained by an averaging over all perturber shifts, is plotted, showing the quality of the agreement between both types of fidelity.



# 5. Rogue waves

## 5.1. General Introduction

In the last few years there was a growing interest in the phenomena called rogue waves, freak waves or giant waves. Rogue waves are waves with a much higher amplitude as one would expect for waves in the actual sea state. One has seen rogue waves for different states such as in a stormy sea but also for a calm sea. For long times the reports of sailors about giant waves has been seen as tall tales. In the last few years there have been some progress of recording such events on the sea. One of the most famous events is the “New year wave” recorded by an oil platform in the North Sea [Hav00]. There are several events described in scientific literature where a rogue wave has hit cargo ships or ferries. A collection of these events can be found in Ref. [Law01]. To investigate the appearance of rogue waves in more detail the European Union has started the MaxWave project [Dan03]. Within this project a satellite has recorded wave heights of the open sea. The data of this project gives a strong hint that one underestimates the freak wave probability with a random wave model. For more details on rogue waves see for instance the review [Kha03].

A first insight for the estimation for the probability of the occurrence of wave heights gives the random sea model of Longuet-Higgins [Lon52]. It is a model of a random superposition of waves but to account for the nonlinearities for water waves one uses a random waves with different wavelengths and directions. For a narrow frequency spectrum one obtains the Rayleigh distribution

$$P(H) = e^{-H^2/2\sigma^2}. \quad (5.1)$$

This distribution describes the probability for the crest height of a wave to exceed the height  $H$ , where sigma accounts for the actual sea state and describes the standard deviation of the height distribution. A freak wave is defined a  $H > 4.4\sigma$ . Estimating with the Rayleigh distribution the probability to find a freak wave, we get a probability of  $6.3 \cdot 10^{-5}$  to observe such a large wave. If we look for the probability of an extreme freak event ( $H \geq 6\sigma$ ) the probability falls to  $1.5 \cdot 10^{-8}$ . However, the data collected by the MaxWave project [Dan03] suggests that the Rayleigh model underestimates significantly the probabilities for the occurrence of freak waves.

There are a number of models using nonlinear instability effects [Ono01, Tru96, Kha03] which successfully describe the mechanism of freak wave formation. However, these nonlinear effects become more efficient if already unusually high wave amplitudes are present as an input. It has been argued in Ref. [Hel08] that the formation of caustics

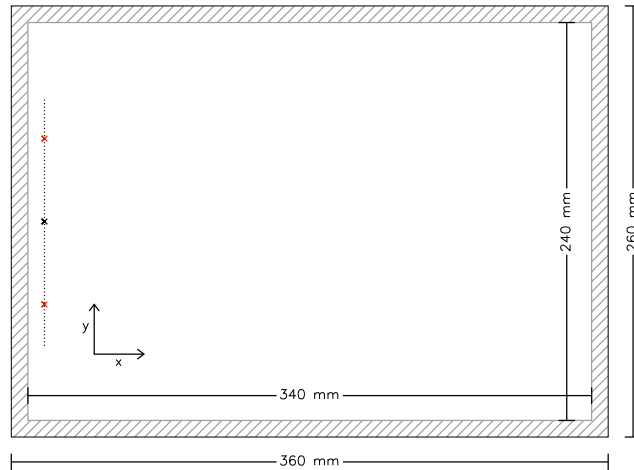


Figure 5.1.: Sketch of the ground plate which we have used for the measurement. The basic size is  $360\text{ mm} \times 260\text{ mm}$ . We can access with our equipment only a subfield of  $340\text{ mm} \times 240\text{ mm}$ . The fixed antenna is situated in the left part of the billiard. Possible positions are indicated by the dotted line.

due to inhomogeneous velocity fields, produced by eddies of varying size, might act as a trigger for these non-linear instability effects.

Such caustics have been also seen in the experiments on branched flow of electrons in a two-dimensional electron gas [Top00, Top01]. This was the starting point for us to try to mimic such a situation and to reinterpretate our results in terms of rogue waves of the sea.

In the following we present first our experimental setup. Afterwards we show some test measurements where we characterize the scattering at a single and at two scatterers. In the second part we present the stationary results for two different configurations of potential landscapes. Here we see the first fingerprint of focussing effects and the formation of caustics. In the last part we shall extend our study to transient waves and we shall present a freak wave event for microwaves in a potential landscape

## 5.2. Basic properties of the experiment

### 5.2.1. Setup

The measurement technique was already introduced in chapter 2. Here we will focus only on the relevant aspects concerning this special setup. In all measurements the distance of the top plate to the ground plate is  $20\text{ mm}$ . The ground plate has a basic size of  $360\text{ mm} \times 260\text{ mm}$ . With our measurement table we can access a sub field of  $340\text{ mm} \times 240\text{ mm}$ . In figure 5.1 is a sketch of the ground plate which indicates dimensions and the accessible field. The fixed antenna is situated in the left part of the ground plate. We have used for different measurements different positions for the fixed antenna.

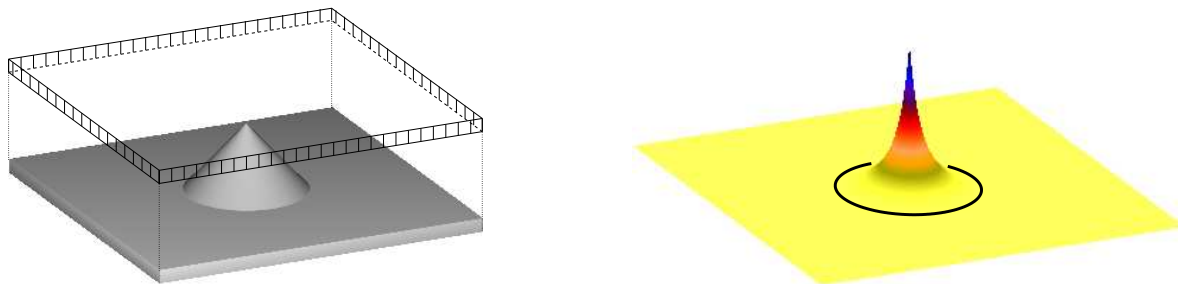


Figure 5.2.: Sketch of one scatterer (a) used in the experiment and the corresponding potential(b). The scatterers have a cone profile with height  $H = 15$  mm and radius  $R = 12.5$  mm. The distance between top and bottom plate is  $h_0 = 20$  mm. In part (b) the strength of the potential is indicated by the height and the color code, where yellow represents small values and blue high values of the potential. The black curve is indicating the boundary of the scatterer.

Common to all these cases is that the antenna is 20 mm away from the left border of the ground plate. This is indicated by the dotted line in the right part of figure 5.1. For the different setups and measurements we made slightly changes from the basic setup. The details of each individual setup are described in the proper context.

We have seen in chapter 2 that it is possible to simulate soft potential by means of a microwave experiments [Kim05a]. In fabricating a potential landscape which comply the one used in the Topinka measurements [Top00, Top01] we have to make a compromise. In principle there are a lot of possibilities to mimic such a potential landscape. According to equation 2.11 we have to vary the height of the cavity. In one possible realization we would have to drill such a landscape into our ground plate of the cavity. This would have been possible, but only with a considerable workshop effort, and with complete lost of flexibility and the arrangement of the scatterers. Therefore we have decided to use a cone like obstacle to be placed on the ground plate. They can be moved freely but with the restriction to be non-overlapping. Thereby we can easily change the configuration of the setup.

Now the question arises what type of potential we get from cones which are pointing into the cavity. Inside the region of such an obstacle we decrease the distance between the top and bottom plate with respect to some basic height  $h_0$  of the resonator. This results in a repulsive potential. The easiest shape of such scatterers is a cone, which we have used in our experiment. In figure 5.2 we illustrate the situation in the cavity for one single scatterer. If we use eq. 2.11 we can specify this expression for the potential in the scattering region:

$$V(|\vec{r}|) = \frac{(\pi n)^2}{\left(h_{\min} + \frac{H}{D/2}|\vec{r}|\right)^2} \quad (5.2)$$

Here  $|\vec{r}|$  is the distance from the scatterer center,  $D$  is the diameter,  $H$  the height of the

scatterer and  $h_{\min}$  the minimal distance between the top plate and the scatterer, thus  $H + h_{\min} = h_0$ .

In the following sections we shall discuss the consequences of this description. We will see that we violate the assumption of an adiabatic change of the potential in comparison with the wavelength. Nevertheless we will use this experimental approach. To estimate the effects for the  $TM_0$  mode we perform some test measurements with a single cone and with two cones. In addition we perform some semiclassical simulations which we will describe next.

### 5.2.2. Simulations with rays – semiclassical description

Even though the wave length in our experiment is comparable with the size of the scatterer we want to compare our results to ray dynamic simulations. In the limit of an adiabatic change of the potential compared to the wave length the  $TM_0$ -mode of the electrical field should not be affected by the potential term but all other modes will be influenced by the scatterers according to eq. 5.2. Classically we can think of a particle which moves in a potential landscape according to the following Hamiltonian:

$$H = \vec{p}^2 + \left( \frac{n\pi}{d(\vec{q})} \right)^2 \quad (5.3)$$

$$\dot{\vec{p}} = -\frac{\partial H}{\partial \vec{q}} \quad (5.4)$$

$$\dot{\vec{q}} = \frac{\partial H}{\partial \vec{p}} \quad (5.5)$$

This Hamiltonian is directly constructed from equation 2.6 which means that we measure the Energy in units of  $1/\text{m}^2$ . The equation of motion for this problem we know from classical mechanics. To calculate the trajectories explicitly we use a the fourth order Runge-Kutta algorithm with adaptable time steps. This algorithm is described for instance in Numerical Recipes [Pre89].

To obtain a density of trajectories we calculate some thousands of them for a given frequency or kinetic energy respectively and count their occurrence for each point on a fictitious measurement grid. The next improvement of this procedure is to calculate the density according to the semiclassical description. The semiclassical wave function or density for a single trajectory can be written as:

$$\psi_{\text{sc}}(\vec{r}) = \frac{c}{\sqrt{p}} e^{iS} \quad (5.6)$$

where  $S = \int p dq + \nu \frac{\pi}{2}$  is the action of the particle along the trajectory. In our simulations we additionally take care for turning points of the simulated particle which gives rise to a Maslovindex of  $\frac{\pi}{2}$ .

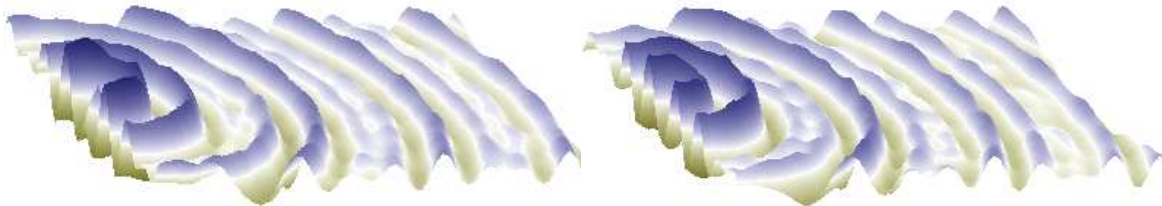


Figure 5.3.: Real (left) and imaginary (right) part of the measured transmission of an empty cavity from one fixed antenna placed in the center of the smaller side of the cavity. Neglecting effects from the boundary the transmission pattern can be described according to eq. 5.7

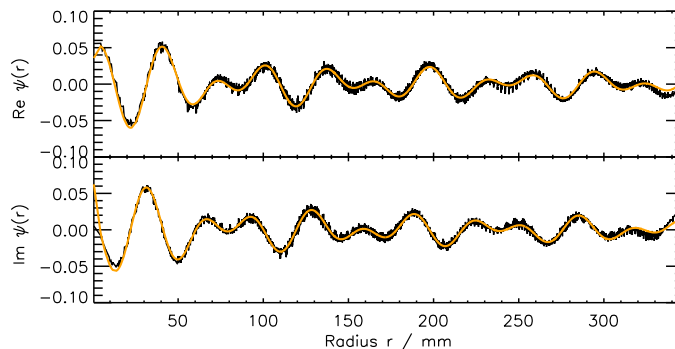


Figure 5.4.: Real (upper) and imaginary (lower) part of the angle averaged transmission versus the distance from the antenna. The solid line corresponds to a fit of equation 5.7.

### 5.2.3. Free wave propagation

In the following we investigate the principle scattering properties of the cones which we have used in our experiment. For a better understanding of the results obtained from the measurement with only a few number of scatterers we have to analyze first a measurement of the empty cavity where the waves can propagate freely. We have measured the free wave propagation in a frequency range from about 7.5 GHz to 15 GHz. In this frequency range only the two lowest TM-modes ( $TM_0$  and  $TM_1$ ) of the electrical field can propagate in the cavity.

The goal of this measurement is to extract the coupling strengths of the zeroth and first TM-modes for each frequency and use this information later to describe the characteristics of the scattering at one or two cones. Theoretically we expect to measure for each mode a Hankel function with the singularity at the source antenna. Assuming that the reflection at the end of the open cavity is small we can write for the wave function inside the cavity:

$$\psi(r, \phi) = a_0 H_0(k_0 r) + a_1 H_1(k_1 r) \quad (5.7)$$

where  $k_0$  is the wave number for the zeroth mode,  $k_1$  for the first mode. The coupling constants  $a_0$  and  $a_1$  are complex numbers which are frequency dependent. They describe the coupling of each mode to the billiard.

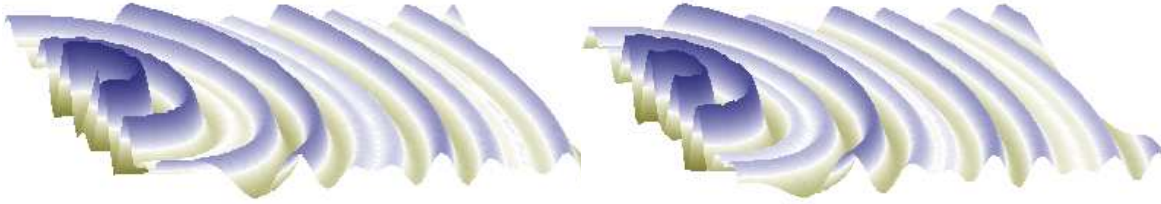


Figure 5.5.: Reconstructed real and imaginary part of the transmission pattern. To obtain the free parameters  $a_0$  and  $a_1$  a fit to the experimental data using eq. 5.7 was performed.



Figure 5.6.: Remaining data if we subtract from the measured data (Fig. 5.3) the the fitted Hankel functions from Fig. 5.3. We have used the same scaling of the  $z$ -axis as in figure 5.5.

In figure 5.3 we show the real and imaginary part of the measured wave function. The figure is shown for a frequency  $\nu$  of 10.5 GHz. To show how good the data is described by the sum of two Hankel functions we can present the data in dependence of the distance from the fixed antenna. This is done in figure 5.4. In this figure the real (upper) and imaginary (lower) part of the transmission for each point versus the distance from the fixed antenna is presented. The solid line corresponds to a fit of the experimental data with equation 5.7. We see a very good agreement between the experimental data and the fit. In figure 5.5 we present the theoretical wave function reconstructed from the fitting parameters. If we compare this with the figure of the experimental data we see small deviations. The deviations are due to the reflection of the waves at the open ends of the cavity. We can obtain this background easily by subtracting the theoretical from the experimental wave function. This background is shown in figure 5.6.

The fit of the experimental data with the function of equation 5.4 can be performed for each measured frequency. Thus we can extract the coupling strength of the antennas to the two modes in dependence of the frequency. In figure 5.7 the black curve describes the absolute value of the coupling for the zeroth mode and the blue line for the first mode. From this figure we see that the coupling of the first mode is zero at the beginning but is increasing with increasing frequency. The two couplings later behave similarly. From the fact that the sum of the coupling strengths is much less than 1 we see that major parts of the measuring signal are not entering the cavity.

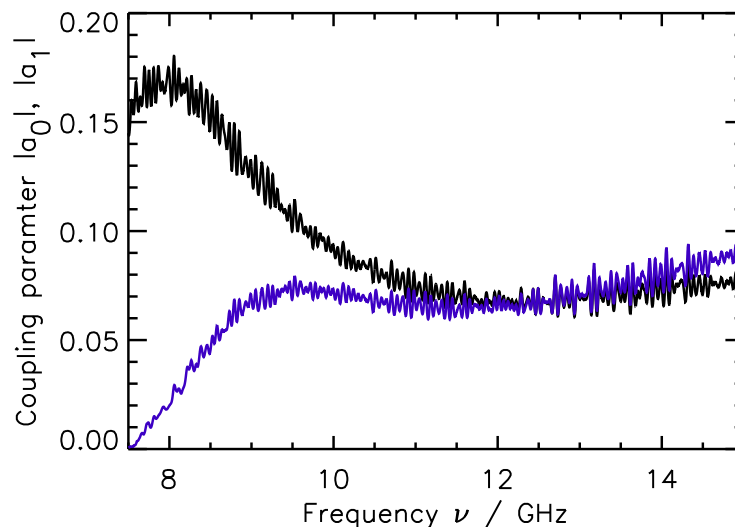


Figure 5.7.: This figure shows the absolute values of the coupling parameters  $a_0$  and  $a_1$  versus the frequency. The black line corresponds to the zeroth mode ( $a_0$ ) the blue line to the first mode ( $a_1$ ).

### 5.2.4. One and two scatterers

#### General description

We can now investigate the scattering properties of the cones. We therefore have performed measurements with a single cone and with two cones in the cavity. To analyze the scattering properties of the cones we will present the measured wave function and compare this with numerical or theoretical data. It turned out that we are in the limit of strong or  $s$ -wave scattering. This implies also that the scattering function can be described approximately by a Hankel function. In a first approximation where we neglect multiple scattering we can write for the wave function inside the cavity.

$$\psi(\vec{r}) = \psi_{\text{in}}(\vec{r}) + \sum_{i=1}^N a_0^i [H_0(k_0|\vec{r} - \vec{r}_i^z|) + a_1^i H_0(k_1|\vec{r} - \vec{r}_i^z|)]. \quad (5.8)$$

In this equation we have used that the origin is situated at the fixed antenna. The incoming wave is denoted by  $\psi_{\text{in}}(\vec{r})$  which is described by equation 5.7. For each scatterer we have to add an additional Hankel function which has for each mode the coefficients  $a_0^i$  and  $a_1^i$ .

#### One scatterer

In figure 5.8 in the left part we show the absolute value of the measured transmission pattern where we have a single cone 72.5 mm in front of the fixed antenna. We have

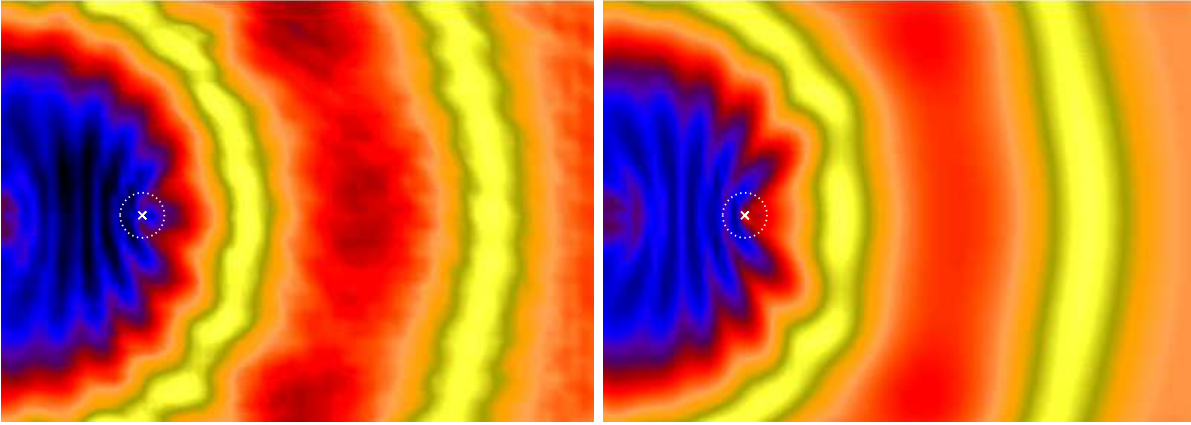


Figure 5.8.: Absolute value of the transmission pattern with a single cone as a scatterer for a frequency of 14 GHz. The center of the cone is indicated by a cross and the circumference of the scatterer by a dotted circle. In the left part the measurement is presented where we have subtracted the background which had remained in the free propagation measurement. The right part shows the reconstructed wave function according to eq. 5.8.

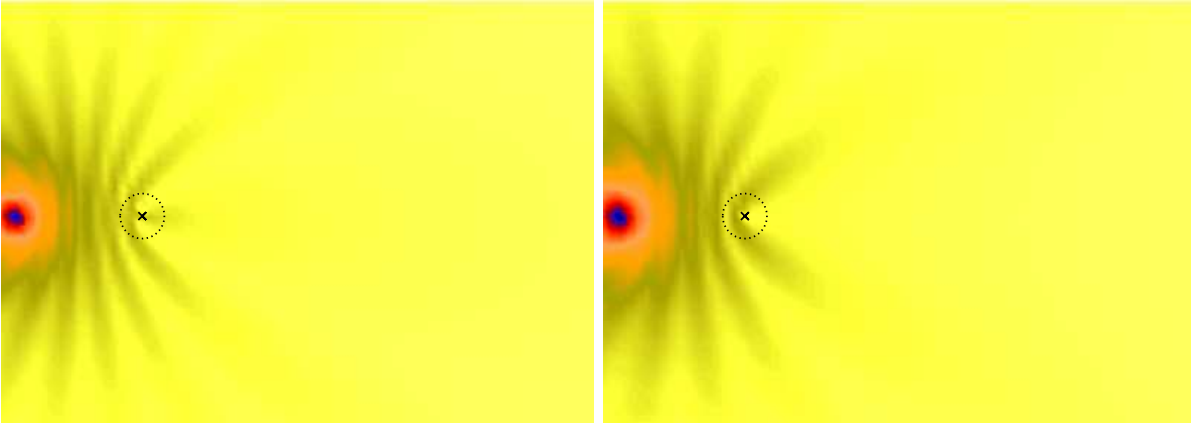


Figure 5.9.: Absolute value of the reconstructed wave function for each single mode. The left part of the figure presents the wave function of the  $TM_0$  mode. The right part for the  $TM_1$  mode.

measured this wave function at a frequency  $\nu = 14.0$  GHz. To improve the quality of the figure we have removed the background which had remained in the measurement of the empty cavity when we have subtracted the fitted Hankel functions from the experimental data (see fig. 5.6).

The right part of figure 5.8 shows the reconstructed wave function according to equation 5.8. The parameters of the incident waves we have already determined independently from the measurement of the empty cavity. Thus we have just to obtain the parameters  $a_0^1$  and  $a_1^1$  of the scattering function. This procedure assumes that the back scattering of the waves from the cone does not change the coupling strength of the antenna. We see a very good agreement between the experimental wave function and the reconstructed one.

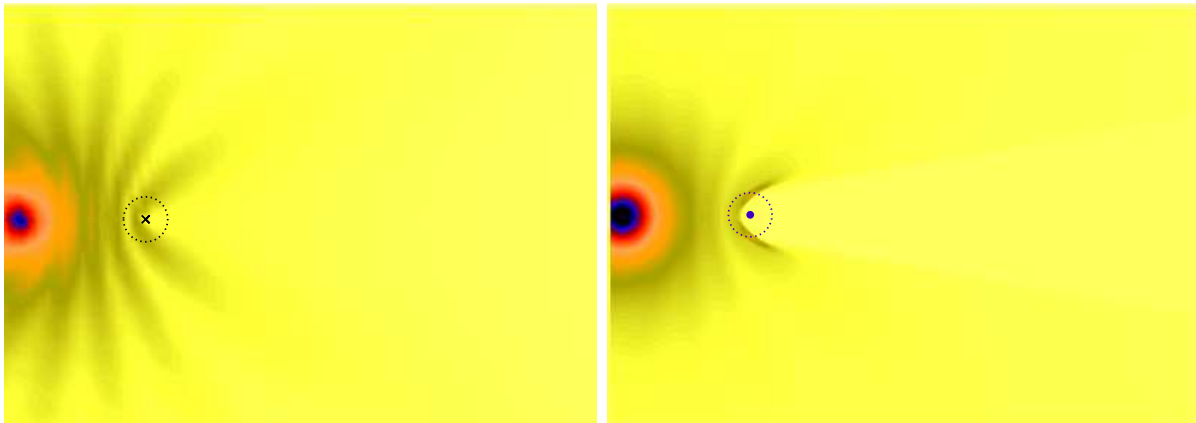


Figure 5.10.: Here we present a comparison between reconstructed wave function of the first mode (left) and the semiclassical simulation (right) for the same frequency as in fig. 5.8

From the last paragraph we know that the experiment can be described very well using the superposition of Hankel functions from equation 5.8. Thereby we have the possibility to investigate each mode separately. In figure 5.9 we present the absolute value of the wave function for each mode independently. Here we see that not only the first mode is affected by the potential but also the zeroth mode feels the potential quite strongly.

Even though we are in the limit of  $s$ -wave scattering we have performed a numerical simulation of the scattering of a classical particle at the cone for the first mode. For the calculation we have started  $10^5$  trajectories from the source antenna with equally distributed leaving angle. To obtain the wave function we have calculated the density of the trajectories, where the amplitude of each trajectory was obtained according to equation 5.6. The result is shown in the right part of figure 5.10. In the left part we have repeated for a better comparison the wave function of the first mode. If we compare these two figures we can see that we have in the semiclassical simulation a shadowing effect which is not present in the wave case. But some of the structures in the vicinity of the cone are reproduced qualitatively by the semiclassical simulation.

## Two scatterers

We have performed the same measurement and analysis for the two cone case. The idea of this measurement was to see a kind of focus effect in the center behind the two cones due to the scattering of the incident wave by the two repulsive potentials. The results are presented in the figures 5.11, 5.12 and 5.13 for a frequency of 14 GHz. Again we show first the experimental scattering wave function and compare it with the fit of a sum of Hankel functions. Again we see a good agreement between the measured wave function and the reconstructed wave function of the fit. Additionally we can compare the scattering coefficients for each of the two modes for the two scatterers with those for a single scatterer. To obtain the coefficients in the two scatterer case we have used the symmetry of the problem such that we have fitted the two cones with identical parameters for each mode. For the  $TM_0$  mode we obtain for the single

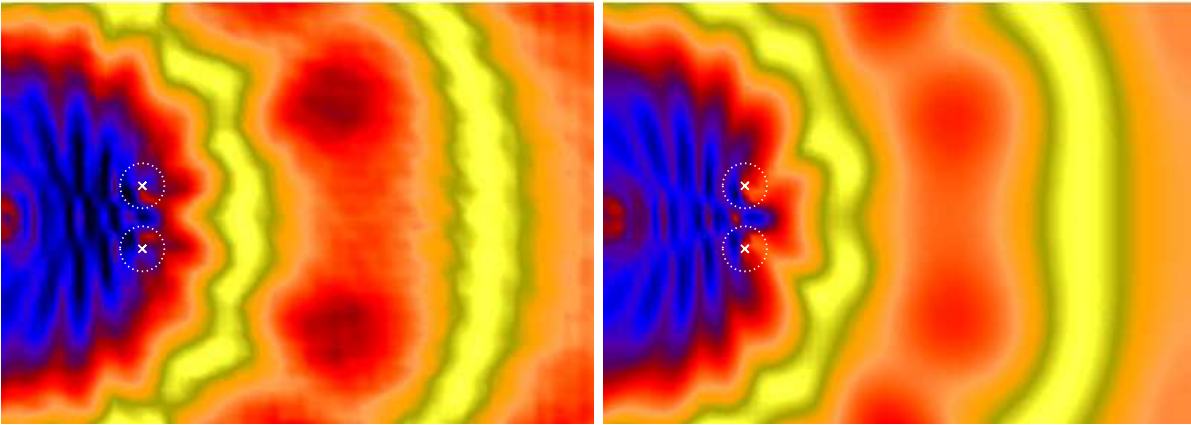


Figure 5.11.: Absolute value of the wave function with two scatterers. The center of the cone is indicated by a cross and the circumference of the scatterer by a dotted circle.

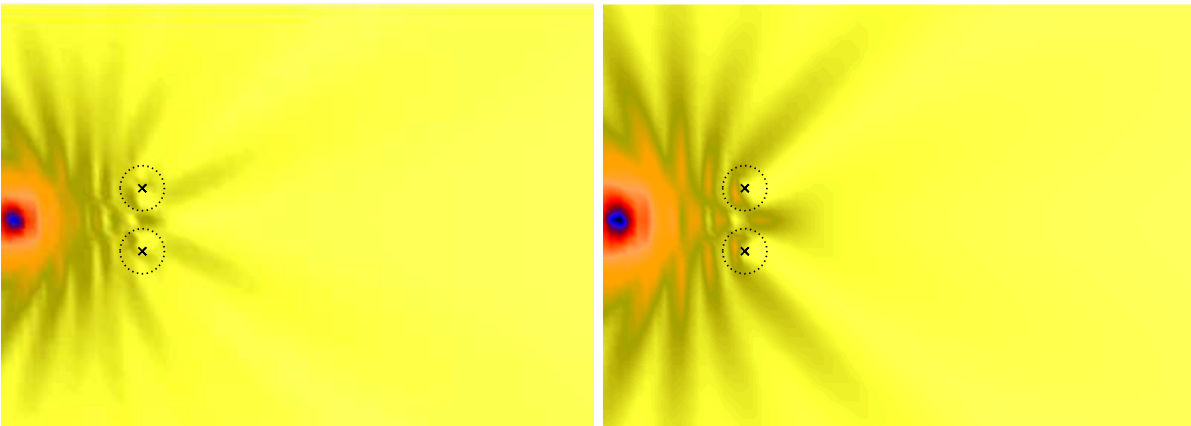


Figure 5.12.: Absolute value of the reconstructed wave function for each single mode. The left part of the figure presents the wave function of the  $TM_0$  mode. The right part for the  $TM_1$  mode.

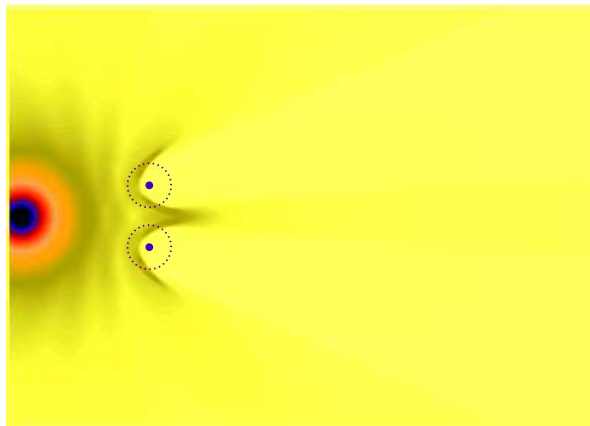


Figure 5.13.: Semiclassical simulation for the first mode of the two cone experiment.

scattering a absolute value for the coefficient of  $8.13 \cdot 10^{-3}$  compared to  $8.12 \cdot 10^{-3}$  in the two scatterer case. For the  $TM_1$  mode the situation slightly changes. Here we get a

absolute value of the coefficient for the single scatterer case of  $8.11 \cdot 10^{-3}$  compared to  $6.83 \cdot 10^{-3}$ , which is a relative deviation of about 15%. This indicates that for the  $TM_1$  mode we have already to consider multiple scattering effects to describe this problem correctly.

As in the single scatterer case we show also the wave functions for each individual mode. And finally we present the results of the first mode of our numerical ray simulation. Apart from the shadowing effect in the classical picture we see again a reasonable agreement between the wave treatment and the semiclassical description. We also can perceive a kind of focus effect behind the two scatterers for the first mode.

We have seen in the last section that also the  $TM_0$  mode is affected by the cones quite strongly. But nevertheless this does not mean that our experimental approach must fail. Experimentally the situation has not changed dramatically by this effect. With the scattering of the  $TM_0$  mode we measure already a superposition of two independently scattered waves for the  $TM_1$  mode case. Concerning the ray simulations we can conclude from the test measurements that the scattering of the  $TM_1$  mode is reproduced at least qualitatively by the simulation. This implies that we can hope at least for high frequencies, where the  $TM_0$  mode is one mode under many open modes, a reasonable good agreement between simulations and experiments. Thus we just proceed with the analysis of the experiment and turn now to the description of the multiple scatterer arrangement.

### 5.3. Scatterer Configurations

Within our measurement field of  $240\text{mm} \times 340\text{mm}$  we place the cones randomly but non-overlapping. In figure 5.14 we have sketched the first realization of the scatterer arrangement. The fixed antenna is situated in the center of the y-direction (this is the smaller side) and is 20 mm away from the border of the cavity. The position of the antenna is marked by a cross.

In figure 5.15 we show the second realization of our experiment. One change to the previous setup of course is the different position of the cones. The second change is the possibility to measure at three different positions with the fixed antenna. The second and third antenna are placed 50 mm away from the center and again 10 mm away from the border. The three positions are marked with crosses in the sketch of the setup. To obtain for all three measurements the same conditions we have attached to the non active antennas a  $50 \Omega$  load, simulating a measurement device attached to this antenna.

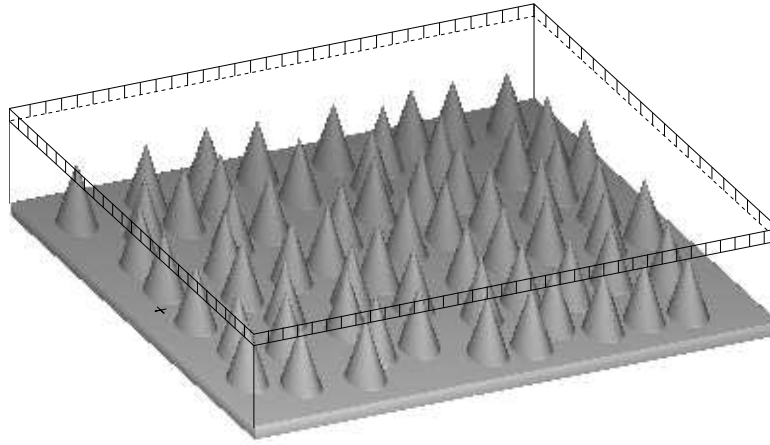


Figure 5.14.: Sketch of the setup. The arrangement of the scatterers shows the first realization. The cross on the left side indicates the position of the fixed antenna.

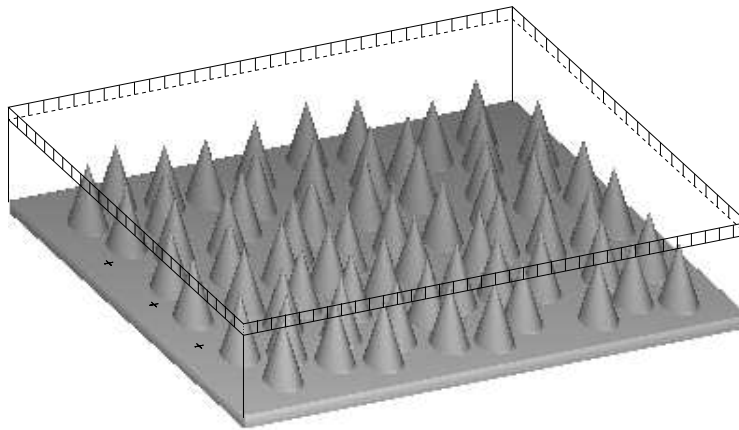


Figure 5.15.: Sketch of the setup. The arrangement of the scatterers shows the second realization. The three crosses on the left side are indicating the three possible fixed antenna positions.

## 5.4. Results in energy domain

### 5.4.1. Wave functions

In the left part of figure 5.16 we show the intensity of a measured wave function for the first configuration of the scatterer arrangement. The presented wave function is measured at a frequency of 30.95 GHz. For this frequency in total 6 modes can propagate in the cavity. We already can see in this figure a branching of the wave function. We have also performed a semiclassical simulation for the modes one to five. The result of this simulation is shown in figure 5.16 in the right part. In the simulation we can see a clustering or guiding of the major part of the rays. These clustered parts coincides in some cases with high amplitudes of the measured wave function.

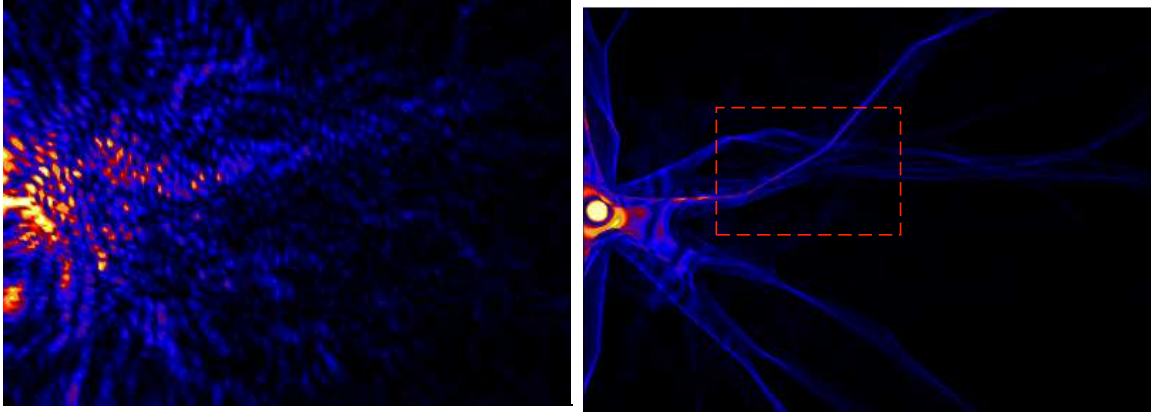


Figure 5.16.: (Left): Wave function for the frequency  $\nu = 30.95$  GHz. (Right): Corresponding semiclassical simulation, where the modes 1 to 5 have been considered.

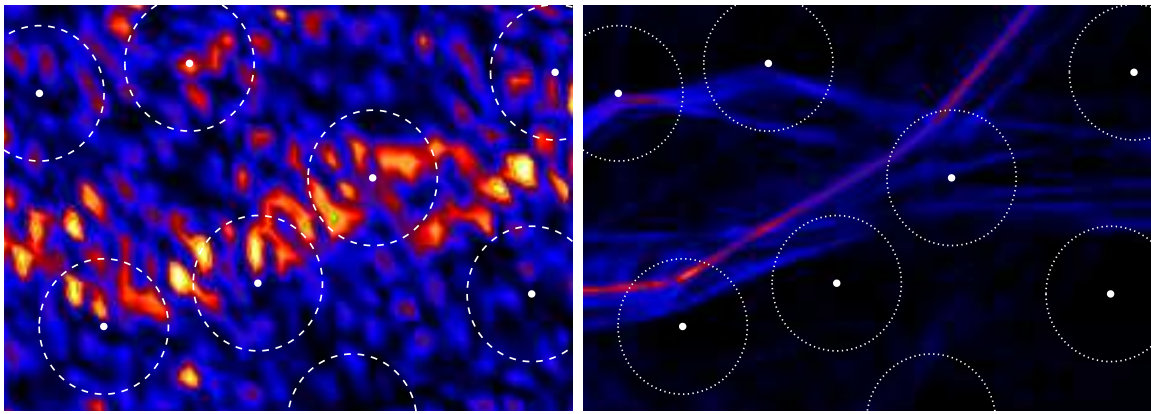


Figure 5.17.: Details of Fig. 5.16. Both for the experiment and the simulation the branches do not follow the potential valleys, but concentrate on the slopes, showing that the branch structures are caused by caustics.

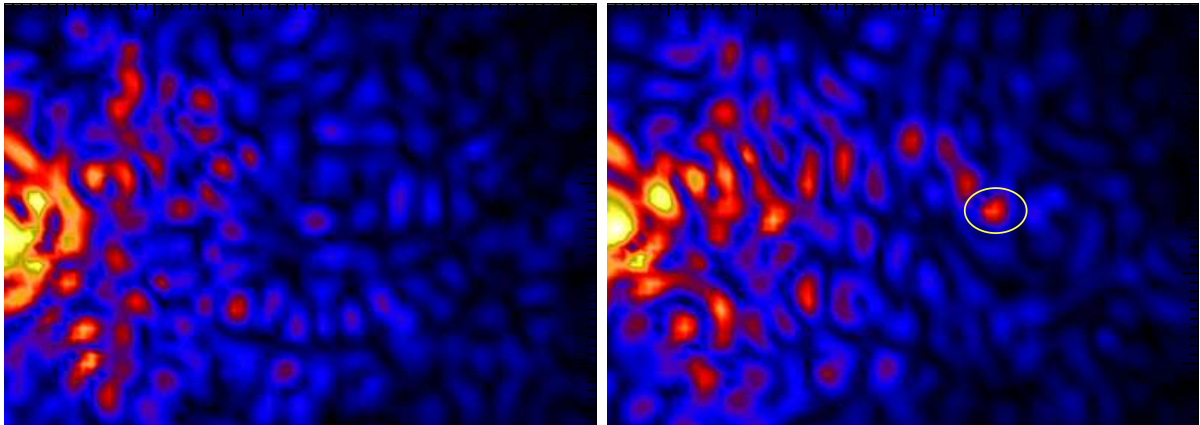


Figure 5.18.: Two wave functions measured at the frequencies 10.03 GHz (left) and 9.53 GHz (right) of the second scatterer configuration. In the right figure we have indicated a spot with a high amplitude by a yellow ellipse.

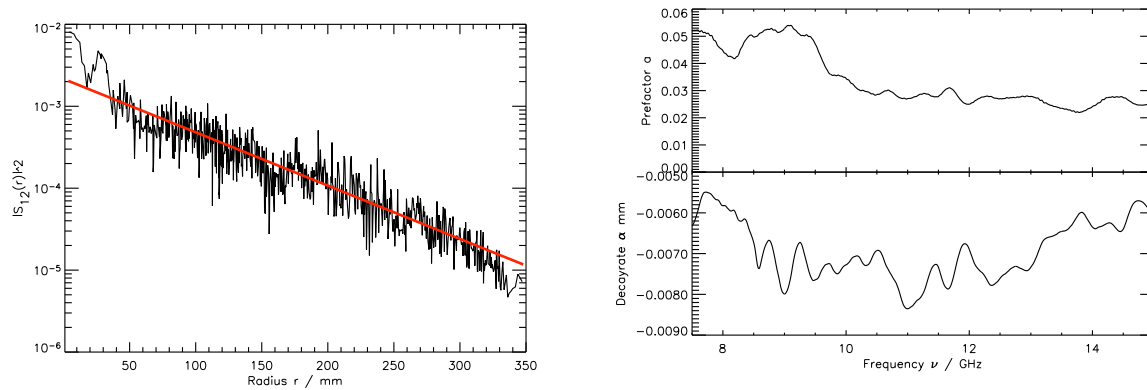


Figure 5.19.: In the left part we plot the intensity of the wave function versus the distance from the source antenna. The  $y$ -axis is plotted on a semi logarithmical scale. The solid line is an exponential fit of the data. In the right part of the figure the fitting parameters are shown in dependence of the frequency. In the upper plot the pre-factor  $a$  of the exponential function and in the lower plot the decay constant  $\alpha$  is presented.

In [Kap02] such branches, which had first been seen in the branched flow experiments of Topinka et. al. [Top00], have been analyzed in more detail. It was pointed out that these branches are caustics in the semiclassical description which do not follow the valleys and also do not avoid high values of the potential. In figure 5.17, which is a blowup of figure 5.16, we see that also in our experiment the branches concentrate on the slopes of the potential and not in the valleys. This is a clear fingerprint of caustics in our experiment.

We present two more typical wave functions which we have obtained in our experiment with the second configuration. They are shown in the left and right part of figure 5.18. In all measured wave function shown up to now we have seen a radial decline of the wave function. This decline will be discussed in the next section separately. In the right part of the second figure we see apart from this decline for a small region a quite high amplitude compared to the amplitudes in the neighborhood. The spot with the high amplitude is marked with a yellow ellipse. After having removed the decay we will see that these points will play a major role for the evolution of extreme high intensities of transient waves and they are the main focus of our study.

### 5.4.2. Radial decline

In this section we quantify the radial decline which we have seen before in the figures of the wave functions. To analyze the radial dependence we plot the absolute value of the wave function versus the distance from the antenna. This is presented in the left part of figure 5.19 in a semi logarithmic plot of the data. For this plot we have superimposed 50 wave functions in a frequency range from 9.475 GHz to 9.525 GHz. For the presentation we have applied an additional smoothing, but not for the data processing. We find from this figure that the decline is an exponential decay. The solid red line in the figure is

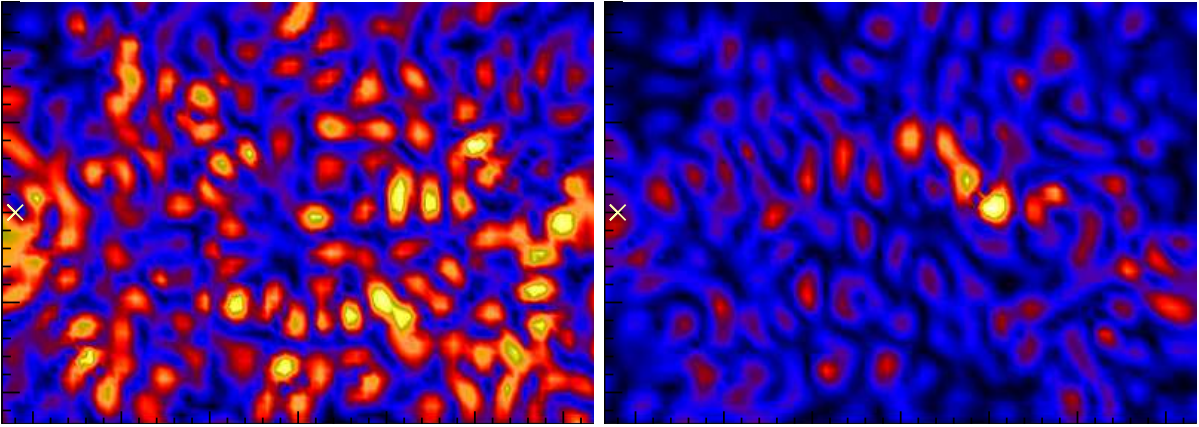


Figure 5.20.: The same wave functions as in figure 5.18 but we have removed the decay. Here we have marked the position of the fixed antenna with a cross

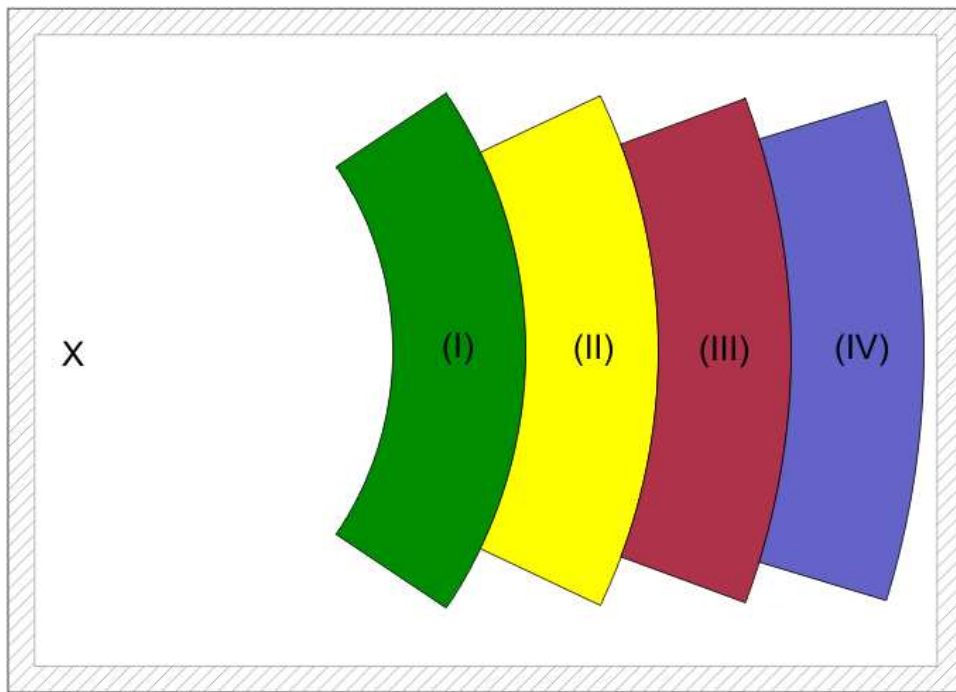


Figure 5.21.: This figure shows the data segmentation which we use for later data analysis. The cross in the left part of the billiard indicates the position of the source antenna.

a fit of an exponential with a pre-factor  $a$  and a decay constant  $\alpha$ . For each frequency we can apply this fit where we again average over a frequency window of 50 MHz. The resulting pre-factor  $a$  and the decay constant  $\alpha$  are plotted versus the frequency in the right part of figure 5.19.

In figure 5.20 we show the same two wave functions as in figure 5.18 but with the decay removed. In the left part of the figure the wave function now has an equally distributed amplitude whereas the wave function in the right part of the figure shows a strong spot.

Here the amplitude is much higher than the amplitudes of the remaining part of the billiard.

### 5.4.3. Intensity distributions

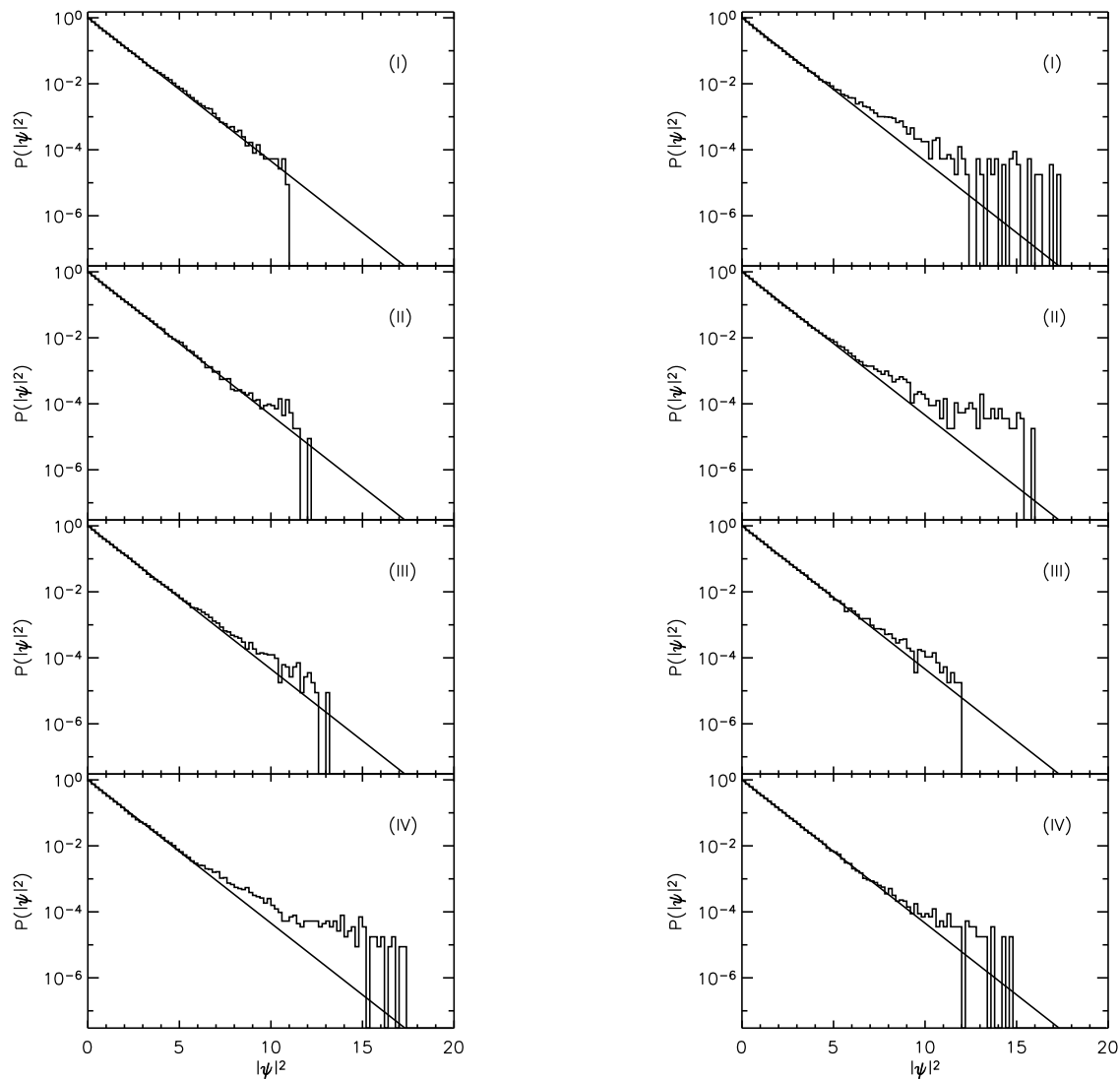


Figure 5.22.: Intensity distributions for each of the segments shown in figure 5.21. The left part of the figure shows the distributions of the first scatterer configuration. The right part the data for the second configuration

We have discussed in the last section that we see in our experiment an intrinsic decay. We will remove this decay for all the following data analyzing steps. By this procedure we have uncovered for some wave functions a very high amplitude in a small confined region. We now want to turn to the question whether these points which have such a high amplitude have a noticeable effect on the intensity distribution. For a fully open

and chaotic billiard the intensity distribution is known to be an exponential decay:

$$P(I) = \frac{1}{\langle I \rangle} e^{-\frac{I}{\langle I \rangle}} \quad (5.9)$$

where  $\langle I \rangle$  is the mean intensity. To analyze the experimental data we have segmented the billiard into four parts. They are shown in figure 5.21 and labeled with (I), (II), (III) and (IV). We have then computed the intensity distribution in the frequency range from 7.5 Ghz to 15 Ghz for each segment individually. The wave function was normalized according to  $\int d\vec{r} \psi^2 = 1$  for every single segment.

We show in figure 5.22 the result for the intensity distribution for both measured configurations. In the left part we present the results for the first configuration in the right part the results for the second. We see that for both setups there are regions, where the intensity distribution follows the prediction (5.9), but there are also regions sharing strong deviations. For the first configuration we see a large deviation from the prediction in segment (IV). For the second configuration we have the largest deviations in segment (II). The major part of this large deviation in segment (II) could be assigned to the wave function we have presented in figure 5.20 (with removed decay).

All following investigations and further measurements have been performed with the second setup as here the spot with the large intensity or amplitude is in the interior of the billiard and not close to its border. We cannot assure that the high amplitude seen in the first configuration might be influenced by the boundary.

We have seen for wave functions regions with large amplitudes and we could show that these amplitudes are more likely to occur in our setup as would have been expected from the random wave model. All the results shown here have been obtained in quasi-stationary measurement. More interesting is the question whether these spots also are relevant for transient waves constructed from wave functions with such high amplitudes. This will be treated in the next section.

## 5.5. Transient waves

### 5.5.1. Setup to measure transient waves

The main goal of our measurement was to perform an analogue experiment with electromagnetic waves for the situation of water waves in the ocean which are effected by a potential landscape (neglecting the fact that water waves have a different dispersion relation and the wave equation is non linear). The picture we have discussed so far was a steady state picture which is not likely to be the situation on the ocean. We have therefore performed with the second configuration a number of additional measurements where the fixed antenna was shifted by a small amount of 2 mm. In total these were 31 different positions. We have recorded the wave function at a smaller sub field which is indicated in figure 5.23 by the red field in a frequency range from 7.5 to 15 GHz. These additional measurements give us the possibility to change the angle under which the

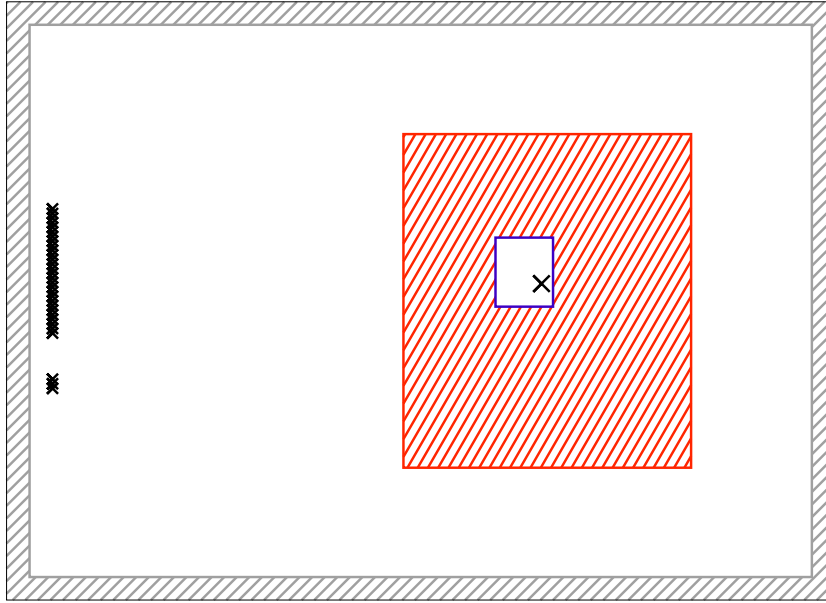


Figure 5.23.: Sketch of the setup for the measurement of transient waves. The red shaded region indicates the sub field of the full billiard where we measure a reduced wave function for different fixed antenna positions. The different antenna positions are marked with crosses in the left part of the billiard. The intersection is due to a cone which we could not pass. The blue region is the neighborhood of the spot which is marked by the large cross.

waves reach the spot point. Furthermore we can superimpose different wave functions from different antenna positions of the fixed antenna. This enables us to mimic transient waves where we will show some results in the later part of this section. In figure 5.23 we show some information about how we have structured the later data analyzing and presentation. We will show later distributions functions or data from three different regions of the subfield we have measured. First we are interested in the point where we have found the large intensity. This point is indicated by a large cross. Secondly we are interested in the neighborhood of this spot. This field we surrounded with a blue box in the figure. That the spot is not in the center of the blue box has the reason that in the left upper part a bit smaller but still very high intensity was found. We wanted both spots to be in this region. The third region of interest is the red field which we call the background or surrounding.

### 5.5.2. Results in the time domain

To turn our stationary patterns presented in the last section into running waves, to be as close as possible to the situation found in the sea, we have to superimpose patterns with different frequencies, entering from different directions,

$$\psi(\vec{r}, t) = \frac{1}{N} \sum_{i=1}^N \psi_{x_i}(\vec{r}, \omega_i) e^{i(\omega_i t - \varphi_i)}. \quad (5.10)$$

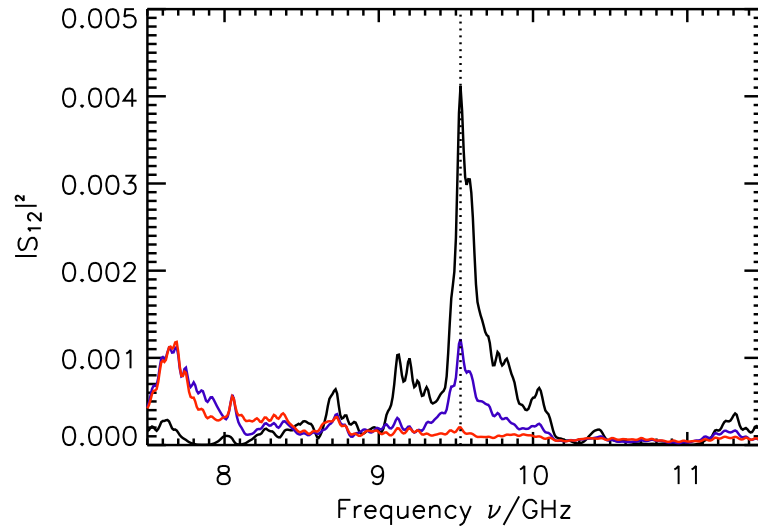


Figure 5.24.: This plot shows the intensity versus the frequency where the source antenna is in the central position. The black curve corresponds to the intensity of the spot, the blue to the neighborhood of the spot and the red to the background. The dotted line indicates the frequency of the maximal intensity.

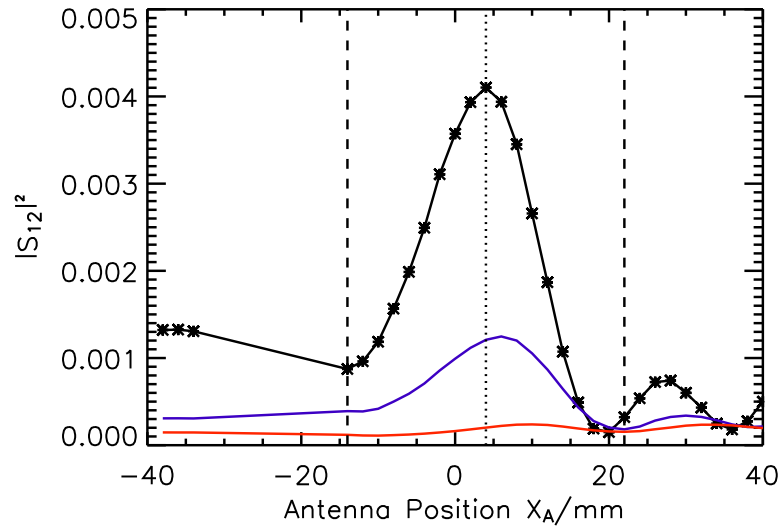


Figure 5.25.: Here we show the intensity versus the position of the source antenna. The color code is the same as in Fig. 5.24. The data is recorded at a frequency  $\nu$  of 9.53 GHz. The dotted line indicates the point of the maximum. The dashed line will be the border for an interval for a selection rule (see in the text)

Here  $\psi_{x_i}(\vec{r}, \omega_i)$  is the wave pattern excited by the antenna at position  $x_i$  and angular frequency  $\omega_i = 2\pi\nu_i$ ,  $\varphi_i$  is a random phase, and  $N$  is the number of patterns superimposed.

To identify the optimal ranges from which we will take the pattern and frequencies

we show the intensity at the spot point in dependence of the frequency in figure 5.24. For this figure we have used the central position of the source antenna. The black line indicates the intensity at the spot. The red line corresponds to the mean intensity of the background. We see a maximum of the intensity for 9.53 GHz for the spot. The intensity of background remains low. Additionally we see a smaller maximum below 8 GHz for the background data. This maximum is due to another small spot which will not be analyzed here.

In figure 5.25 the intensity of the spot is plotted versus the position of the fixed antenna. The frequency for this figure was chosen according to the maximal intensity of figure 5.24. We can see again a maximum which is situated at -4 mm for the position of the source antenna. Again the mean intensity of the background is much lower than the intensity of the spot. The dips in intensity of the spot at positions -20, 20, and 35 mm are a result of shadowing. Here the antenna faces directly a nearby scatterer.

There are obviously a huge number of possibilities to superimpose the stationary patterns. First of all we applied a Gaussian distribution for the selected frequencies  $\nu_i$  centered at 9.5 GHz and a variance of  $\Delta\nu_G = 0.764$  GHz thus covering more or less the frequency window where the spot was found. Within this window the frequencies were chosen at random. According to the uncertainty relation this corresponds to wave trails of length  $\Delta r = c/2\pi\Delta\nu_G = 60$  mm. The phases  $\varphi_i$ , too, were chosen at random, and the antenna positions  $x_i$  were taken from the set of positions within the two dashed vertical lines in Fig. 5.25. For the number of patterns to be superimposed we chose  $N = 150$ .

In calculating the time signal from eq. 5.10 we face a problem. Since in the measurement the frequencies had been increased in fixed steps  $\Delta\nu = 1.0$  MHz, the generated time signals are periodic with a period  $T = 1/\Delta\nu \approx 1000$  ns. Therefore we proceeded in a slightly different way: Instead of looking for the time evolution of  $\psi(\vec{r}, t)$  we looked for the probability density  $p(I)$  of intensities  $|\psi(\vec{r}, 0)|^2$  at time  $t = 0$  by averaging over the phases  $\varphi_i$ . This should be equivalent to the probability density of  $|\psi(\vec{r}, t)|^2$  as a function of time. Additionally we picked up the frequencies within the Gauss window and the used antenna positions at random for an ensemble averaging.

We did investigate the intensity distribution of the whole field for an ensemble of  $10^6$  different pattern generated with the method described above. Thereby we have distinguished in our analysis between three different fields: the complete field, the complete field without the area around the spot and the spot itself (as we have indicated in figure 5.23). The distribution of the intensities of all points is shown in figure 5.26 by the black data points. The black solid line indicates the expected result from a random wave model. We see a strong deviation from this expected behavior of the random wave model. The distribution of the intensities where we have excluded the spot is presented by the blue data points. We see that even if we exclude the spot point we do not reach the exponential decay we would have expected for a purely random field. We have found that if we choose an arbitrary point of the field and look for the distribution of the intensity for this point only, we see the expected exponential decay but with a local mean intensity  $\langle I \rangle_{\text{loc}}$ . The orange data points in figure 5.26 presents the intensity distribution of the spot are therefore one example of this effect. Here the local mean intensity exceeds by far the mean intensity of the full field. We also see that the tail of

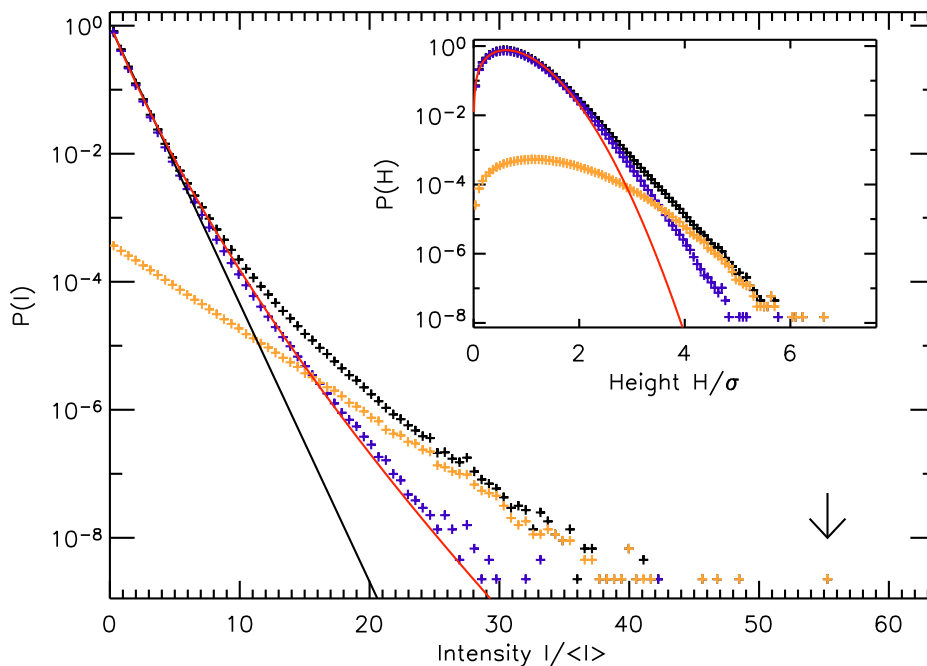


Figure 5.26.: Intensity distribution for the wave patterns generated by means of eq. (5.10), averaged over 1,000,000 realization, for all point of the area displayed in Fig. 5.20 (dark), and for points of the region of the hot spot only (orange). The distribution of all points but a small region around the spot is presented by the blue data points. The black solid line corresponds to the expectation from the random plane wave model. The red solid line has been calculated from eq. (5.14), see the text for details. The arrow indicates the used pattern for the time evolution study presented in Figs. 5.28 and 5.29.

the distribution of all points is dominated by the intensity distribution of the spot. As the local mean intensity  $\langle I \rangle_{\text{loc}}$  can be different for each point, the intensity distribution for all points thus may be written as

$$p(I) = \int dz p_{\text{loc}}(z) \frac{1}{z} e^{I/z}, \quad (5.11)$$

where  $p_{\text{loc}}$  is the probability density to observe a value of  $z$  for the local average  $\langle I \rangle_{\text{loc}}$ . Exactly the same phenomenon has been observed in Ref. [Hel08] in simulations of wave patterns produced by a locally varying velocity field.

We have been able to access  $p_{\text{loc}}$  experimentally. The result is shown in Fig. 5.27. In Ref. [Hel08] a Gaussian distribution had been assumed, but the experimental distribution function shown in Fig. 5.27 definitely is non-Gaussian. Instead it can perfectly be described by a  $\chi^2$ -distribution,

$$p_{\text{loc}}(z) = \left( \frac{n}{2\langle I \rangle} \right)^{\frac{n}{2}} \frac{1}{\Gamma\left(\frac{n}{2}\right)} z^{\frac{n}{2}-1} \exp\left(-\frac{nz}{2\langle I \rangle}\right). \quad (5.12)$$

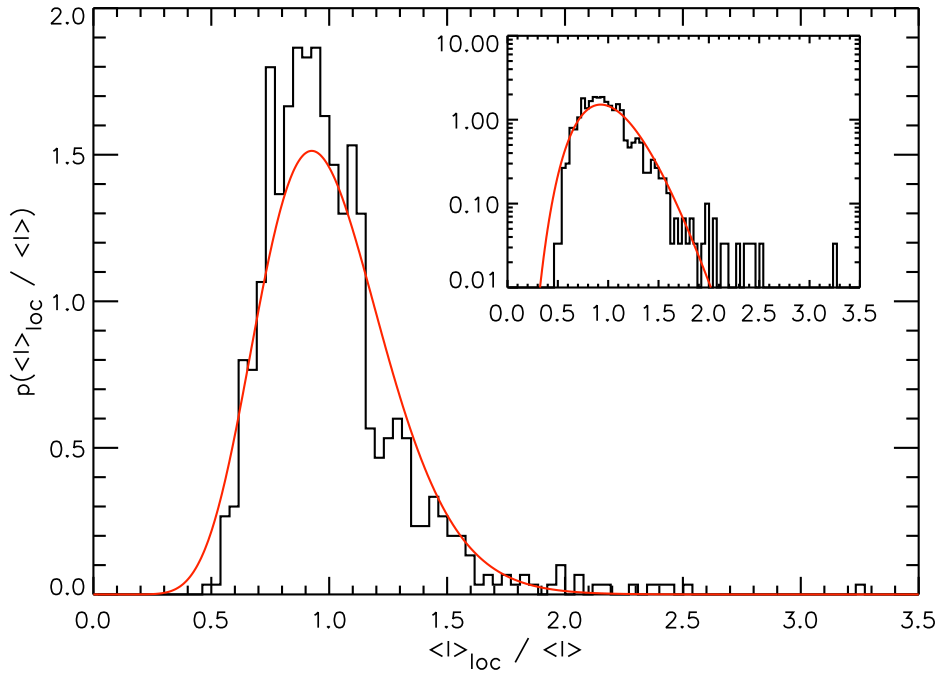


Figure 5.27.: Distribution of the mean intensities found for the 780 pixels of our measurement. The inset shows the same data but in a semi-logarithmical plot. The solid line is a fit with a  $\chi^2$ -distribution with 31 degrees of freedom

with  $n = 31$  degrees of freedom. Note that there is an additional factor  $n$  in the exponent, and a corresponding change in the normalization, missing in the usual definition of the  $\chi^2$  distribution. This rescaling had been necessary to meet the condition

$$\langle z \rangle = \int z p_{\text{loc}}(z) dz = \langle I \rangle, \quad (5.13)$$

With expression (5.12) for  $p_{\text{loc}}(z)$  the integral (5.11) can be solved analytically with the result

$$p(I) = \frac{n}{\langle I \rangle \Gamma\left(\frac{n}{2}\right)} \left(\frac{nI}{2\langle I \rangle}\right)^{\frac{n}{4}-\frac{1}{2}} K_{\frac{n}{2}-1} \left(2\sqrt{\frac{nI}{2\langle I \rangle}}\right), \quad (5.14)$$

where  $K_\nu(x)$  is a modified Bessel function. The red line in Fig. 5.26 has been calculated from eq. (5.14). It fits perfectly with the intensity distribution found if the spot region is excluded, but not with the distribution including the hot spot. This is not really a surprise. Already the inset of Fig. 5.27 shows that the  $\chi^2$  distribution, though generally working very well fails to describe the rare events in the tail of very high amplitudes.

We now turn our attention to the time evolution itself. For the further discussion we picked out one event, marked by an arrow in Fig. 5.26. The experimental probability to find this event had been about  $1.3 \cdot 10^{-9}$ . It may thus be called “rare”, but one should keep in mind that it exceeds the probability expected for a random pattern by a factor of  $10^{15}$ ! Thus in purely random patterns such events in practice never will be

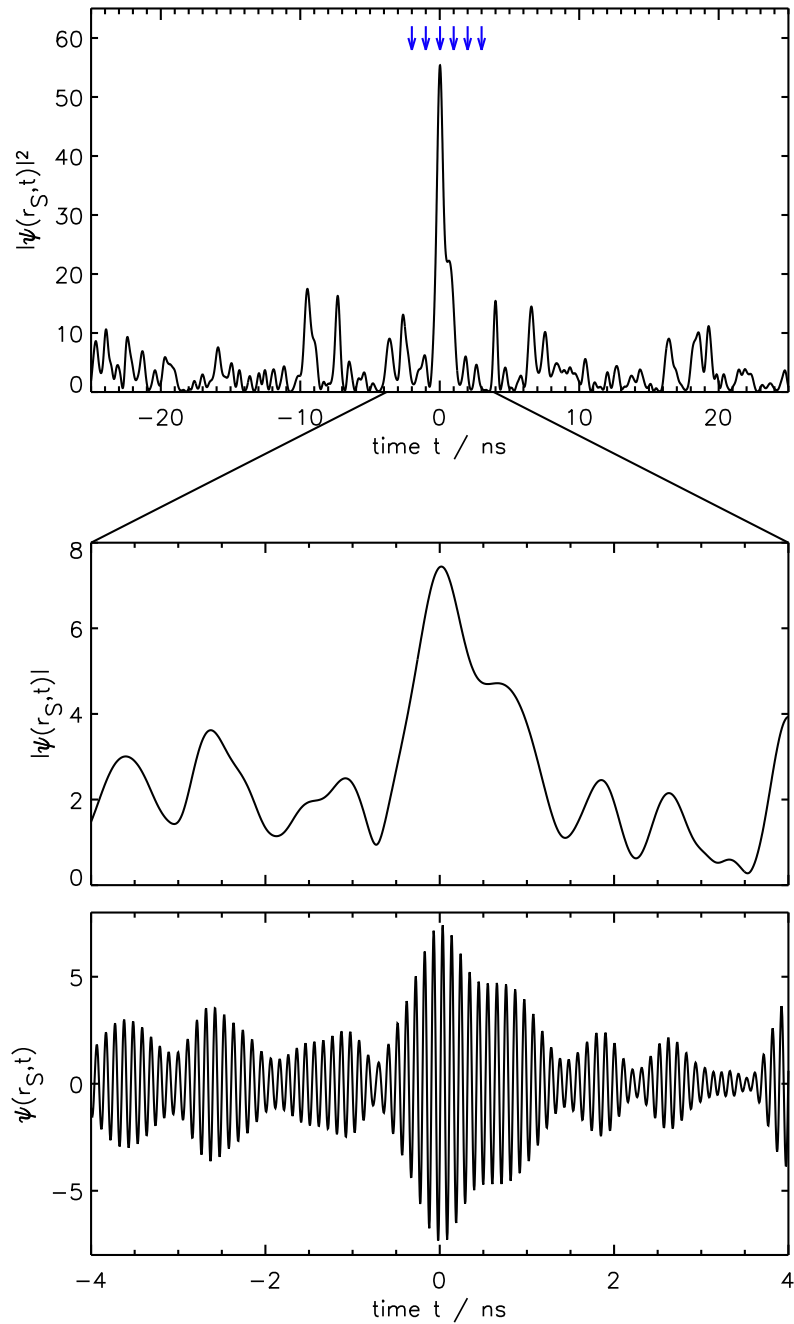


Figure 5.28.: Time evolution in the center of the spot for the event marked by an arrow in the histogram in Fig. 5.26. The arrows indicates the times chosen for the snapshots shown in Fig. 5.29. The lower part shows a blowup of the time evolution for the spot. Here we present the modulus (center) and the real part (bottom) of the wave function.

observable! In the upper part of figure 5.28 the time evolution of the intensity at the spot is presented. In the lower part a blowup of the time evolution around the extreme event is shown. Here we present the modulus of the amplitude and the real part of the

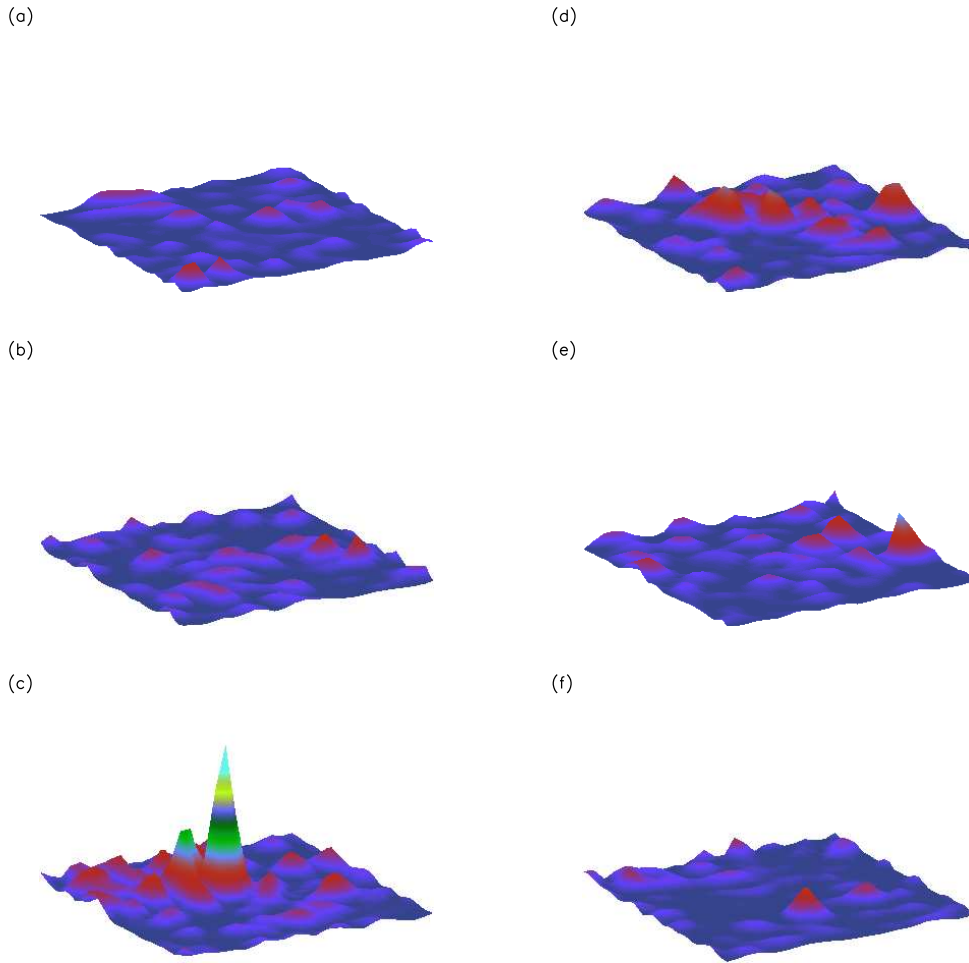


Figure 5.29.: Snapshots of the time evolution of the complete area surrounding the hot spot for the event plotted in red in the histogram in Fig. 5.26. The times used for the snapshot are marked in Fig. 5.28 by arrows.

wave function at the spot. We see for  $t = 0$  a very high peak corresponding to a height of  $I/\langle I \rangle = 55$ .

We want to close our discussion with a sequence of wave functions plotted at 6 different times. We have used the same data for this sequence shows as it was presented in the upper part of figure 5.28. Here we show the wave function for the full field. The first two figures show the wave function shortly before the occurrence of the large amplitude at the spot. The figure in the center shows the wave function where we have recorded the maximal amplitude. The last three figures presents the wave function after the high amplitude wave event.

We have investigated in this chapter the flow pattern of electromagnetic waves through an arrangement of conical scatterers which simulate a soft potential. We have obtained similar results as they were observed in the branched electron flow experiments [Top00, Top01]. This shows that the details of the potential are not of relevance for the found structures. We could additionally show that the branches concentrate on the slopes of

the potential giving rise that caustics are responsible for the branched structure of the flow [Kap02].

Investigating the intensity distribution we found large deviations which could be related to singular points with extreme high intensities. These intensities have been found to be much larger than expected from a random pattern. We went a step further and reinterpreted our results as a realization of a wave field developing in the sea under the influence of spatially varying velocity fields. Computing transient waves from our data we have seen events which exceed considerably the freak wave border. We have seen additionally that although these events have been rare in our analysis they are by orders of magnitude more frequent than expected from a random superposition of waves. This gives a strong support for the conjecture that linear theories are sufficient to produce wave heights needed as input for non-linear instability events [Hel08].



## 6. Summary and outlook

We have presented a number of experimental results which can be described theoretically by random wave models. We have started in chapter 3 with spatial correlation functions in an open microwave billiard. Here we have extended former studies on pair correlation functions of vortex points in the probability flow also to pair correlation functions between vortex and hyperbolic points in the flow. We have seen that if the wave length is comparable with the system size the results of the random wave model have to be adopted to describe the investigated correlation functions correctly. In the study on the quantum stress tensor we got an overall good agreement but also here we had to incorporate system specific features to explain the deviations from the results of the random wave model. In this case a net current being present in our quantum dot experiments was the disturbing non-generic property.

In the second part of this work we have investigated the fidelity for a special class of perturbations. The fidelity is a measure for the time dependent stability of a quantum system against perturbations. We have shown that for a local perturbation, realized by the shift of a small perturber in a microwave billiard, the fidelity decays algebraically with a  $1/t$  long-time behavior. This is in contrast to the exponential or Gaussian long-time behavior observed in the fidelity decay due to global perturbations. All results could be quantitatively explained within the random-plane-wave model, including a scaling prediction on the dependence of the fidelity decay on the perturber shift. In addition we could show that scattering fidelity and ordinary fidelity are identical within the experimental errors.

The experiments on the fidelity are planned to be extended in two more directions. In one case we want to study the fidelity in dependence of the strength of the coupling to the outside. Here we have obtained in our group already preliminary results. In this experiments the change of the coupling shall be realized by varying the antenna coupling of a single antenna. The idea of this measurement is to investigate the effect of unwanted coupling of a quantum system to the outside world which is of relevance in quantum computation. In a second study we want to investigate another type of local perturbation. Here the fidelity decay due to local boundary perturbations shall be investigated. There exist already some theoretical predictions of Arseni Goussev and Klaus Richter [Gou07] who claimed an exponential decay of the fidelity depending on the classical decay rate of a particle moving in the billiard.

In chapter five we have investigated the flow pattern of electromagnetic waves through an arrangement of conical scatterers which simulate a soft potential. We have obtained similar results as they were observed in the branched electron flow experiments [Top00, Top01]. This shows that the details of the potential are not of relevance for the found

structures. We could additionally show that the branches concentrate on the slopes of the potential giving rise that caustics are responsible for the branched structure of the flow [Kap02].

Investigating the intensity distribution we found large deviations which could be related to singular points with extreme high intensities. These intensities have been found to be much larger than expected from a random pattern. We went a step further and reinterpreted our results as a realization of a wave field developing in the sea under the influence of a spatially varying velocity fields. Computing transient waves from our data we have seen events which exceed considerably the freak wave border. We have seen additionally that, although these events have been rare in our analysis, they are by orders of magnitude more frequent than expected from a random superposition of waves. This gives a strong support for the conjecture that linear theories are sufficient to produce wave heights needed as input for non-linear instability events [Hel08].

# A. Bilinear interpolation and nodal line estimation

The problem discussed in this chapter is how to extract the nodal lines of a two-dimensional scalar field which is given on a rectangular grid. We present in the following a procedure which is based on the bilinear interpolation method and which was used to extract approximately the nodal lines for various quantities obtained from our microwave measurements. These are, for example, the wave function, the components of the flow, or the vorticity.

## A.1. The method of bilinear interpolation

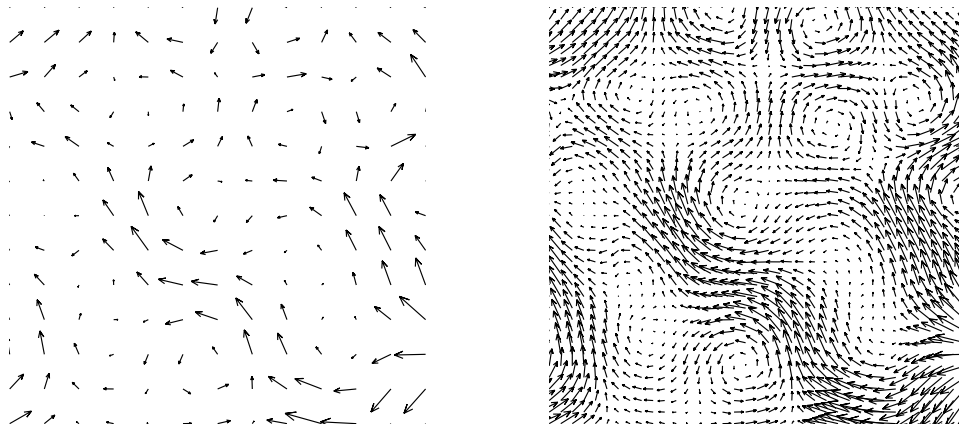


Figure A.1.: Vector field to present the potential of the bilinear interpolation method. In (a) the original field is shown. Here each arrow corresponds to a *measurement point*. In part (b) the field has been interpolated with additional three intermediate points along each axis.

Before we discuss the details of the method we show as an introduction the ability of the bilinear interpolation. We apply this method to a vector field<sup>1</sup> which is shown in figure A.1 in part (a). Each arrow corresponds to a point on the measurement grid. In part (b) of the figure the same vector field is shown but now the density of points has been increased due to the interpolation. This figure shows clearly more structure than the original one since the higher density of vectors are guiding the eyes. Thus vortex and saddle points are better visible as in the original figure.

---

<sup>1</sup>In the case of a vector field the method has to be applied to each component independently.

We now want to present briefly the mathematical background of this method. In what follows we restrict ourselves only on four measurement points which are arranged on a square. Furthermore and without loss of generality we perform a coordinate transformation such that the corner points are represented by the unit square. We denote in the following estimated quantities with capital letters. In figure A.2 we present a sketch to illustrate the interpolation procedure and secondly a small example of a bilinear interpolated function.

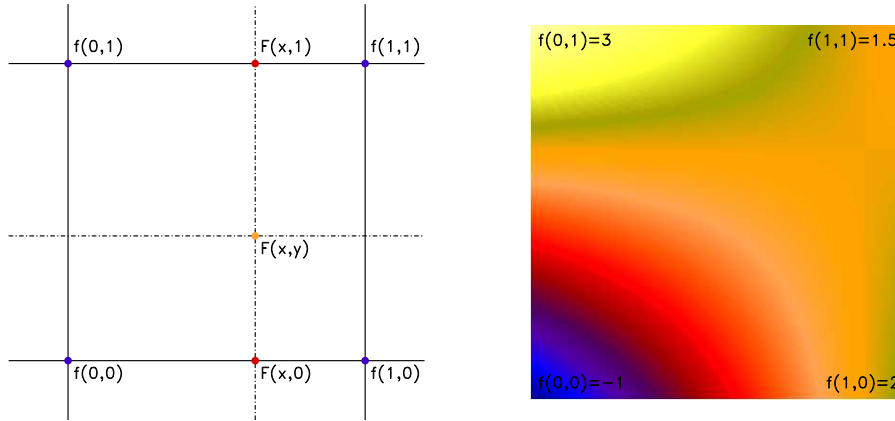


Figure A.2.: In part (a) a sketch to illustrate the bilinear interpolation is shown. The blue points indicate the data points where the function is known. At the orange point the interpolation should be performed. Part (b) of the figure shows a bilinear interpolated function.

We start our approximation with a linear interpolation of the function  $f$  along one arbitrary axis. Here we choose the x-axis and perform this linear interpolation along the upper and lower border of the square. Hence we obtain estimated values for  $F(x, 1)$  and  $F(x, 0)$  (see the red points in Fig. A.2 (a)). Expressed in an equation these two linear interpolations read:

$$F(x, 1) = f(0, 1)(1 - x) + f(1, 1)x \quad (\text{A.1})$$

$$F(x, 0) = f(0, 0)(1 - x) + f(1, 0)x. \quad (\text{A.2})$$

In the next step we have to interpolate again linearly between  $F(x, 1)$  and  $F(x, 0)$ . This yields already an expression for the bilinear interpolation:

$$F(x, y) = F(x, 0)(1 - y) + F(x, 1)y \quad (\text{A.3})$$

$$\begin{aligned} F(x, y) &= f(0, 0)(1 - x)(1 - y) \\ &\quad + f(1, 0)(1 - y)x \\ &\quad + f(0, 1)(1 - x)y \\ &\quad + f(1, 1)xy \end{aligned} \quad (\text{A.4})$$

We can rewrite the last equation into a matrix expression:

$$F(x, y) = \begin{pmatrix} 1 - x \\ x \end{pmatrix}^T \begin{pmatrix} f(0, 0) & f(0, 1) \\ f(1, 0) & f(1, 1) \end{pmatrix} \begin{pmatrix} 1 - y \\ y \end{pmatrix} \quad (\text{A.5})$$

From this one can directly see where the name for the interpolation method comes from. Such a matrix equation defines the bilinear map for the vectors  $\begin{pmatrix} 1-x \\ x \end{pmatrix}$  and  $\begin{pmatrix} 1-y \\ y \end{pmatrix}$ . For the later discussion we go back to eq. A.4 where we expand the products and sort the result for the variables  $x$  and  $y$ . We end up with a very compact expression for the bilinear interpolation:

$$F(x, y) = a_0 + a_1x + a_2y + a_3xy, \quad (\text{A.6})$$

where the coefficients  $a_i$  are given by

$$a_0 = f(0, 0) \quad (\text{A.7})$$

$$a_1 = f(1, 0) - f(0, 0) \quad (\text{A.8})$$

$$a_2 = f(0, 1) - f(0, 0) \quad (\text{A.9})$$

$$a_3 = f(0, 0) + f(1, 1) - f(0, 1) - f(1, 0) \quad (\text{A.10})$$

## A.2. Limits of the bilinear interpolation

In the presentation of figure A.1 we emphasized the potential of the method. Here we also want to discuss the limits of the bilinear interpolation method. It will turn out that these limits are at the same time the limits for our microwave measurements itself.

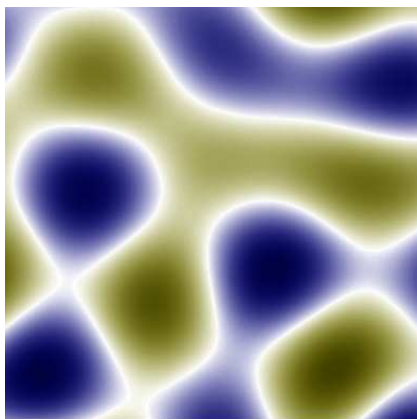


Figure A.3.: A two-dimensional function to illustrate the method of bilinear interpolation

In figure A.3 a typical scalar field is shown. We have constructed this field by a superposition of random plane waves (see chapter 2). For the plotting we have extracted the values of this field on a fictitious measurement grid with  $241 \times 241$  points. We have chosen the wave number  $k$  to be  $0.1 \text{ mm}^{-1}$  and the distance  $\Delta r$  of the grid points to be 1 mm, which yields  $k\Delta r = 0.1$ . In the following discussion we will use this field as our reference and apply the bilinear interpolation for three different densities of base points.

The results of the three different interpolations are shown in figure A.4. We have chosen for the distance  $\Delta r$  of the base points values of 5 mm, 10 mm and 30 mm, which

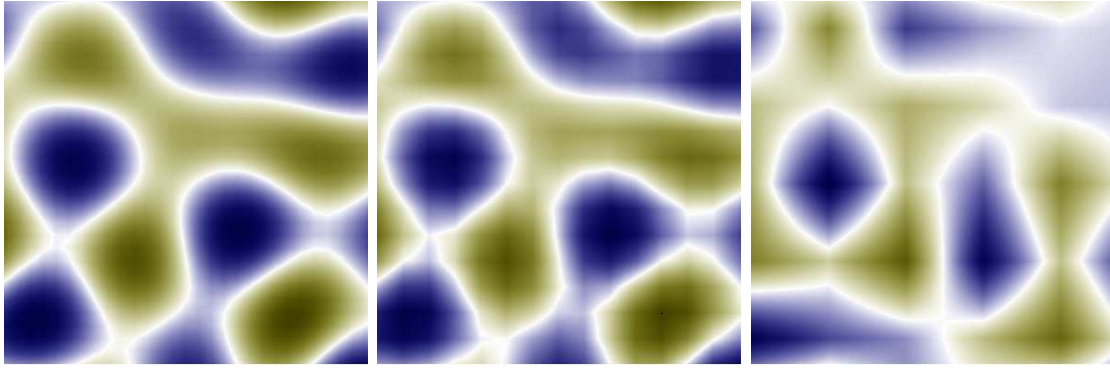


Figure A.4.: Reconstructed wave function from a fictitious measurement grid. The value of  $k\Delta r$  increases from 0.5 (a) over 1 (b) to 3 (c).

corresponds to  $k\Delta r$  of 0.5, 1 and 3. We can see that the method reproduces the function very well in the case of plot (a). Going from (b) to (c) the ability of resampling the true function decreases and even fails to reconstruct the original function in the third plot. This shows directly the limitations of this method which are at the same time the limitations of the experiment, as we probe the field only at discrete points with the antenna. The resolution of the spatial grid should fulfill the condition  $k\Delta r \leq 1$ , where  $k$  is the wave number and  $\Delta r$  the step size of the measurement grid.

### A.3. Nodal lines of an interpolated field

With eq. A.6 we have an approximate expression for the field. From here it is straight forward to calculate the nodal lines that we are interested in. If we set the approximate expression for the field  $F$  to zero and use the theorem of implicit functions we can parameterize the nodal lines for example in dependence of the  $x$ -coordinate:

$$F(x, y) = F(x, G(x)) = 0 \iff G(x) = -\frac{a_0 + a_1 x}{a_2 + a_3 x} \quad (\text{A.11})$$

With the function  $G$  we have the nodal line within one square. There is still a technical point remaining which is to test for each square if the solution of the function  $G$  has support in it. In principle one can obtain three different solutions/behaviours for the nodal line curve  $G$  which correspond to the number of nodal lines in the considered square. There could be no, one or two nodal lines. These three cases are shown in figure A.5.

In the last equation we have obtained an analytical expression for the approximated nodal line of a field  $f(x, y)$ . From here it is again only a technical problem to extract the crossing points of nodal lines of two fields. This is needed for instance in the case of the flow in an open billiard system. Here one is interested in critical points of the flow where the current vanishes which means the nodal lines of the  $x$ -component and those of the  $y$ -component intersect each other.

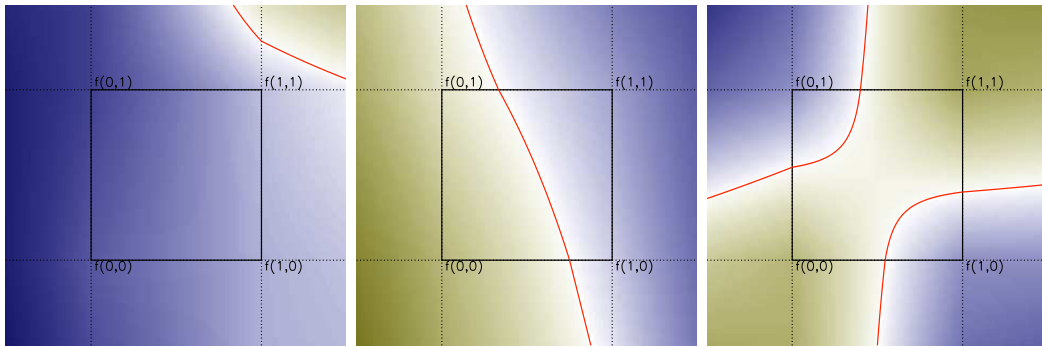


Figure A.5.: We show here the three possible solutions for the nodal line function  $G$ . In the left part no nodal line exists in the region of interest. In the center the field has one nodal. In the right part two nodal lines are obtained in the region of interest.



## B. Critical point analysis

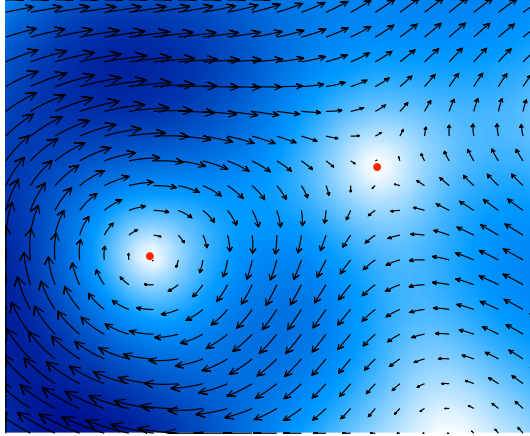


Figure B.1.: Part of a flow calculated from a wave function. In the flow two critical points are visible. The background color indicates the magnitude of the flow, where darker color means stronger flow. The small red spots are placed at the nodal points of the flow.

In appendix A we have discussed the extraction of the nodal lines and nodal points of a scalar field. In this section we want to present a method which is able to classify automatically a critical point. As an example for critical points in the flow we show in figure B.1 the two major types of critical points which we have found in the experiment. The method of the classification goes back to a diagonalization of a linear map describing the flow in the vicinity of the critical point. The presented method is strongly related to the analysis of fixed points in dynamical systems.

For the following let us assume that we have an arbitrary two-dimensional vector field  $\vec{u}(\vec{r})$  which depends only on the position  $\vec{r} = (x, y)^T = (r_1, r_2)^T$ . We then can approximate each component of the field  $\vec{u}$  in the vicinity of a given point  $\vec{a}$  with a Taylor series up to the linear term:

$$\tilde{u}_i(\vec{r}) = u_i(\vec{a}) + \sum_{k=1}^2 \partial_k u_i(\vec{a}) \cdot (r_k - a_k) + \dots \quad (\text{B.1})$$

We can specialize the last equation for two more assumptions. First we may apply a coordinate transformation such that  $\vec{a} = \vec{0}$ . Secondly we assume that the vector field vanishes at the origin which corresponds to the situation of a critical point in the probability flow. Thereby we can simplify equation B.1 to:

$$\tilde{u}_i(\vec{r}) = \sum_{k=1}^2 \partial_k u_i(\vec{0}) \cdot r_k. \quad (\text{B.2})$$

If we introduce the notation

$$A_{ik} = \partial_k u_i(\vec{0}), \quad (\text{B.3})$$

we see that the sum in equation B.2 is nothing more than a matrix-vector multiplication. Thus we end up with:

$$\vec{u}(\vec{r}) = A\vec{r}. \quad (\text{B.4})$$

Up to this point we have seen that one can approximate a vector field in the vicinity of a critical point by a linear map. The vector field we have studied in chapter 3 was the probability flow  $\vec{j}(\vec{r})$ . If we adopt the notation to the probability flow we can write for the approximated flow near a critical point:

$$\vec{j}(\vec{r}) = A\vec{r}, \quad (\text{B.5})$$

where  $A$  is the matrix describing the linear map and  $\vec{r}$  is the position. By a study of the eigenvalues of the matrix  $A$  we can obtain information about the type of critical points. We therefore have to calculate this matrix from our data. In principle it is possible to obtain the entries of the matrix by the definition we made in equation B.3. But as it involves a derivative of the flow we will use another way to calculate the matrix elements. For this method we choose two points  $\vec{r}^{(1)}$  and  $\vec{r}^{(2)}$  in the neighborhood of such a critical point and calculate the flow  $\vec{j}^{(1)}$  and  $\vec{j}^{(2)}$  at these two points with a bilinear interpolation. For each single point we get the following set of two equations:

$$\begin{aligned} \vec{j}_1^{(i)} &= A_{11}r_1^{(i)} + A_{12}r_2^{(i)} \\ \vec{j}_2^{(i)} &= A_{21}r_1^{(i)} + A_{22}r_2^{(i)} \end{aligned} \quad (\text{B.6})$$

where the upper index  $i$  denotes the two different points and is either 1 or 2. We can now construct a linear equation to obtain the matrix elements of the matrix  $A$ :

$$\begin{pmatrix} r_1^{(1)} & r_2^{(1)} & 0 & 0 \\ 0 & 0 & r_1^{(1)} & r_2^{(1)} \\ r_1^{(2)} & r_2^{(2)} & 0 & 0 \\ 0 & 0 & r_1^{(2)} & r_2^{(2)} \end{pmatrix} \begin{pmatrix} A_{11} \\ A_{12} \\ A_{21} \\ A_{22} \end{pmatrix} = \begin{pmatrix} j_1^{(1)} \\ j_2^{(1)} \\ j_1^{(2)} \\ j_2^{(2)} \end{pmatrix} \quad (\text{B.7})$$

The thus calculated matrix  $A$  can be diagonalized and we obtain as a result two eigenvalues  $\lambda_1$  and  $\lambda_2$ . In our case the eigenvalues can have the following properties:

Eigenvalue relation	Flow behaviour
$\lambda_1 = \lambda_2^*$ and $\text{Re}(\lambda_{1,2}) < 0$	vortex point
$\lambda_1, \lambda_2$ real and $\lambda_1 < 0 < \lambda_2$	saddle point
$\lambda_1 = \lambda_2$ , $\lambda_1, \lambda_2$ real and $\lambda_1, \lambda_2 < 0$	sink point

Table B.1.: Possible properties of the eigenvalues of  $A$  for the experimental flow.

In addition to the vortex and saddle points we find in the experiment a third class of points which we call sink points. These points occur when the coupling of the two

---

attached wave guides is comparable with the coupling of the probe antenna. In this case the probe antenna can be a sink of the electromagnetical field inside the cavity.

With this efficient method combined with the nodal line estimation it is possible to obtain all vortex and saddle points of a few hundred wave function patterns in about ten minutes.



# C. Theoretical expressions for the pair correlation functions

Here we collect some theoretical expressions of the pair correlation functions of critical points in a flow. Additionally we present the density functions of critical points from a straight boundary. All functions involving saddle points of the flow have been calculated by J. D. Urbina and M. Dennis and will be published in a forthcoming joint publication [Höhma08]. For completeness we will present also older results on correlation functions obtained by M. Dennis and M.V. Berry [Ber00, Den01] and by A.I. Saichev et. al. [Sai01]. For further details concerning the derivations and further explanations we refer the reader to the original publications.

## C.1. Pair correlation functions

In the calculations of pair correlation functions of vortex points  $g_{vv}(r)$  the spatial autocorrelation function  $C(|\vec{r}|)$  is a main ingredient. In the following we will use the dimensionless distance  $R = k|\vec{r}|$

$$C(R) = J_0(R) \tag{C.1}$$

where  $J_0$  is the Bessel function of the normal kind. To be able to express the vortex-vortex pair correlation function  $g_{vv}(R)$  in a compact way we need the following abbreviations [Ber00]:

$$\begin{aligned} C &= C(R) \\ E &= C'(R) \\ H &= -C'(R)/R \\ F &= -C''(R) \\ F_0 &= -C''(0) \end{aligned} \tag{C.2}$$

where  $'$  denotes the standard derivative. Secondly we need some combinations of these functions:

$$\begin{aligned} D_1 &= [E^2 - (1 + C)(F_0 - F)][E^2 - (1 - C)(F_0 + F)] \\ D_2 &= F_0^2 - H^2 \\ Y &= \frac{H^2(CE^2 - F(1 - C^2))^2}{F_0^2(E^2 - F_0(1 - C^2))^2} \\ Z &= \frac{D_1 D_2 (1 - C^2)}{F_0^2(E^2 - F_0(1 - C^2))^2} \end{aligned} \tag{C.3}$$

With all these abbreviations one ends up with the following integral which can be evaluated numerically:

$$g_{vv}(R) = \frac{2(E^2 - F_0(1 - C^2))}{\pi F_0(1 - C^2)} \int_0^\infty dt \frac{3 - Z + 2Y + (3 + Z - 2Y)t^2 + 2Zt^4}{(1 + t^2)^3 \sqrt{1 + (1 + Z - Y)t^2 + Zt^4}} \quad (\text{C.4})$$

The charge correlation function  $g_Q(R)$  which accounts also for the chirality of the vortex points, can be expressed in a much nicer way [Ber00, Höhma08]:

$$g_Q(R) = \frac{4}{R} \frac{d}{dR} \left[ \frac{d \arcsin(J_0(R))}{dR} \right]^2 \quad (\text{C.5})$$

We have seen above that the calculation of the vortex pair correlation function needs a number of combinations of the autocorrelation function and its derivatives. Finally one ends up with an integral which cannot be solved analytically. The situation for the vortex-saddle pair correlation function  $g_{vs}$  is even worse. Here it was not possible to obtain an expression for this function (see [Höhma08]). The same is true for the saddle-saddle pair correlation function  $G_{ss}$ . Alternatively one can express the autocorrelation function  $C(R)$  which is nothing more than the Bessel function  $J_0$  by its asymptotic approximation. The leading order term is:

$$C(R) \stackrel{R \gg 1}{\approx} \sqrt{\frac{2}{\pi R}} \cos(R - \pi/4). \quad (\text{C.6})$$

Thereby one obtains quite simple relations for the pair correlation functions:

$$g_{vv}(R) \sim 1 + \frac{4 \sin 2R}{\pi R}, \quad (\text{C.7})$$

$$g_{vs}(R) \sim 1 - \frac{4 \sin 2R}{\pi R}, \quad (\text{C.8})$$

$$g_{ss}(R) \sim 1 + \frac{4 \sin 2R}{\pi R}. \quad (\text{C.9})$$

## C.2. Densities of critical points from a straight boundary

In the same way as for the pair correlation functions we need to express the density of vortices or saddles in dependence from their distance from a straight boundary some abbreviations. Here we define the 1-point quadratic field correlation  $B(Y)$  where  $Y$  is the dimensionless distance  $ky$  from the boundary. For Dirichlet boundary conditions  $B(Y)$  is:

$$B(Y) = 1 - J_0(2Y). \quad (\text{C.10})$$

The result for the density of vortices from a straight boundary has already been calculated by K.-F. Berggren et. al. [Ber02]. M. Dennis and J.D. Urbina extended this to the saddle point density. For the vortices we have:

$$\rho_v(Y) = \frac{\sqrt{4B + B'' - 1}\sqrt{B(2 + B'') - B'^2}}{2B^{3/2}}. \quad (\text{C.11})$$

In case of the saddle points one obtains a very lengthy expression [Höhma08]:

$$\begin{aligned} \rho_s(Y) = & \frac{2B^{1/2}}{2(4B + B'' - 1)^{3/2}(B(2 + B'') - B'^2)^{3/2}} \\ & \times (16 - 64B + 64B^2 + 16B'^2 - 64BB'^2 \\ & + 16B'^4 - 16B'' + 64B^2B'' - 32BB'^2B'' \\ & + 16BB''^2 + 16B^2B''^2 - 4B'^2B''^2 \\ & + 4B''^3 - B''^4 + 8B'B''' - 32BB'B''' \\ & + 8B'^3B''' - 8B'B''B''' + 2B'B''^2B''' \\ & - 4B^2B''^2 + B'^2B''^2 - 2BB''B''^2 \\ & - 8BB'''' + 16B^2B'''' + 4B'^2B'''' \\ & - 8BB'^2B'''' + 8B^2B''B'''' \\ & - 2B'^2B''B'''' + 2BB''^2B''''). \end{aligned} \quad (\text{C.12})$$



## D. Calculation of the period shift in correlation functions

Let us consider the function

$$g(kx) = e^{-u(kx)} \cos(kx) \quad (\text{D.1})$$

where  $u(kx)$  describes the decay of the oscillation. In all cases considered here the decay is algebraic, i.e.

$$u(kx) = n \ln(kx) \quad (\text{D.2})$$

The phase shift  $-\pi/4$  for the Bessel functions is irrelevant here, and will not be considered in the following. Convolution by a Gaussian function yields

$$g_{\text{conv}}(kx) = \Re \left[ \frac{1}{\sqrt{\pi\delta}} \int d\bar{k} e^{-u(\bar{k}x) - i\bar{k}x - \frac{(\bar{k}-k)^2}{2\delta^2}} \right] \quad (\text{D.3})$$

Expanding  $u(kx)$  up to the linear term at  $\bar{k} = k$  and taking only terms linear in  $u'(kx)$  the integration can be done with the result

$$g_{\text{conv}}(kx) = e^{-u(kx)} \cos(k_{\text{eff}}x) e^{-\frac{\delta^2 x^2}{2}} \quad (\text{D.4})$$

where  $k_{\text{eff}} = sk$  and

$$s = 1 + \frac{\delta^2 x}{k} u'(kx) \quad (\text{D.5})$$

With expression (D.2) for  $g(kx)$  one ends with expression (3.5) for the stretching factor  $s$ .



## E. Calculation of the variance of the level velocity distribution

We have used in chapter 4 the variance of the level velocities to extract the only free parameter  $\alpha$  which was left over in our analysis. In [Bar99] is a small missprint so we redo the calculation in slightly different way for the distribution of the level velocities. Before we start with the derivation of the distribution function we want to collect some definitions and calculations which are shared in two different calculations. First we present the definition of the level velocity. From equation 4.10 we can calculate the velocity of the energy levels when moving the perturber from point  $x_1$  to  $x_2$ :

$$v = \frac{\Delta E}{\Delta x} = \alpha \frac{\psi^2(x_1) - \psi^2(x_2)}{x_1 - x_2}, \quad (\text{E.1})$$

Having calculated the distribution one can easily calculate the second moment e. g. the variance. This calculation will be presented in the first section of this chapter. In the second section we will present a more compact way to calculate the variance and higher order moments of Gaussian distributed fields. For the following calculations we need the expression

$$\lim_{\Delta x \rightarrow 0} \frac{1}{\Delta x} [1 - (J_0(k\Delta x))^2]. \quad (\text{E.2})$$

This can be done quite easily if we expand the Bessel function in a Taylor series. For small  $z$  we can approximate  $J_0(z)$  and  $J_0^2(z)$ :

$$J_0(z) = 1 - \frac{z^2}{4} + \mathcal{O}(z^4), \quad (\text{E.3})$$

$$J_0^2(z) = 1 - \frac{z^2}{2} + \mathcal{O}(z^4). \quad (\text{E.4})$$

If we use this approximate expression and apply it to eq. E.2 we obtain

$$\lim_{\Delta x \rightarrow 0} \frac{1}{\Delta x} [1 - (J_0(k\Delta x))^2] = \frac{k^2}{2}. \quad (\text{E.5})$$

Calculating averages where the amplitude of the wave function in a chaotic billiard is involved mostly needs the calculation of a two point correlation function of the following type  $\langle \psi(x_1)\psi(x_2) \rangle$ . This can be done using the random plane wave assumption for chaotic billiards of Berry [Ber77]. One obtains for the two-point correlation function:

$$\langle \psi(x_1)\psi(x_2) \rangle = \frac{1}{A} J_0(k|x_1 - x_2|) \quad (\text{E.6})$$

where  $A$  is the billiard area and  $k$  the wave number. Later on we will use the shorthand notation  $\langle \psi_1 \psi_2 \rangle = \langle \psi(x_1) \psi(x_2) \rangle$  and  $\Delta x = |x_1 - x_2|$ . For  $\Delta x = 0$  the two-point correlation function reduces to  $\langle \psi^2 \rangle = \frac{1}{A}$ .

## E.1. Calculation using the distribution function

In this section we want to present a pedestrian way to calculate the distribution function for the level velocities of a chaotic billiard system. The calculation is analogous to the one for the fidelity amplitude in section 4.3.

$$\begin{aligned} P(v) &= \langle \delta(v - \alpha \frac{\psi_1^2 - \psi_2^2}{\Delta x}) \rangle \\ &= \frac{\sqrt{|K|}}{2\pi} \int_{-\infty}^{\infty} \int_{-\infty}^{\infty} \int_{-\infty}^{\infty} dt d\psi_1 d\psi_2 e^{vt} e^{-\frac{1}{2}(\psi_1, \psi_2) \tilde{K} (\psi_1, \psi_2)^T}, \end{aligned} \quad (\text{E.7})$$

where we have used the following abbreviations

$$\begin{aligned} \tilde{K} &= K + \frac{2i\alpha t}{\Delta x} \delta \\ \delta &= \begin{pmatrix} 1 & \cdot \\ \cdot & -1 \end{pmatrix} \\ K^{-1} &= \begin{pmatrix} \langle \psi_1 \psi_1 \rangle & \langle \psi_1 \psi_2 \rangle \\ \langle \psi_2 \psi_1 \rangle & \langle \psi_2 \psi_2 \rangle \end{pmatrix} \end{aligned}$$

The Gaussian integration over  $\psi_1$  and  $\psi_2$  yields the following:

$$\begin{aligned} P(v) &= \frac{1}{2\pi} \int_{-\infty}^{\infty} dt e^{vt} \left( \frac{|K|}{|K + \frac{2i\alpha t}{\Delta x} \delta|} \right)^{\frac{1}{2}} \\ &= \frac{1}{2\pi} \int_{-\infty}^{\infty} dt e^{vt} \left| \mathbb{1} + \frac{2i\alpha t}{\Delta x} \delta K^{-1} \right|^{-\frac{1}{2}} \end{aligned} \quad (\text{E.8})$$

Evaluating the determinant and using the results from equations E.6 for the two-point correlation function we obtain the following expression

$$P(v) = \frac{1}{2\pi} \int_{-\infty}^{\infty} dt e^{vt} \left[ 1 + \left( \frac{2\alpha t}{A\Delta x} \right)^2 (1 - J_0^2(k\Delta x)) \right] \quad (\text{E.9})$$

We now perform the transition for  $\Delta x \rightarrow 0$  (see eq. E.5) and define a new variable  $\beta := \frac{A}{\sqrt{2\alpha k}}$ . We then obtain

$$P(v) = \frac{\beta}{\pi} \int_0^{\infty} dt e^{vt} \frac{1}{\sqrt{\beta^2 + t^2}} \quad (\text{E.10})$$

The fourier integral can be found for instance in [Bro95] and we end up with the final result for the level velocity distribution function

$$P(v) = \frac{\beta}{\pi} K_0(\beta|v|) \quad (\text{E.11})$$

where  $K_0$  is the modified Bessel function of the first kind. In a last step we have to calculate the second moment of this distribution function:

$$\langle v^2 \rangle = \int_{-\infty}^{\infty} v^2 P(v) dv = \frac{2\beta}{\pi} \int_0^{\infty} v^2 K_0(\beta|v|) = \frac{1}{\beta^2} = \frac{2\alpha^2 k^2}{A^2} \quad (\text{E.12})$$

## E.2. Calculation of higher order moments of Gaussian random variables

For the next and more direct approach to calculate the second moment of the level velocity distribution we use Wick's Theorem to calculate the expectation value of a product of Gaussian distributed variables:

$$\langle A_1 A_2 \dots A_n \rangle = \begin{cases} 0 & n \text{ odd} \\ \sum_{P_D} \langle A_1 A_2 \rangle \dots \langle A_{n-1} A_n \rangle & n \text{ even} \end{cases} \quad (\text{E.13})$$

where the sum has to be performed over all permutations yielding distinct pairs for the two-point correlation functions  $\langle A_i A_j \rangle$ . As we will need this expression later on and also illustrate this method we calculate the expectation value for  $n = 4$ :

$$\begin{aligned} \langle A_1 A_2 A_3 A_4 \rangle &= \langle A_1 A_2 \rangle \langle A_3 A_4 \rangle \\ &+ \langle A_1 A_3 \rangle \langle A_2 A_4 \rangle \\ &+ \langle A_1 A_4 \rangle \langle A_2 A_3 \rangle. \end{aligned} \quad (\text{E.14})$$

We specialize this result for two important examples. If  $A_3 = A_1$  and  $A_4 = A_2$  we obtain

$$\langle A_1^2 A_2^2 \rangle = \langle A_1^2 \rangle \langle A_2^2 \rangle + 2 \langle A_1 A_2 \rangle^2, \quad (\text{E.15})$$

and if  $A_1 = A_2 = A_3 = A_4$  we have

$$\langle A_1^4 \rangle = 3 \langle A_1^2 \rangle. \quad (\text{E.16})$$

With this we are prepared to calculate the second moment of the velocity distribution. We have defined in eq. (E.1) the level velocity. Using this definition we get

$$\langle v^2 \rangle = \frac{\alpha^2}{\Delta x^2} [\langle \psi_1^4 \rangle - 2 \langle \psi_1^2 \psi_2^2 \rangle + \langle \psi_2^4 \rangle] \quad (\text{E.17})$$

$$= \frac{\alpha^2}{\Delta x^2} [3 \langle \psi_1^2 \rangle - 2 (\langle \psi_1^2 \rangle \langle \psi_2^2 \rangle + 2 \langle \psi_1 \psi_2 \rangle^2) + 3 \langle \psi_2^2 \rangle] \quad (\text{E.18})$$

$$= \frac{\alpha^2}{\Delta x^2} [\langle \psi_1^2 \rangle - \langle \psi_1 \psi_2 \rangle^2] \quad (\text{E.19})$$

Where we have used in the last step  $\langle \psi_1^2 \rangle = \langle \psi_2^2 \rangle$ . With eq. (E.6) we get the following expression for the variance of the level velocity distribution

$$\langle v^2 \rangle = \frac{4\alpha^2}{A^2} \frac{1}{\Delta x} [1 - (J_0(k\Delta x))^2] . \quad (\text{E.20})$$

Performing the limit  $\Delta x \rightarrow 0$  we obtain with equation E.5 the final result:

$$\langle v^2 \rangle = \frac{2\alpha^2 k^2}{A^2} \quad (\text{E.21})$$

in accordance with equation E.12.

# List of Figures

2.1. Sketch to describe the scattering process . . . . .	6
2.2. Wave function measurement table . . . . .	7
3.1. Sketch of the open microwave cavity . . . . .	13
3.2. Typical wave function in an open cavity . . . . .	14
3.3. Figure to illustrate critical points in open billiard systems . . . . .	15
3.4. Vortex pair correlation function . . . . .	17
3.5. Pair correlation function of vortex and saddle points . . . . .	18
3.6. Density of vortex and saddle points against a straight wall . . . . .	18
3.7. Distribution of nearest neighbor distances for critical points in the flow .	20
3.8. Finite size effects of the pair correlation function (period stretching) . . .	21
3.9. Spatial auto correlation function . . . . .	22
3.10. Spatially resolved intensity, flow and stress tensor components . . . . .	27
3.11. Experimental distributions of the quantum stress tensor components (I) .	28
3.12. Quantifying the net current observed in the experiment . . . . .	29
3.13. Experimental distributions of the quantum stress tensor components (II)	30
3.14. Quantifying the net current observed in the numerical data . . . . .	31
3.15. Distributions of the quantum stress tensor components from numerical data . . . . .	32
4.1. Part of the reflection spectrum and the experimental setup . . . . .	36
4.2. Results for the scattering fidelity . . . . .	38
4.3. Results for the ordinary fidelity . . . . .	39
4.4. Comparison between scattering and ordinary fidelity . . . . .	39
5.1. General setup for the rogue wave analogue measurement . . . . .	42
5.2. Sketch of the cones and the corresponding potential . . . . .	43
5.3. Wave function of the free wave propagation . . . . .	45
5.4. Angle averaged wave function of the free wave propagation . . . . .	45
5.5. Theoretical wave function of the free wave propagation . . . . .	46
5.6. Background which cannot be described by the free wave propagation . . . .	46
5.7. Antenna coupling for the two lowest modes . . . . .	47
5.8. Wave scattering at a single scatterer of conical shape . . . . .	48
5.9. Scattering at a single scatterer of conical shape for individual modes . . .	48
5.10. Scattering at a single scatterer – comparison of the ray simulation with the experiment . . . . .	49
5.11. Wave scattering at two scatterers of conical shape . . . . .	50
5.12. Wave scattering at two scatterers of conical shape for individual modes . .	50

5.13. Ray simulation of the $TM_1$ mode for the scattering at two cones . . . . .	50
5.14. Sketch of the setup for the first scatterer arrangement . . . . .	52
5.15. Sketch of the setup for the second scatterer arrangement . . . . .	52
5.16. Intensity of a measured and simulated wave function for $\nu = 30.95$ GHz .	53
5.17. Blow up of a measured and simulated wave function for $\nu = 30.95$ GHz .	53
5.18. Intensity of two measured wave functions at the frequencies 10.03 GHz and 9.53 GHz . . . . .	53
5.19. Plot of the radial decline seen in the wavefunction . . . . .	54
5.20. The intensity of two measured wave functions at the frequencies 10.03 GHz and 9.53 GHz with removed decay . . . . .	55
5.21. Data segmentation . . . . .	55
5.22. Intensity distribution of different parts in the billiard . . . . .	56
5.23. Sketch of the setup for the measurement of transient waves . . . . .	58
5.24. Intensity of the spot versus the frequency . . . . .	59
5.25. Intensity of the spot versus position of the fixed antenna . . . . .	59
5.26. Intensity distribution of the transient waves . . . . .	61
5.27. Local mean intensity for each point of the transient measurement . . . .	62
5.28. Time evolution at the spot for a transient wave . . . . .	63
5.29. Time evolution of a subfield for a transient wave . . . . .	64
A.1. Example bilinear interpolation . . . . .	69
A.2. Sketch to explain the function of the bilinear interpolation . . . . .	70
A.3. Test function to illustrate the limits of bilinear interpolation . . . . .	71
A.4. Different interpolations of a test function . . . . .	72
A.5. Possible nodal line configurations obtained from a bilinear interpolation .	73
B.1. Figure of a flow pattern . . . . .	75

# Bibliography

- [Abr61] A. Abragam. *The Principles of Nuclear Magnetism*. University Press Oxford (1961).
- [Aur93] R. Aurich and F. Steiner. Statistical properties of highly excited quantum eigenstates of a strongly chaotic system. *Physica D* **64**, 185 (1993).
- [Bäcke99] A. Bäcker and R. Schubert. Chaotic eigenfunctions in momentum space. *J. Phys. A* **32**, 4795 (1999).
- [Bäcke02] A. Bäcker and R. Schubert. Autocorrelation function of eigenstates in chaotic and mixed systems. *J. Phys. A* **35**, 539 (2002).
- [Bar99] M. Barth, U. Kuhl, and H.-J. Stöckmann. Global versus local billiard level dynamics: The limits of universality. *Phys. Rev. Lett.* **82**, 2026 (1999).
- [Bar01] M. Barth. *Mikrowellen-Experimente zu Leveldynamik und Wirbelbildung*. Dissertation Philipps-Universität Marburg (2001).
- [Bar02] M. Barth and H.-J. Stöckmann. Current and vortex statistics in microwave billiards. *Phys. Rev. E* **65**, 066208 (2002).
- [BB92] I. Bialynicki-Birula, M. Cieplak, and J. Kaminski. *The Theory of Quanta*. Oxford University Press Oxford (1992).
- [Ber77] M. V. Berry. Regular and irregular semiclassical wavefunctions. *J. Phys. A* **10**, 2083 (1977).
- [Ber00] M. V. Berry and M. R. Dennis. Phase singularities in isotropic random waves. *Proc. R. Soc. Lond. A* **456**, 2059 (2000).
- [Ber02] K.-F. Berggren, A. F. Sadreev, and A. A. Starikov. Crossover from regular to irregular behavior in current flow through open billiards. *Phys. Rev. E* **66**, 016218 (2002).
- [Ber08a] K.-F. Berggren, D. N. Maksimov, A. F. Sadreev, R. Höhmann, U. Kuhl, and H.-J. Stöckmann. Quantum stress in chaotic billiards. Preprint (2008). arXiv:0711.1438.
- [Ber08b] M. V. Berry and M. R. Dennis. Boundary-condition-varying circle billiards and gratings: the Dirichlet singularity. *J. Phys. A* **41**, 135203 (2008).
- [Boh84] O. Bohigas, M. J. Giannoni, and C. Schmit. Characterization of chaotic spectra and universality of level fluctuation laws. *Phys. Rev. Lett.* **52**, 1 (1984).

- [Bro95] I. N. Bronstein, K. A. Semendjajew, G. Musiol, and K. Mühlig. *Taschenbuch der Mathematik*. Harri Deutsch Thun (1995).
- [Cer02] N. R. Cerruti and S. Tomsovic. Sensitivity of wave field evolution and manifold stability in chaotic systems. *Phys. Rev. Lett.* **88**, 054103 (2002).
- [Cro03] R. Crook, C. G. Smith, A. C. Graham, I. Farrer, H. E. Beere, and D. A. Ritchie. Imaging fractal conductance fluctuations and scarred wave functions in a quantum billiard. *Phys. Rev. Lett.* **91**, 246803 (2003).
- [Dan03] H. Dankert, J. Horstmann, S. Lehner, and W. Rosenthal. Detection of wave groups in SAR images and radar image sequences. *IEEE Trans. on Geoscience and Remote Sensing* **41**, 1437 (2003).
- [Den01] M. R. Dennis. Local properties and statistics of phase singularities in generic wavefields. *Proc. SPIE* **4403**, 13 (2001).
- [Dor90] E. Doron, U. Smilansky, and A. Frenkel. Experimental demonstration of chaotic scattering of microwaves. *Phys. Rev. Lett.* **65**, 3072 (1990).
- [Dörr98] U. Dörr. *Eigenmodenuntersuchungen am dreidimensionalen Mikrowellen-Sinabillard*. Dissertation Philipps-Universität Marburg (1998).
- [Doy02] V. Doya, O. Legrand, F. Mortessagne, and C. Miniatura. Light scarring in an optical fiber. *Phys. Rev. Lett.* **88**, 014102 (2002).
- [Ebe84] K. J. Ebeling. Statistical properties of random wave fields. In W. P. Mason and R. N. Thurston, editors, *Semi-Classical Approximation in Quantum Mechanics. In: Mathematical Physics and Applied Mathematics 7, Contemporary Mathematics 5. Dordrecht etc.* volume 17 page 233. Academic Press New York (1984).
- [Eck99] B. Eckhardt, U. Dörr, U. Kuhl, and H.-J. Stöckmann. Correlations of electromagnetic fields in irregular cavities. *Europhys. Lett.* **46**, 134 (1999).
- [Fol86] N. O. Folland. Microscopic stress tensors in quantum systems. *Phys. Rev. B* **34**, 8296 (1986).
- [Fra04] K. M. Frahm, R. Fleckinger, and D. L. Shepelyansky. Quantum chaos and random matrix theory for fidelity decay in quantum computations with static imperfections. *Eur. Phys. J. D* **29**, 139 (2004).
- [Fri95] U. Frisch. *Turbulence: The Legacy of A. N. Kolmogorov*. Cambridge University Press Cambridge (1995).
- [God88] M. J. Godfrey. Stress field in quantum systems. *Phys. Rev. B* **37**, 10176 (1988).
- [God90] M. J. Godfrey. Quantum-mechanical stress field in  $H_2^+$ . *J. Phys. B* **23**, 2427 (1990).
- [Goo07] J. W. Goodman. *Speckle Phenomena in Optics: Theory and Applications*. Ben Roberts & Co. Greenwood Village, CO (2007).

- 
- [Gor04] T. Gorin, T. Prosen, and T. H. Seligman. A random matrix formulation of fidelity decay. *New J. of Physics* **6**, 20 (2004).
- [Gou07] A. Goussev and K. Richter. Loschmidt-echo decay from local boundary perturbations. *Phys. Rev. E* **75**, 015201(R) (2007).
- [Gräf92] H.-D. Gräf, H. L. Harney, H. Lengers, C. H. Lewenkopf, C. Rangacharyulu, A. Richter, P. Schardt, and H. A. Weidenmüller. Distribution of eigenmodes in a superconducting stadium billiard with chaotic dynamics. *Phys. Rev. Lett.* **69**, 1296 (1992).
- [Gut90] M. C. Gutzwiller. *Chaos in Classical and Quantum Mechanics*. Interdisciplinary Applied Mathematics, Vol. 1. Springer New York (1990).
- [Haa01] F. Haake. *Quantum Signatures of Chaos. 2nd edition*. Springer Berlin (2001).
- [Hav00] S. Haver and O. J. Anderson. Freak waves: Rare realizations of a typical population or typical realizations of a rare population? *Proc. ISOPE Conference* **3**, 123 (2000).
- [Hel08] E. J. Heller, L. Kaplan, and A. Dahlen. Refraction of a Gaussian seaway. Preprint (2008). nlin.CD/08010613.
- [Höhma08] R. Höhmann, U. Kuhl, J. D. Urbina, M. R. Dennis, and H.-J. Stöckmann. Correlation functions of vortex and saddle points in open billiard system. Preprint (2008). to be published.
- [Hol93] P. R. Holland. *The quantum theory of motion : an account of the de Broglie-Bohm causal interpretation of quantum mechanics*. Cambridge Univ. Pr. Cambridge (1993).
- [Hönts04] J. Höntschel, R. Stenzel, and W. Klix. Simulation of quantum transport in monolithic ICs based on In<sub>0.53</sub>Ga<sub>0.47</sub>As-In<sub>0.52</sub>Al<sub>0.48</sub>As RTDs and HEMTs with a quantum hydrodynamic transport model. *IEEE Trans. on Electron Devices* **51**, 684 (2004).
- [Jac82] J. D. Jackson. *Klassische Elektrodynamik, 2. Auflage*. de Gruyter Berlin (1982).
- [Kap02] L. Kaplan. Statistics of branched flow in a weak correlated random potential. *Phys. Rev. Lett.* **89**, 184103 (2002).
- [Kha03] C. Kharif and E. Pelinovsky. Physical mechanisms of the rogue wave phenomenon. *Eur. J. Mech. B* **22**, 603 (2003).
- [Kim02] Y.-H. Kim, M. Barth, H.-J. Stöckmann, and J. P. Bird. Wavefunction scarring in open quantum dots: A microwave-billiard analogy study. *Phys. Rev. B* **65**, 165317 (2002).
- [Kim03a] Y.-H. Kim, M. Barth, U. Kuhl, and H.-J. Stöckmann. Current and vorticity auto correlation functions in open microwave billiards. *Prog. Theor. Phys. Suppl.* **150**, 105 (2003).

- [Kim03b] Y.-H. Kim, M. Barth, U. Kuhl, H.-J. Stöckmann, and J. P. Bird. Scanning Fourier spectroscopy: A microwave analog study to image transmission paths in quantum dots. *Phys. Rev. B* **68**, 045315 (2003).
- [Kim05a] Y.-H. Kim, U. Kuhl, H.-J. Stöckmann, and J. P. Bird. Investigating dynamical tunnelling in open quantum dots by means of a soft-walled microwave-cavity analogue. *J. Phys.: Condens. Matter* **17**, L191 (2005).
- [Kim05b] Y.-H. Kim, U. Kuhl, H.-J. Stöckmann, and P. W. Brouwer. Measurement of long-range wave-function correlations in an open microwave billiard. *Phys. Rev. Lett.* **94**, 036804 (2005).
- [Kuh98] U. Kuhl. *Mikrowellenuntersuchungen an eindimensionalen Streusystemen und in zweidimensionalen Kavitäten*. Dissertation Philipps-Universität Marburg (1998).
- [Kuh00] U. Kuhl, E. Persson, M. Barth, and H.-J. Stöckmann. Mixing of wavefunctions in rectangular microwave billiards. *Eur. Phys. J. B* **17**, 253 (2000).
- [Kuh07] U. Kuhl. Wave functions, nodal domains, flow, and vortices in open microwave systems. *Eur. Phys. J. Special Topics* **145**, 103 (2007).
- [Lau94] H.-M. Lauber. *Experimenteller Nachweis geometrischer Phasen und Untersuchungen der Wellenmechanik nichtintegrabler Systeme mit Mikrowellenresonatoren*. Dissertation Ruprecht-Karls-Universität Heidelberg (1994).
- [Law01] G. Lawton. Monsters of the deep (the perfect wave). *New Scientist* **170**, 28 (2001).
- [Li94] B. Li and M. Robnik. Statistical properties of high-lying chaotic eigenstates. *J. Phys. A* **27**, 5509 (1994).
- [Lid00] A. R. Liddle and D. H. Lyth. *Cosmological inflation and large-scale structure*. Cambridge University Press Cambridge (2000).
- [Lon52] M. S. Longhuet-Higgins. On the statistical distribution of the heights of sea waves. *J. of Marine Research* **11**, 245 (1952).
- [Lon57a] M. S. Longhuet-Higgins. The statistical analysis of a random, moving surface. *Phil. Trans. R. Soc. Lond. A* **249**, 321 (1957).
- [Lon57b] M. S. Longhuet-Higgins. Statistical properties of an isotropic random surface. *Phil. Trans. R. Soc. Lond. A* **250**, 157 (1957).
- [Mad27] E. Madelung. Quantentheorie in hydrodynamischer form. *Z. Phys.* **40**, 322 (1927).
- [Mar92] C. M. Marcus, A. J. Rimberg, R. M. Westervelt, P. F. Hopkins, and A. C. Gossard. Conductance fluctuations and chaotic scattering in ballistic microstructures. *Phys. Rev. Lett.* **69**, 506 (1992).
- [Mar02] R. Maranganti, P. Sharma, and L. Wheeler. Quantum notion of stress. *J. Aerosp. Eng.* **20**, 22 (2002).

- [Mis73] C. W. Misner, K. S. Thorne, and J. A. Wheeler. *Gravitation*. W. H. Freeman New York (1973).
- [Nie85] O. H. Nielsen and R. M. Martin. Quantum-mechanical theory of stress and force. *Phys. Rev. B* **32**, 3780 (1985).
- [Ono01] M. Onorato, A. R. Osborne, M. Serio, and S. Bertone. Freak waves in random oceanic sea states. *Phys. Rev. Lett.* **86**, 5831 (2001).
- [Pau33] W. Pauli. *Quantentheorie, Handbuch der Physik XXIV*. Springer Berlin (1933).
- [Pau80] W. Pauli. *General Principles of wave mechanics, Handbuch der Physik XXIV*. Springer Berlin (1980).
- [Per84] A. Peres. Stability of quantum motion in chaotic and regular systems. *Phys. Rev. A* **30**, 1610 (1984).
- [Por65] C. E. Porter. *Statistical Theory of Spectra: Fluctuations*. Academic Press New York (1965).
- [Pre89] W. H. Press, B. P. Flannery, S. A. Teukolsky, and W. T. Vetterling. *Numerical recipes in PASCAL*. University Press Cambridge (1989).
- [Ric45] S. O. Rice. *Bell Sys. Tech. J.* **24**, 46 (1945).
- [Rog02] C. L. Rogers and A. M. Rappe. Geometric formulation of quantum stress fields. *Phys. Rev. B* **65**, 224117 (2002).
- [Sai01] A. I. Saichev, K.-F. Berggren, and A. F. Sadreev. Distribution of nearest distances between nodal points for the Berry function in two dimensions. *Phys. Rev. E* **64**, 036222 (2001).
- [Sai02] A. I. Saichev, H. Ishio, A. F. Sadreev, and K.-F. Berggren. Statistics of interior current distributions in two-dimensional open chaotic billiards. *J. Phys. A* **35**, L87 (2002).
- [Sch05] R. Schäfer, T. Gorin, T. H. Seligman, and H.-J. Stöckmann. Fidelity amplitude of the scattering matrix in microwave cavities. *New J. of Physics* **7**, 152 (2005).
- [Šeb99] P. Šeba, U. Kuhl, M. Barth, and H.-J. Stöckmann. Experimental verification of topologically induced vortices inside a billiard. *J. Phys. A* **32**, 8225 (1999).
- [She04] V. B. Shenoy. Chapter 7: Nanomechanics. In A. Lakhtakia, editor, *The Handbook of Nanotechnology: Nanometer Structures, Theory, Modeling and Simulations*. pp. 256–316. SPIE press (2004).
- [Sre96] M. Srednicki and F. Stiernelof. Gaussian fluctuations in chaotic eigenstates. *J. Phys. A* **29**, 5817 (1996).
- [Sri91] S. Sridhar. Experimental observation of scarred eigenfunctions of chaotic microwave cavities. *Phys. Rev. Lett.* **67**, 785 (1991).

- [Ste92] J. Stein and H.-J. Stöckmann. Experimental determination of billiard wave functions. *Phys. Rev. Lett.* **68**, 2867 (1992).
- [Ste93] J. Stein. *Eigenfunktionen von Hohlraumresonatoren*. Dissertation Philipps-Universität Marburg (1993).
- [Ste95] J. Stein, H.-J. Stöckmann, and U. Stoffregen. Microwave studies of billiard Green functions and propagators. *Phys. Rev. Lett.* **75**, 53 (1995).
- [Stöck90] H.-J. Stöckmann and J. Stein. “Quantum” chaos in billiards studied by microwave absorption. *Phys. Rev. Lett.* **64**, 2215 (1990).
- [Stöck99] H.-J. Stöckmann. *Quantum Chaos - An Introduction*. University Press Cambridge (1999).
- [Stöck04] H.-J. Stöckmann and R. Schäfer. Recovery of the fidelity amplitude for the Gaussian ensembles. *New J. of Physics* **6**, 199 (2004).
- [Tan07] G. Tanner and Søndergaard. Wave chaos in acoustics and elasticity. *J. Phys. A* **40**, R443 (2007).
- [Tao08] J. Tao, G. Vignale, and I. V. Tokatly. Quantum stress focusing in descriptive chemistry. Preprint (2008). arXiv:0801.2117v1.
- [Top00] M. A. Topinka, B. J. LeRoy, S. E. J. Shaw, E. J. Heller, R. M. Westervelt, K. D. Maranowski, and A. C. Gossard. Imaging coherent electron flow from a quantum point contact. *Science* **289**, 2323 (2000).
- [Top01] M. A. Topinka, B. J. LeRoy, R. M. Westervelt, S. E. J. Shaw, R. Fleischmann, E. J. Heller, K. D. Maranowski, and A. C. Gossard. Coherent branched flow in a two-dimensional electron gas. *Nature* **410**, 183 (2001).
- [Tru96] K. Trulsen and K. B. Dysthe. A modified nonlinear schrödinger equation for broader bandwidth gravity waves on deep water. *Wave Motion* **24**, 281 (1996).
- [Van03] J. Vaníček and E. J. Heller. Semiclassical evaluation of quantum fidelity. *Phys. Rev. E* **68**, 056208 (2003).
- [Wya05] R. E. Wyatt. *Quantum Dynamics with Trajectories, Introduction to Quantum Hydrodynamics* volume 28 of *Interdisciplinary Applied Mathematics*. Springer New York (2005).

# Acknowledgements

My thanks go to everybody who has contributed to this work or supported me during my time in Marburg.

- First of all, to Prof. Stöckmann for all his valuable help and guidance and for giving me the opportunity to do my PhD in his group. I have profited from his rich experience and many fruitful discussions with him.
- Prof. Eckhardt as the second referee for his kind interest in this work.
- A special thank goes to Ulrich Kuhl for reading the text critically, for many fruitful discussions and supporting me during my time in the quantum chaos group. He was always willing to listen to my questions and to answer my problems.
- Mark Dennis and Juan Diego Urbina for the discussion and the collaboration on the spatial correlation functions of open billiard systems.
- Karl-Fredrik Berggren for the collaboration on the quantum stress tensor and for the many discussions resulting in successful joint publication.
- Thomas Seligman for his hospitality at the CIC in Cuernavaca, Mexico and the fruitful discussions about our fidelity studies.
- Eric Heller and Lev Kaplan for the collaboration on the rogue wave study and the the discussions on this topic.
- Timur Tudorovskiy, Bernd Köber and Alexander Potzuweit of the quantum chaos group in Marburg for a very pleasant working atmosphere.
- The DFG for financial support.
- Last but not least I want to thank my dear wife Andrea for her support especially in the last few months during the time of writing this thesis.



# Wissenschaftlicher Werdegang

29.07.1977 Geboren in Kassel

1998 - 2005 Philipps-Universität Marburg: Studium Diplom-Physik mit Nebenfach Chemie (Vordiplom) und Informatik (Diplom)

09.10.2000 Vordiplom

23.02.2005 Diplom, Diplomarbeit in der Arbeitsgruppe Quantenchaos (Prof. Dr. H.-J. Stöckmann):

*“Untersuchung von Billiards mit symmetrischer Unordnung”*

2005 - 2008 Philipps-Universität Marburg: Promotion in der Arbeitsgruppe Quantenchaos (Prof. Dr. H.-J. Stöckmann):

*“Experimental tests of random wave models with chaotic microwave billiards”*